UNIVERSITY
OF TECHNOLOGY
SYDNEY

Laser Doppler Vibrometry Based Remote Sensing for Active Noise Control

by Tong Xiao

Thesis submitted in fulfilment of the requirements
for the degree of

Doctor of Philosophy

under the supervision of

Dr. Benjamin Halkon
A/Prof. Sebastian Oberst
Dr. Guoqiang Zhang

University of Technology Sydney
Faculty of Engineering and IT

November 2022

Author's declaration

I, *Tong Xiao* declare that this thesis, is submitted in fulfilment of the requirements for the award of Doctor of Philosophy, in the *Centre for Audio, Acoustics and Vibration* (*CAAV*), *School of Mechanical and Mechatronic Engineering*, *Faculty of Engineering and Information and Technology* at the University of Technology Sydney.

This thesis is wholly my own work unless otherwise referenced or acknowledged. In addition, I certify that all information sources and literature used are indicated in the thesis.

This document has not been submitted for qualifications at any other academic institution.

This research is supported by the Australian Government Research Training Program.

Production Note:
SIGNATURE: Signature removed prior to publication.

DATE: November 7, 2022

PLACE: Sydney, Australia

Abstract

Demands for active noise control/cancellation (ANC) to provide a quiet environment have grown significantly over the past few decades. Notably, many ANC headphones and earphones have emerged and gained much success in the market due to their excellent performance and robustness. There are also other ANC applications, such as ANC headrests and ANC windows. However, developments for such applications have been slow due to their relative complexity and cost of implementation. Particularly, the physical presence and the number of required sensors, typically condenser microphones, severely limit the performance of many ANC applications.

Laser Doppler vibrometry, which works on the principle of optical interferometry, has been widely used in to measure vibrations in many vibro-acoustic applications. Yet, the developed instrument, laser Doppler vibrometer (LDV), has little been studied in the published literature in the context of sound/noise measurement and control. The main advantage of such a technique is that it is often considered to be non-contact and non-invasive. For ANC headrests and windows, which prohibit the use of passive acoustic absorption materials and limit the installation of physical microphones for noise control, an LDV can be favourable by providing acoustic information remotely and inherently non-invasively.

This thesis, therefore, investigates and develops LDV-based remote acoustic sensing techniques for ANC applications, particularly ANC headrests and windows. The first part of the thesis studies how to use an LDV together with customised retro-reflective membranes to acquire acoustic information at discrete locations from a remotely positioned LDV. Then, such a configuration is used for remote error sensing in an ANC headrest scenario. The experimental results show significant improvements over the state-of-the-art systems. The reference signals are also investigated in ANC systems. Results show that a non-minimum-phase secondary path may require reference microphones to be installed at a considerable distance away from the secondary sources to have an adequate control performance, especially for the low frequencies. This is impractical in many applications. Remote acoustic sensing can also be applied for the reference signal. Results show that the proposed remote reference sensing can achieve a comparable result without the need for physical connections like those required for conventional microphones.

The second part of the thesis is concerned with measuring and controlling noise over a large area, e.g., at a window or a similar opening. Instead of measuring at a series of discrete points as with a microphone array, refracto-vibrometry can serve as an alternative method to measure the sound field, quasi-continuously, over an area and then utilise the measurements for control. The major advantage of this technique is that it enables sound pressure measurement at all points of interest without disturbing the sound field and with high spatial resolution. Such a technique is preferable for noise control at windows and openings where ventilation and access are prioritised over the introduction of physical sensors. The sound field at an enclosure opening is measured in the experiment and used for the error signals for ANC. Results show that using refracto-vibrometry to measure a sound field can give a much finer resolution than using a microphone array and an ANC system as a consequence can have the optimal performance for a given secondary source arrangement.

Acknowledgments

I would like to express my deepest gratitude to my supervisors, Dr. Ben Halkon, A/Prof. Sebastian Oberst and Dr. Guoqiang Zhang, for all the guidance and support during my research. Without them, this thesis would not be possible. I take this opportunity to sincerely acknowledge their guidance, help and encouragement.

Special thanks to my previous supervisor, Prof. Xiaojun Qiu, who gave me the chance and guided me throughout my candidature. The discussions with him have deepened my understanding of acoustics and provided insights into my research.

I would like to thank everyone at the Centre of Audio, Acoustics and Vibration. In particular, my colleagues and co-authors, Dr. Sipei Zhao, Dr. Shuping Wang and Mr. Jiaxin Zhong. Discussions with them have broadened my knowledge of acoustics. It is also my pleasure to acknowledge the help from Dr. Qiaoxi Zhu, who gave me technical support and encouraged me through my dark days. I am also grateful to Dr. Somanath Pradhan for going through many difficulties at the beginning of our candidatures.

I would like to thank Dr. Buye Xu and Dr. Chuming Zhao during my internship at Facebook (Meta). They have given me many insights and supports throughout the journey.

I would like to acknowledge the support by the Research Training Program scholarship from the Australian Government.

Finally, I would like to thank my parents and my families for their selfless support throughout many different stages of my life.

List of Publications

Much of this work has either been published or submitted for publications as journal articles and conference proceedings. The following is a list of the manuscripts that formed the basis for the thesis.

Peer-reviewed International Journals:

1. **Xiao, T.**, Zhao, S., Qiu, X. and Halkon, B.: 2021, Using a retro-reflective membrane and laser doppler vibrometer for real-time remote acoustic sensing and control, *Sensors* **21**(11).
2. **Xiao, T.**, Qiu, X. and Halkon, B.: 2020, Ultra-broadband local active noise control with remote acoustic sensing, *Scientific reports* **10**(1), 1-12.

Peer-reviewed Conference Proceedings:

3. **Xiao, T.**, Halkon, B., Oberst, S., Wang, S. and Qiu, X.: 2022, Sound field measurement at an enclosure opening using refracto-vibrometry, *Proceedings of the 28th International Congress on Sound and Vibration, ICSV*, 2022.
4. **Xiao, T.**, Qiu, X. and Halkon, B.: 2021, Using a laser doppler vibrometer to estimate sound pressure in air, *in* S. Oberst, B. Halkon, J. Ji and T. Brown (eds), *Vibration Engineering for a Sustainable Future*, Springer International Publishing, Cham, pp. 371-377.
5. Zhong, J., **Xiao, T.**, Halkon, B., Kirby, R. and Qiu, X.: 2020, An experimental study on the active noise control using a parametric array loudspeaker, *INTER-NOISE and NOISE-CON Congress and Conference Proceedings*, Vol. 261, Institute of Noise Control Engineering, pp. 662-668.

6. **Xiao, T.** and Qiu, X.: 2019, A comparison of using sound pressure and particle velocity as error signals for local active noise control, *Proceedings of the 26th International Congress on Sound and Vibration, ICSV* 2019.

Table of Contents

List of Figures

FIGURE **Page**

List of Tables

CHAPTER 1

Introduction

1.1 Mechanism and Early History of Active Noise Control (ANC)

An active sound/noise control system was created as an alternative to passive control for low frequency sound. As illustrated in Fig. 1.1, for passive noise control a part of the incoming noise is reflected back by the sound-absorbing material. The majority is dissipated in the material where the sound energy converts to heat. However, passive control is normally effective for high frequencies since the dimension of the material must be larger than the wavelength of the primary noise. To work in the low frequency range, the size of the material will be too considerable to be used in practice. Active noise control, on the other hand, uses one or multiple secondary control loudspeakers to produce the “anti-noise”, which has the opposite phase than the primary noise. It typically works best for low frequencies.

Many consumer products and some researchers label ANC as "Active Noise Cancellation", which may not be exactly accurate and can be misleading. Sound and noise cannot be magically “cancelled” and “disappeared”. Instead, ANC - Active Noise “Control” - works based on the principle of superposition, that is, the anti-noise from the secondary sources(s) is superposed to the primary noise. The acoustic energy may thus be attenuated significantly at one or multiple

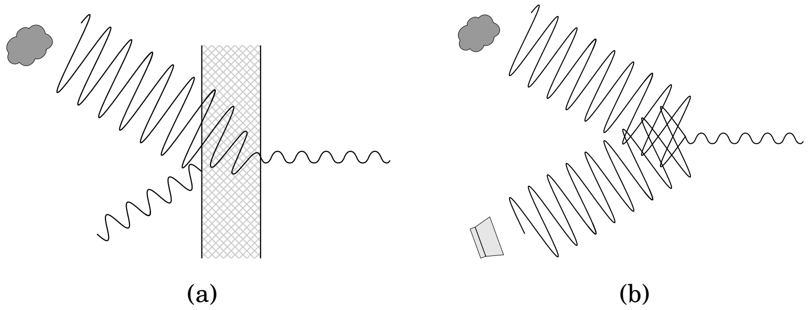

Figure 1.1: Illustration of (a) passive noise control and (b) active noise control

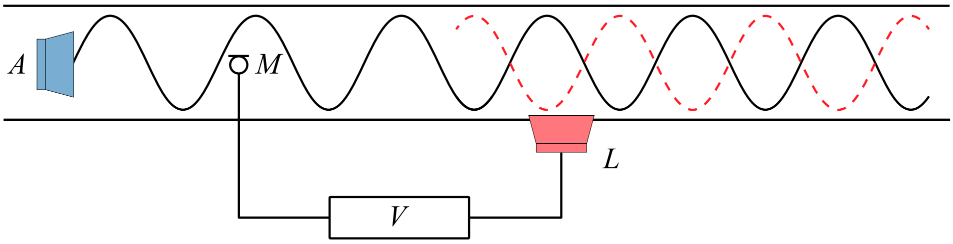

Figure 1.2: Figure redrawn from Lueg's patent (Lueg, 1936)

locations. However, the law of conservation of energy is still valid and the acoustic energy at other locations will be increased.

The very first ANC system is commonly credited to a German physicist, Paul Lueg, for his patent on “Process of Silencing Sound Oscillations”, which was filed in 1934 and granted in 1936 (Lueg, 1936). The one-dimensional principle illustration is shown in Fig. 1.2. The patent described the idea of using a microphone M to sense the existing undesired sound from A. An amplifier V, providing delays and amplification of the inverted detected sound, drove the control source L for cancellation. Although such a system, from the current view, is too simple to work in practice, it has laid the foundation for later emerging ANC systems.

Twenty years later, Olson and May (1953) and Olson (1956) studied such a system, named as “Electronic Sound Absorber” in ducts, for machines, rooms and passenger seats using feedback control as shown in Fig. 1.3. It is the earliest prototype in ANC headrests. However, due to the limitation of the technology at the time, the control performance was observable only at low frequencies, such as below 200 Hz.

The research went into hiatus again for the next few decades until the late

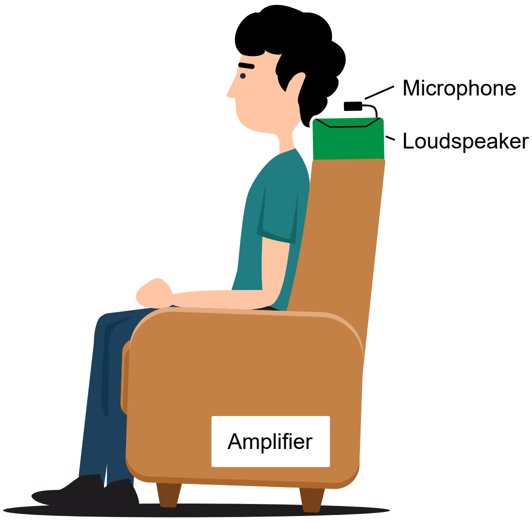

Figure 1.3: Figure redrawn from Olson (1953 and 1956)

1970s. Since the early 1980s, with the remarkable developments in digital signal processing and processors, ANC has seen interest and advances in many applications. Technological advances in other areas, such as mechanical and power electronic designs in large machines and vehicles, further urban development, manufacturing and so on, resulted in greater noise pollution and thus called for the use of ANC systems. Many researchers have studied both the theoretical (Piraux & Mazzanti, 1985; Piraux & Nayroles, 1980) and experimental behaviours of various systems, such as ducts (Berengier & Roure, 1980; Eghtesadi, 1983; Tichy & Warnaka, 1983), periodic noise (Chaplin, 1980, 1983), automotives (Oswald, 1984), enclosures (Curtis et al., 1985) and others (Guicking & Karcher, 1984; Swinbanks, 1984). In the late 1980s, more studies were conducted on the acoustics of ANC in free fields and enclosed sound fields (Bullmore et al., 1987; Elliott et al., 1988c; Nelson et al., 1987a,b; Snyder & Hansen, 1989). In the meanwhile, with the rise of the adaptive signal processing (Goodwin, 1984; Widrow & Stearns, 1985), more and more have made the ANC adaptive and real-time (Burgess, 1981; Carme, 1988; Elliott et al., 1988b; Eriksson et al., 1987; Roure, 1985; Warnaka et al., 1984, 1981).

In the 1990s and 2000s, the development of ANC systems has seen a great surge. Many applications (e.g., airplanes and open offices as illustrated in Fig. 1.4) required ANC functionality to regulate the noise. The details of the progress will be provided in the subsequent sections when reviewing the specific applications. A current modern ANC system, for example for a single-

(a)

(b)

Figure 1.4: Illustration of noise in (a) airplanes and (b) an open office.

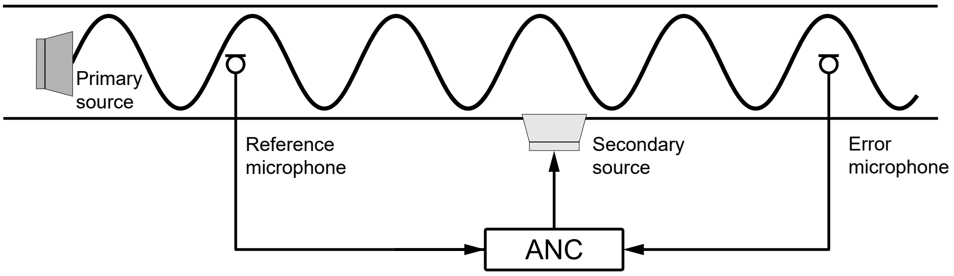

Figure 1.5: Configuration of single-channel ANC system in a duct.

channel system in a duct as shown in Fig. 1.5, contains the main components one reference microphone close to the primary source to sense the primary noise, an error microphone located at the point of interest to measure the residual noise after the control, and a secondary source to produce the anti-noise. In the feedback system, only the error signal is available for acoustic sensing. The hybrid structure combines both structures and uses both signals as input for better control performance.

1.2 Basic ANC Structures

Before finding the control filter, the secondary path, that is, the path from the secondary source to the error microphone should be determined. As shown in Fig. 1.6, the secondary path modelling, or system identification, is typically

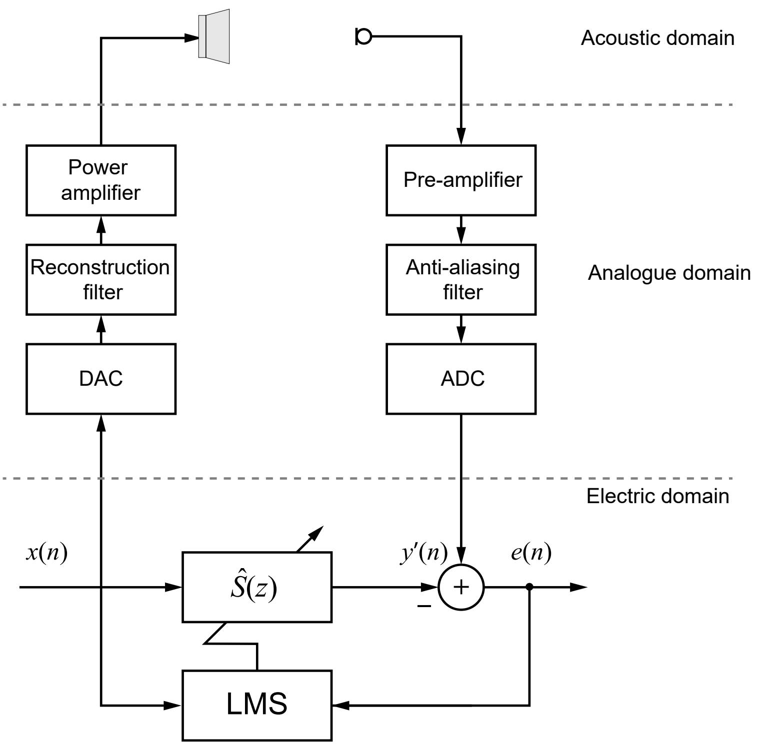

Figure 1.6: Offline secondary path modelling (system identification).

performed offline using the least-mean-square (LMS) algorithm. Once the secondary path is modelled, the estimated secondary path $\hat{S}(z)$ contains not only the transfer function of the acoustic domain but also the information of the electrical components in the analogue domain, such as power and pre-amplifiers, reconstruction and anti-aliasing filters, digital-to-analogue (DAC) and analogue-to-digital (ADC) converters.

Next, the control can be performed. The three main structures work as follows:

- **Feedforward** The feedforward control structure primarily uses the reference microphone to provide the time-advance signal of the primary noise. The secondary source signal is found by convolving the input reference signal with the control filter, which is determined by both the reference and the error signals as shown in Fig. 1.7a. The feedforward method can potentially reduce broadband noise at all frequencies, though the performance of which can depend on the relationship between the reference and the error microphones (e.g., coherence and causality).
- **Feedback** The feedback control structure should also be adaptive. As

demonstrated in Fig. 1.7c, there is only one error microphone providing the acoustic information. The feedback method does not require reference microphones. However, it can only control predictable noises, such as narrowband or low frequency noise (Elliott, 2000).

- **Hybrid** The hybrid ANC system has been proposed using both the feedforward and the feedback control methods (Akhtar & Mitsuhashi, 2011; Kuo & Morgan, 1996; Wu et al., 2015). The hybrid control structure, as shown in Figs. 1.7e and 1.7f, takes advantage of both methods to achieve a better control performance. The feedforward subsystem controls the coherent noise (w.r.t. the reference microphone) and the feedback subsystem controls the residual non-coherent predictable noise.

1.3 Development of ANC Applications

There are many types of ANC systems throughout history. They can be categorised into the following four groups by system complexity.

- **Duct noise** Early studies on ANC systems are based on duct noise (e.g., engine exhaust duct, air conditioner ducts). The environment is relatively simple (as in a tube) and the noise can be regarded as plane waves. ANC can be used in combination with reactive or dissipative mufflers to better control the duct noise.

- **Personal devices** Personal ANC devices include ANC headphones and earphones. Typically, the passive materials (e.g., perforated earpads or ear inserts) are used for attenuating the high frequency noise. ANC systems are used to control the low frequencies. Controlling noise in the ANC headphones is more complicated than controlling the duct noise. The environment in the earcup is more complex and the space constraint is more serious. Nonetheless, such systems have been well-developed and there have been many successful commercial products available in the market nowadays.

- **Interior noise** Controlling interior noise often means controlling the noise at local locations since controlling the noise in the whole enclosure can be extremely difficult. Typically, ANC headrest systems are used to

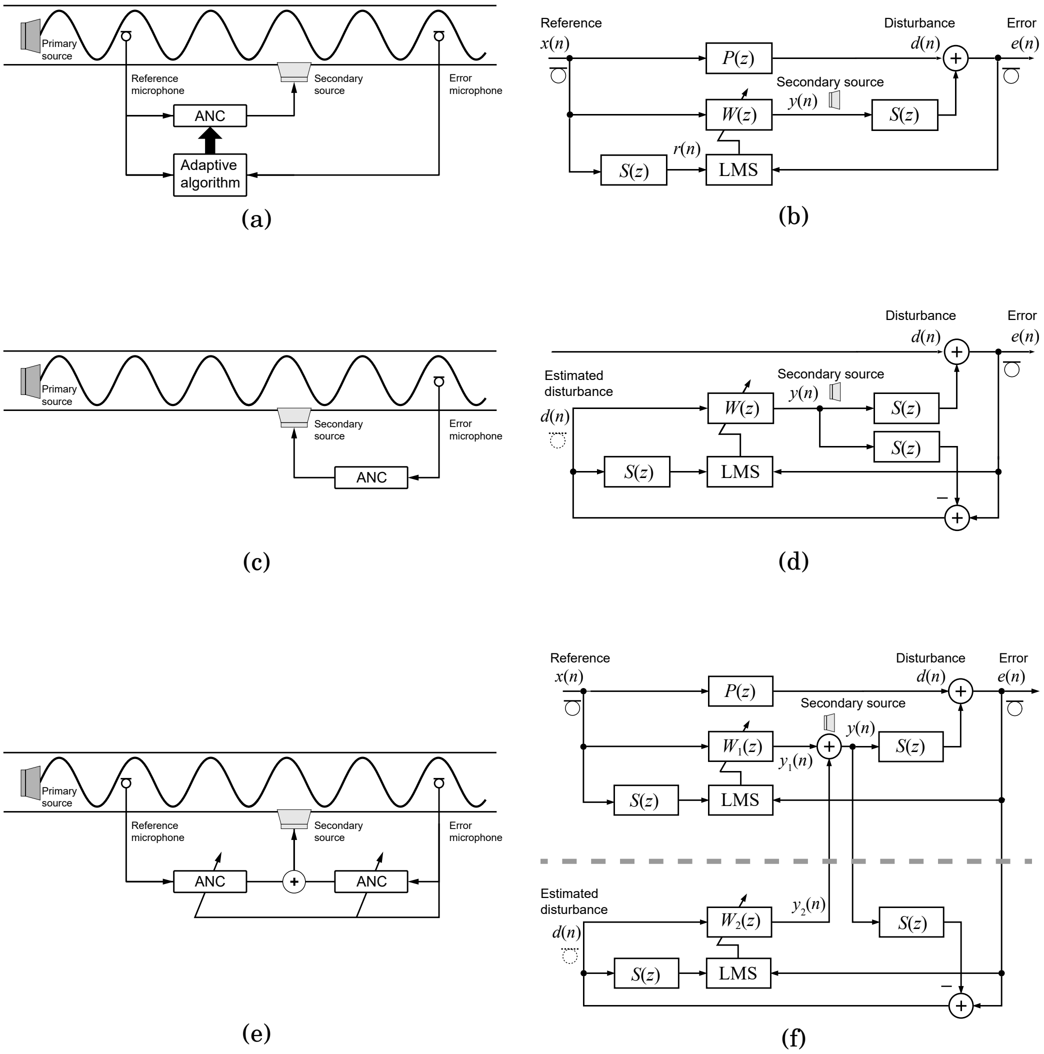

Figure 1.7: (Left column, from top to bottom) Configuration of single-channel feedforward, feedback and hybrid ANC systems, respectively. (Right column, from top to bottom) Block diagram of the FxLMS algorithm in the single-channel feedforward, feedback and hybrid ANC systems, respectively.

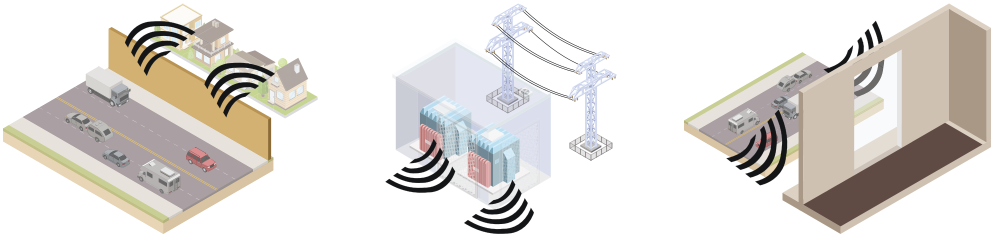

(a) (b) (c)

Figure 1.8: (a) Traffic noise near a residential area with noise barriers. (b) Transformer and other electrical plant noise through ventilation. (c) Traffic and urban noise through open windows.

provide users with zones of quiet. Similar to ANC headphones/earphones, such a system is also binaural. However, as further discussed below, ANC headrests can be more complicated due to many reasons (e.g., removal of passive material, long distances of secondary paths, transducer placements, etc.).

- **Free-space noise** Controlling free-space noise can be very challenging. Noise in a large area is expected to be controlled. Fig. 1.8 shows some applications, for example, traffic noise near a residential area with noise barriers, hum noise from transformers and other electrical plants through ventilation, traffic and urban noise through open windows. They typically require a large number of control channels.

The discussion on the development of ANC applications will be mainly focused on the following three systems - ANC headphones/earphones, ANC headrests and ANC windows.

1.3.1 ANC Headphones/Earphones

Although the basic principle of ANC was introduced by Lueg in the 1930s, it was not until the later 1950s (Hawley, 1956; Meeker, 1957; Simshauser & Hawley, 1955) and later in the late 1980s that detailed studies were carried out for headphones. The doctoral theses by Wheeler (1986) and Carme (1987) are commonly recognised as some of the first works. A reduction level of 10-15 dB up to about 500 Hz was achieved by Wheeler and more than 20 dB reduction for 50-400 Hz was achieved by Carme using the feedback control method.

Since then, there have been a substantial amount of studies on ANC headphones. Trinder & Jones (1987) showed more than 15 dB reduction for 60-600 Hz for an open-backed headphone. Veit (1988) described a slightly different system with microphones mounted externally. This system had a 10 dB reduction level from 250-1000 Hz. Twiney & Salloway (1990) patented a system that could reduce the low frequency pressure pulsations and thus make the system more stable. Later, Bai & Lee (1997) reported a feedback ANC system using the H_∞ robust control theory. A broadband noise of 200-800 Hz was attenuated by 15 dB. Gan et al. (2005) and later Kuo et al. (2006) used the adaptive feedback system in the headphone and evaluated the system against many factors. More than 30 dB reduction was achieved for narrowband harmonics from engine noise. Zhang et al. (2013) provided a simplified approach for easy implementation. A 15 dB reduction was achieved for the narrowband and about 14 dB reduction was achieved for 200-700Hz broadband noise.

Many systems also adopted the feedforward control architecture. Early work started from Jones & Smith (1983) and Chaplin et al. (1987) controlling periodic noise. Because of the feedforward configuration, broadband noise can be more easily controlled than that in feedback systems. Pan et al. (1997) and Brammer et al. (1997) showed an average of more than 10 dB noise reduction (maximum 26 dB) below 300 Hz for helicopter noise. Cartes et al. (2002) used the Lyapunov-tuned LMS algorithm to improve the system stability, particularly for time-varying noise. They demonstrated a noise reduction of 33 dB and 30 dB for pure tone and aircraft noise, respectively. Other issues, such as the causality of the feedforward configuration on the control performance (Cheer et al., 2019; Zhang & Qiu, 2014) and hardware-related implementations (Bai et al., 2018) were also explored extensively.

The direction of the incoming noise is important in the feedforward ANC systems. Studies (Cheer et al., 2019; Liebich et al., 2018; Rafaely & Jones, 2002; Zhang & Qiu, 2014) have demonstrated that the performance in ANC headphones and earphones was affected by the time advance between the reference and the error microphones in the feedforward configurations. The ANC performance was the best when the time advance was the most significant. There are a few solutions. The hybrid ANC algorithm (Liebich et al., 2018;

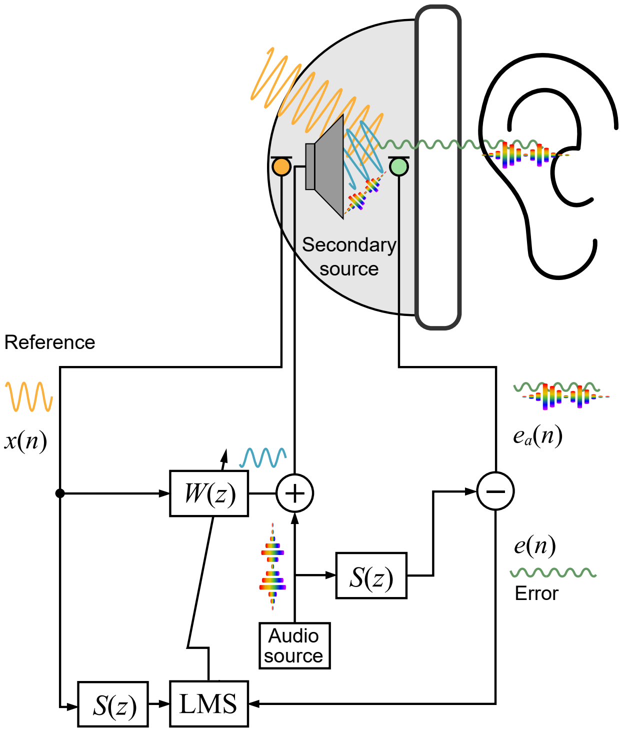

Figure 1.9: Diagram of the feedforward audio-integrated ANC system in headphones.

Rafaely & Jones, 2002) and the multi-reference ANC system (Cheer et al., 2019) were proposed to maintain the control performance when the causality of the system was compromised.

Another important functionality of ANC headphone and earphone systems is audio playback during noise control for communication or entertainment purposes. Such a system is often described as an "audio-integrated" ANC system (Chang et al., 2016; Gan & Kuo, 2002). Fig. 1.9 demonstrates the block diagram of an audio-integrated feedforward ANC system in headphones. The ANC components for controlling the noise are the same as the conventional ones. However, the desired audio is injected into the secondary source and replayed back to the user. This injected audio will also be detected by the error sensor and thus this injected signal passing through the secondary path should be subtracted by the error signal. Then the error signal will only contain the residual noise for the ANC algorithm.

1.3.2 ANC Headrests

An ANC headrest still typically uses two secondary sources (loudspeakers) to control noise at the user's ears. However, the main purpose of using such a system is to eliminate the discomfort from wearing headphones for a long period. In certain cases, the use of any headphones can be prohibited, for example, in moving vehicles. Therefore, as the name suggests, the secondary sources are installed in the headrest of a seat to control the noise for the user. Although the control algorithms used in ANC headrests do not differ significantly from the ones in headphones, due to the specific replacements of the components, ANC headrests have many hurdles. The major problems are listed as follows

- **Passive material removal** The main purpose of using an ANC headrest is to remove any devices and materials from the head and ears. For ANC headphones, the perforated earpads or ear inserts can provide effective passive noise reduction above 1 kHz in general (Bai et al., 2018; Liebich et al., 2018; Rudzyn & Fisher, 2012), whereas the ANC components are typically effective below 1 kHz. With the removal of the passive materials, the high frequency noise is left uncontrolled.

- **Long and dynamic secondary paths** The secondary sources in ANC headrests are significantly further away from the ears compared to being in the earcups on the head. Therefore, not only is the delay in the secondary path increased considerably, but the path can also be dynamic due to any movement of the user's head. In such cases, control can become extremely difficult.

- **Sensor placement** The placements of the reference and the error sensors are limited to certain locations. ANC algorithms minimise the sound pressure at the error sensors. However, the error sensors should not be installed close to the user's ears causing inconvenience. Similarly, the reference sensors should provide coherent reference signals with enough time advance. These signals may be compromised when the sensors can only be installed at certain locations.

Due to the problems above, ANC headrests are still undergoing early development. As mentioned previously, ANC headrests originate from the system proposed by Olson & May (1953). However, the development was on hiatus for four decades and it was not until the 1990s that ANC headrests regained the attention (Garcia-Bonito et al., 1997; Rafaely & Elliott, 1999; Rafaely et al., 1999; Sutton, 1994). Since then, many studies have been about the sensor placement issue, particularly the error sensors. The control performance at the user's ears can be severely degraded when the error sensors are installed remotely. The history and progress of optimising the ANC performance in headrests can be briefly described in the following methods.

- **Virtual microphone** (VM) This method essentially puts the two error microphones close to the user's ears (Garcia-Bonito et al., 1997). It was found that the presence of the user's head can enlarge the quiet zone (Garcia-Bonito & Elliott, 1995). When the error microphones are close, the quiet zone can be extended to the user's ears. However, since the quiet zone is about a tenth of the acoustical wavelength to be controlled (Elliott et al., 1988c), this method is only limited to low frequency noises.

- **Remote microphone** (RM) This method was proposed by Roure & Albarrazin (1999). The transfer function is pre-determined between physical microphones and temporarily placed virtual microphones. During control, the transfer function is applied to the signal from the physical error microphones such that the noise at the virtual locations is minimised. Recent studies have shown significant performance improvement using such a method (Elliott et al., 2018; Jung et al., 2017, 2018, 2019). However, one potential problem of such a method is that it is susceptible to any change in the primary path (i.e., the disturbance signal).

- **Virtual microphone control** (VMC) This method was proposed by Pawelczyk (2004). This method contains two stages - tuning and control. During the tuning stage, an adjustment filter is determined between the estimated disturbance signal and the error signal from the physical microphone when minimising the error signal at the virtual microphone. During the control stage, this adjustment filter is applied to the physical error signal (the associated estimated disturbance signal, to be exact) such that noise at the virtual location can be attenuated. Further use of such a method can be found in work (Pawelczyk, 2008; Shi et al., 2019). Comparisons were made from the above three method (Buck et al., 2018).

- **Auxiliary filter based virtual sensing** (AF-VS) This method is highly similar to the VMC method (Edamoto et al., 2016). The difference is that the adjustment (auxiliary) filter is directly applied to the reference signal instead of the estimated disturbance signal. Thus, this method can still be feasible when the estimated disturbance signal is not accurate (e.g., with a dynamic secondary path). This method can provide good performance even when the virtual error signal is non-causal (Kajikawa & Shi, 2019).

Some ANC headrests developed are illustrated in Figs. 1.10-1.13. There are also other virtual/remote sensing algorithms for solving the error sensor placement issue, which can be found in (Moreau et al., 2008). Other similar systems (e.g., ANC pillows, infant incubator ANC systems, etc.) that share similar problems as ANC headrests can be found in the overview paper by Chang et al. (2016) and Kajikawa & Shi (2019).

Problems regarding the reference sensors for ANC headrests have received very little attention so far. The reference signals were either taken from the accelerometers (Elliott et al., 1988b) or measured around the wheels (Jung et al., 2019) or on the floor of the vehicle (Cheer & Elliott, 2015). Similar systems were tested in aircraft and helicopters, where the reference signals were taken from the tachometers (Elliott, 2000). The reference sensors were far away from the main system and close to the noise sources, and multiple sensors were used to improve the coherence with error signals. So far, the main issues related to the reference sensors and signals in vehicles are about providing enough time advance and having good coherence with error signals. In practice, the implementation can be very difficult, such as choosing the best locations.

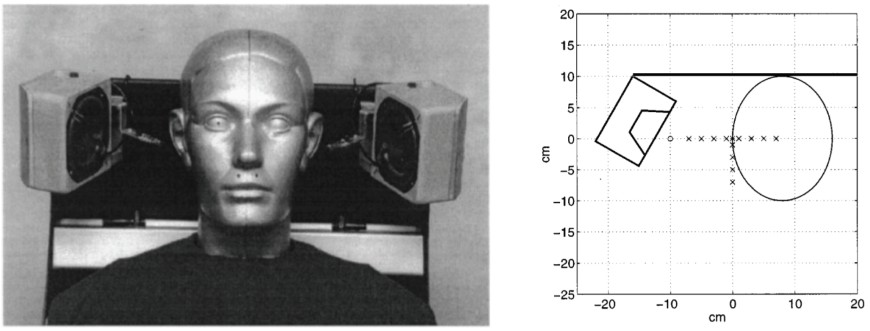

(a) (b)

Figure 1.10: (a) The experimental headrest system. (b) The geometric arrangement of the headrest, with the control loudspeaker, a physical control microphone marked by the circle located 2 cm away from the loudspeaker (Rafaely et al., 1999).

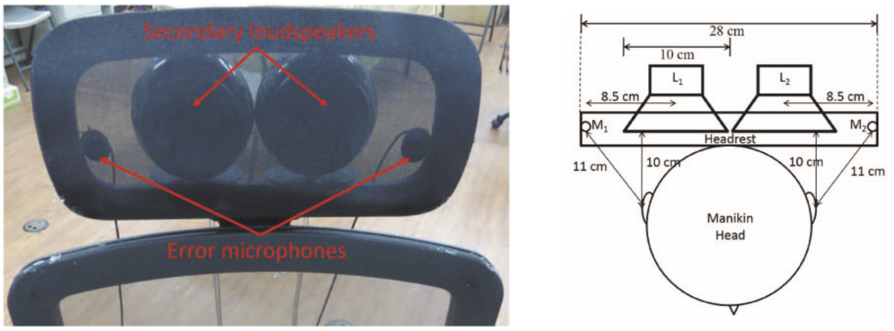

(a) (b)

Figure 1.11: (a) Proposed ANC headrest system. (b) Geometrical configuration of proposed systems (Siswanto et al., 2015).

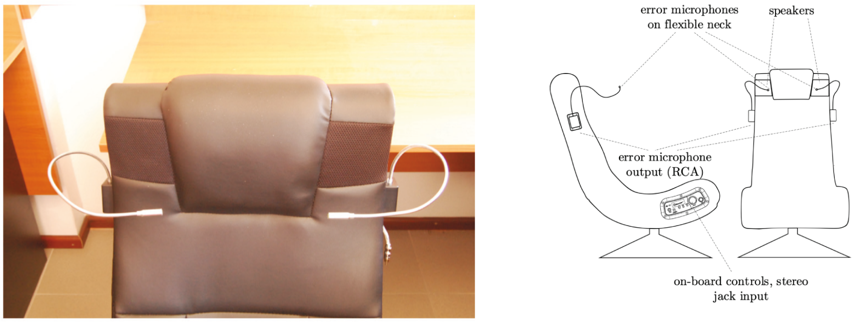

(a) (b)

Figure 1.12: (a) Photo of the headrest with the error microphones. (b) Sketch of the noise-canceling chair (Sujbert & Szarvas, 2018).

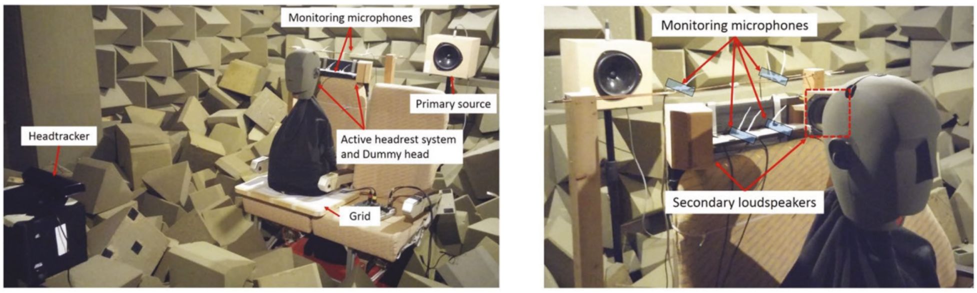

(a) (b)

Figure 1.13: (a) Physical arrangement used to demonstrate local active control at the ears of a listener while the head position is being tracked and (b) detail showing the position of the monitoring microphones and secondary loudspeakers (Elliott et al., 2018).

1.3.3 ANC Windows

It is easy to understand many apertures, such as windows and doors, require open access for various reasons, e.g., ventilation, daylighting and access (for doors). However, noise insulation is also a crucial aspect requiring consideration, particularly in urban areas with dense populations and urban noise pollution. Studies have shown that the sound attenuation through apertures (i.e., transmission loss) could be severely degraded as the covered area decreases. For example, the sound transmission loss can be 20 dB when fully shut. Even when it is 90% covered, there can only be about 10 dB transmission loss (Bies et al., 2017; Ford & Kerry, 1973). Therefore, similarly to ANC headrests, the removal of the passive material is detrimental and must be overcome. In addition, as discussed previously, passive materials are especially effective for high frequencies, whereas the performance is not as much for low frequencies. Active control can be very attractive when working in conjunction with passive control (Ohnishi et al., 2004), or in certain applications, works sorely to attenuate noise.

ANC for a large aperture/opening is normally very complicated. Unlike ANC headrests, which aim to attenuate noise at or around the user's ears, ANC windows (we use ANC windows mainly as the example application in discussion hereinafter) typically require a large number of channels ($\gg 4$ channels) for a large area. As the size of the opening increases, the required channels will also increase. Furthermore, the sound field at the opening can be complex. Not only the noise source can be non-stationary (e.g., traffic noise with moving vehicles or trains), but structures and the surroundings of the opening produce diffracted and reflected sound also makes the problem difficult in practice.

Some early work, particularly experimental work, can be traced to the 1970s controlling transformer noise (Hesselmann, 1978; Ross, 1978). Ford & Kerry (1973) found that a partially opened double glazing window can be 10 dBA better than a partially opened single glazing window. Jakob & Möser (2003a,b) investigated the use of ANC for double glazing windows, and they achieved about 7 dB with the feedforward controller and 3-6 dB with the feedback controller. Field & Fricke (1998) showed that quarter-wave resonators with different lengths could be used outside building ventilation openings to reduce noise with a reduction of 6-7 dB in certain 1/3 octave bands. Emms &

Fox (2001) compared three types of active absorbers to reduce sound transmission through a square aperture. They discovered that a maximally absorbing dipole and monopole combination could provide a more than 10 dB attenuation for wavelengths greater than three times the length of the aperture side. Since the 2000s, there have been many studies on controlling noise through an opening (either rectangular apertures or other irregular shapes). There has also been a study controlling very large scale outdoor sound fields (Heuchel et al., 2020). Some notable systems are listed in Table 1.1 with descriptions of the configurations.

These ANC window systems can be categorised into the following five types

- **Open apertures** This type consists of systems with an unobstructed opening with fixed dimension. Examples can be found in (Ise, 2005; Kwon & Park, 2013; Murao & Nishimura, 2012) as shown in Figs. 1.14, 1.15 and 1.16.

- **Sliding windows** This type is similar to open apertures, but with a sliding glass panel potentially changing the opening size. Examples can be found in (Carme et al., 2016; Lam et al., 2018b, 2020), as shown in Figs. 1.17 and 1.18.

- **Tilt windows** This kind of window is tilted only instead of fully opened. Examples can be found in (Brggemann et al., 2019; Eder et al., 2017; Hanselka & Sachau, 2016; Pàmies et al., 2014).

- **Plenum/staggered windows** Plenum windows have staggered air inlet and outlet. These systems can be found in (Huang et al., 2011; Tang et al., 2016; Tong et al., 2015).

- **Aperture of a baffled cavity** This kind of system is similar to open apertures and sliding windows, where noise propagates through an opening, though from a cavity in this case. This kind of system is illustrated in Fig. 1.19. It has been shown that both secondary sources and error microphones can be placed along the edges thus causing minimum obstruction (Wang et al., 2015, 2017a, 2019b, 2017b).

From the five types of systems, the configurations of the transducers, including the secondary sources and error microphones, are mainly divided into two groups - *distributed layout* and *boundary layout*. Hereinafter, the conventional rectangular openings (i.e., open apertures, sliding windows and aperture of a baffled cavity) are mainly investigated and discussed.

The distributed layout, as studied by Ise (2005), Murao & Nishimura (2012), Kwon & Park (2013) and Lam et al. (2020), installs the transducers even across the opening. The advantage of such a layout is the scalability of the system. The number of secondary sources is corresponding increased when the size of the opening is increased, though provided that the separation distance between the secondary sources remains to be less than half of the wavelength of interest. Although it can achieve a better ANC performance than the boundary layout, it is apparent that the distributed transducers lead to visual obstruction. More details can be found in (Lam et al., 2021).

The boundary layout, as studied by Tao et al. (2016); Wang et al. (2015, 2017a, 2019b, 2017b), promotes the transducers to be installed along the edges of the opening. The main advantage is that the opening is unobstructed. However, the boundary layout requires more secondary sources to achieve the same performance as the distributed layout. More layers of secondary sources can increase the frequency range, though the length of the short side of the opening ultimately decides the upper frequency limit to be controlled (Wang et al., 2019a). The error microphones can also be installed at the edges of the opening and a large amount is also needed. The length of the short side also decides the upper frequency limit, although it can be improved by adding more layers of microphones. More details can be found in (Qiu, 2019).

Table 1.1: Summary of prior work in the active control of sound through apertures (extended based on Lam et al. (2018b)).

Author	Type	Window Size (W × H [cm])	Opening Size	Ref Layout	No. of Ref (Distance* [cm])	Secondary Layout	No. of Secondary	Error Layout	No. of Error (Distance* [cm])	Type of Noise	Noise Reduction (Global/Local)
Window											
Ise (2005)	Open Aperture	N/A	N/A	N/A	N/A	Distributed	16	Distributed	16 (100)	BLWN (200 to 700 Hz)	10 dB (Local)
Murao & Nishimura (2012)	Open Aperture	25 × 25	25 × 25	Distributed	4 (5)	Distributed	4	Distributed	4 (10)	BLWN (500 Hz to 2kHz)	10-15 dB (Global)
Kwon & Park (2013)	Open Aperture	30 × 30	30 × 30	Boundary	4 (30)	Boundary	8	N/A	0	BLWN (400 Hz to 1 kHz)	Up to 10 dB (Global)
Pàmies et al. (2014)	Tilt Window	56 × 142	5cm Gap 2° Tilt	Single	1 (1500)	Boundary	1	Single	1 (42)	Real aircraft pass-by (20 to 160Hz)	3 dB (Global)
Carme et al. (2016)	Sliding Window	75 × 75	13 × 75	Single	1 (N/A)	Boundary	5	Distributed	5 (N/A)	Traffic Noise (<300 Hz)	15.5 dB (N/A)
Hanselka & Sachau (2016) Eder et al. (2017)	Tilt Window	91 × 91	N/A	Side	2 (35)	Boundary	8	Boundary	14 (N/A)	BLWN (100 Hz to 1 kHz)	13 dB (Local)
Brggemann et al. (2019)	Tilt Window	95 × 132.5	N/A	Side	2 (35)	Boundary	i. 14 ii. 20	Boundary	i. 14 (N/A) ii. 20 (N/A)	BLWN (0.1 to 1 kHz)	i. 5.5 dB (Local) ii. 10.0 dB (Local)
Lam et al. (2018b)	Sliding Window	100 × 100	18 × 93 30 × 93	Distributed	i. 8 (5) ii. 16 (5)	Distributed	i. 8 ii. 16	Distributed	i. 8 (50) ii. 16 (50)	Tonal (<2.1 kHz)	i. ~3 dB (Global) ii. ~4 dB (Global)
Lam et al. (2020)	Sliding Window	100 × 100	45 × 93	Single	1 (100)	Distributed	24	Distributed	24 (18)	i. BLWN (100 Hz to 1 kHz) ii. Traffic (100 Hz to 1 kHz) iii. Train (100 Hz to 1 kHz) iv. Aircraft (100 Hz to 1 kHz)	i. 8.8 dB (Global) ii. 8.67 dB (Global) iii. 10.14 dB (Global) iv. 7.51 dB (Global)
The opening of the baffled rectangular cavity											
Wang et al. (2015) Tao et al. (2016)	Open Aperture	–	43 x 67	Ideal	N/A	Distributed	6	Distributed	i. 12 (10) ii. 6 (10)	BLWN (<0.5 kHz)	~15 dB (Global)
Wang et al. (2017b)	Open Aperture	–	43 x 67	Ideal	N/A	Boundary	8	Boundary	8 (10)	BLWN (<1 kHz)	~10 dB (Local, 0.2 m around error)
Wang et al. (2017a)	Open Aperture	–	43 x 67	Ideal	N/A	Boundary	32	Distributed	32 (10)	Tonal (<1 kHz)	~20dB (Global)
Wang et al. (2017a)	Open Aperture	–	43 x 67	Ideal	N/A	Distributed	32	Distributed	32 (10)	Tonal (<1 kHz)	~20dB (Global)
Wang et al. (2019b)	Open Aperture	–	43 x 67	Ideal	N/A	Distributed	32	Boundary (Single Layer) Boundary (Double Layer)	32 (10) 32 (10)	Tonal (<1 kHz)	~10dB (Global) ~12dB (Global)

* The distance from the secondary sources.

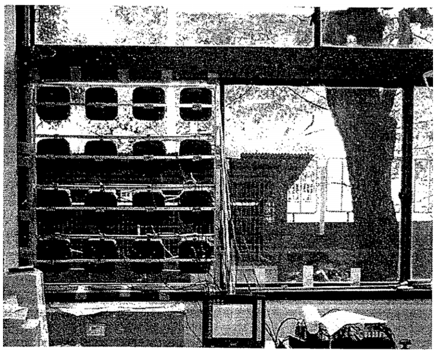

Figure 1.14: The ANC window with 16 loudspeakers and 16 error microphones evenly distributed across the entire window (Ise, 2005).

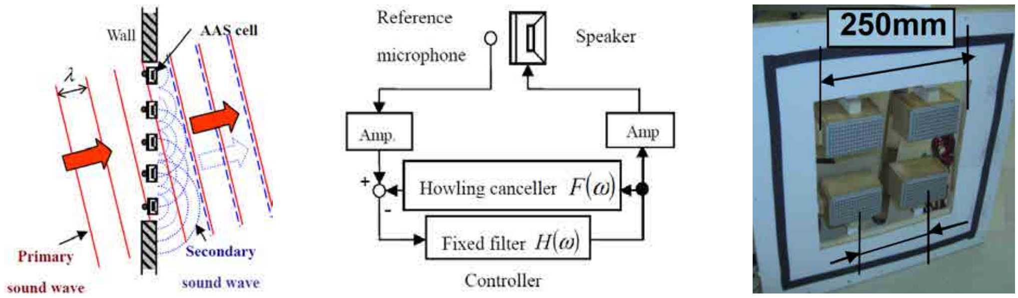

(a)

(b)

(c)

Figure 1.15: (a) Basic concept of the Active Acoustic Shielding (AAS), (b) diagram of an AAS cell and (c) photo of a 4-cell AAS window developed by Murao & Nishimura (2012).

(a)

(b)

Figure 1.16: (a) Experimental setup of the active window system. (b) Schematic of the ANC system (Kwon & Park, 2013).

(a)

(b)

Figure 1.17: (a) Photo of the active window system. (b) The active window with feedforward configuration (Carme et al., 2016).

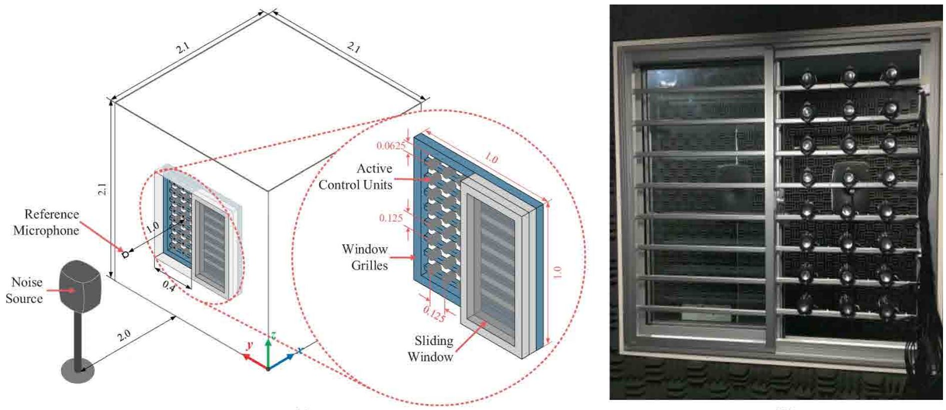

(a)

(b)

Figure 1.18: (a) Schematic of the mock-up room, and (b) view of the active control system from the inside of the mock-up chamber (Lam et al., 2020).

1.4 Instrument for Sound Measurement

1.4.1 Microphones

Microphones, being the primary tools for measuring sound information, have been extensively studied for many decades and their related theories are well-established. Nearly all common microphones acquire sound information using a lightweight, ultra-thin diaphragm under tension. The sound fluctuation cause displacement of the conducting diaphragm, which leads to a change in the electric change regarding the backplate. It is then amplified through a pre-amplifier for signal output. Depending on the working principle and construction, common measurement microphones have the following types. Fig. 1.20 shows the cutaway view of a typical condenser microphone.

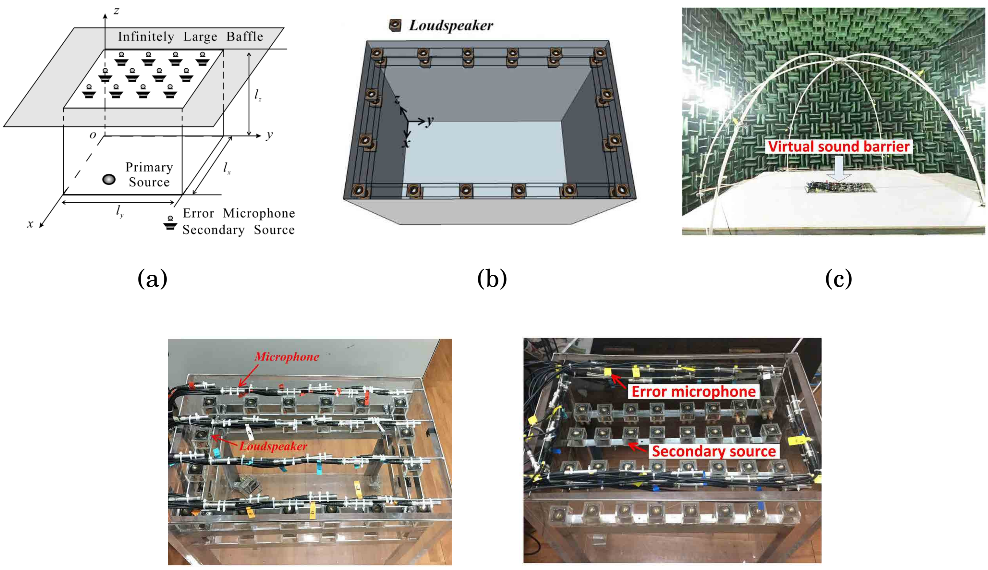

(a) (b) (c)

(d) (e)

Figure 1.19: (a) A schematic diagram of a planar Virtual Sound Barrier (VSB) system on the baffled opening of a rectangular cavity (Wang et al., 2015). (b) Schematic diagram of the double layered secondary loudspeaker system (Wang et al., 2017a). (c) The experimental setup. (d) A closer look at the VSB system at the opening (Wang et al., 2017a). (e) The experimental setup showing double-layer error microphones at the edge (Wang et al., 2019b).

- **Polarised condenser microphone** The electric change, i.e., the capacitance, is from the diaphragm and a polarised backplate, which needs an externally supplied bias voltage of the order of 200 V.
- **Prepolarised (electret) microphone** Similar to the condenser microphone, but the backplate is permanently polarised during manufacture. Thus, there is no need for high external voltage.
- **Piezoelectric microphone** The piezoelectric effect is used to convert the mechanical displacement of the piezoelectrical crystal to an electrical signal.
- **Dynamic microphone** A coil is attached to the diaphragm with a permanent magnet. The diaphragm displacement causes changes in the magnetic field.
- **MEMS (micro-electromechanical systems) microphone** It is similar to the condenser microphone and the electret microphone but can be fabricated with pre-amplifiers in a much smaller form factor.

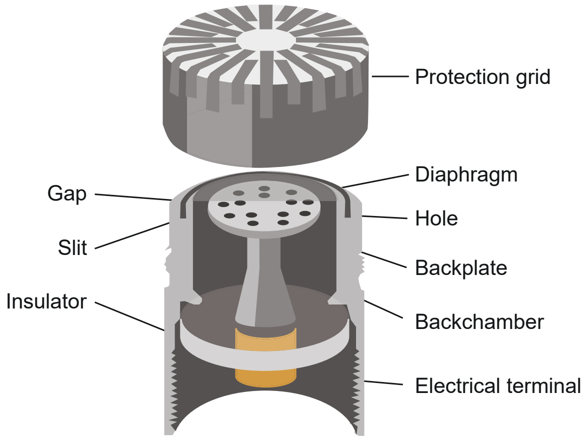

Figure 1.20: Cutaway view of a condenser microphone (Brüel & Kjær, 2019; Eargle, 2012).

- **Optical microphone** It also uses a moving diaphragm, but the displacement is detected by the modulated light through optical fibres. It is typically used in special cases, such as around a magnetic resonance imaging (MRI) scanner, which forbids metallic objects.

One can find thorough details about the designs and developments of microphones in (Brüel & Kjær, 2019; Crocker, 2007; Eargle, 2012).

Depending on the environment, microphones can be designed to be used in free fields, pressure fields or diffuse fields. Depending on the required directivity, microphones can be designed to be omni-directional or directional. Furthermore, typically microphones measure sound pressure directly, but some can also measure pressure gradient or sound intensity.

In terms of size, most microphones vary from 1/8 inch to 1 inch. The most common ones are the 1/2-inch and 1/4-inch microphones. The 1-inch microphones are typically used to measure low-level sound measurement, whereas 1/8-inch ones are typically used for high-level and high-frequency (i.e., ultrasound) measurement. Microphones should be as small as possible so as not to disturb the sound field. Diffraction effect, that is, the bending of sound waves as they encounter objects whose sizes are comparable to the sound wavelength can occur. Fig. 1.21 shows the diffraction effect of a circular cylinder with various angles of incidence. The limit of diameter/λ is commonly imposed and thus limits the size of the microphone.

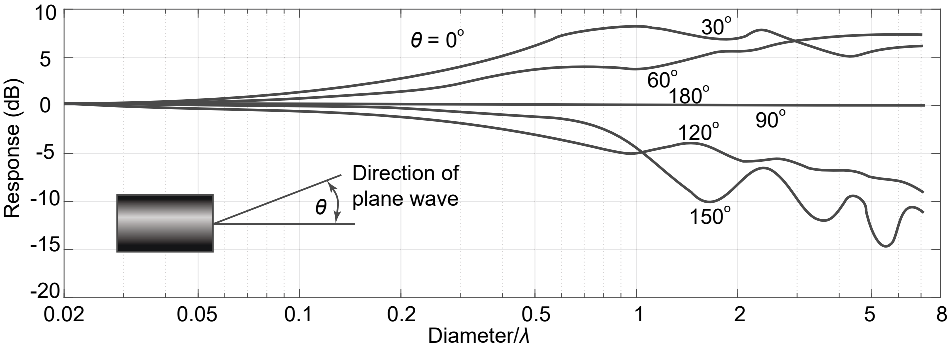

Figure 1.21: The diffraction effect with respect to the radius of the microphone (Muller et al., 1938).

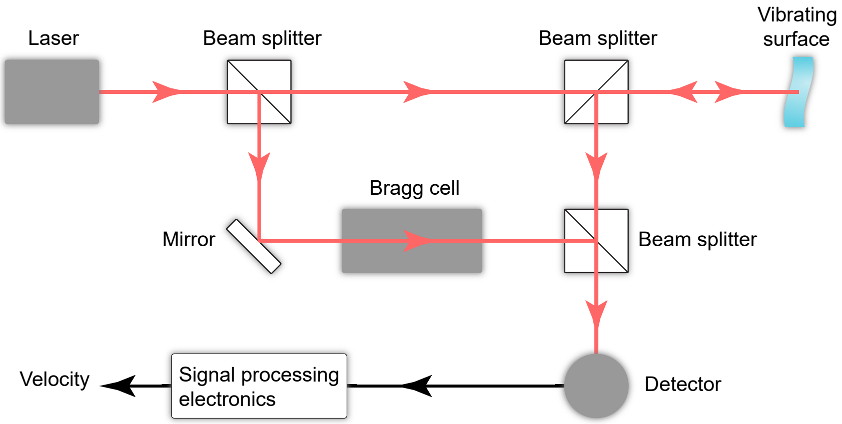

Figure 1.22: Schematic of an LDV.

1.4.2 Laser Doppler Vibrometers (LDVs)

Another instrument for acoustical and vibration measurement is the laser Doppler vibrometer (LDV). The schematic of an LDV is illustrated in Fig. 1.22. The laser beam is directed onto the surface of a vibrating object and is reflected back along the original path. The reflected laser beam is frequency modulated by a Doppler shift due to the vibration. There is another unshifted beam as a reference. After going through a photo-detector and some signal processing, the velocity of the vibrating object can be calculated. Compared to common accelerometers, which need to be installed on the object to measure the vibration and can potentially affect the behaviour of the object, LDVs offer non-contact and non-invasive measurements. Furthermore, LDVs typically have very high sensitivity with commercially available instruments able to resolve vibration displacements down to pm (picometre) and velocities down to nm/s resolution. These qualities make LDVs favourable in many applications.

Point-based Measurement

Using LDVs to measure discrete points on an object is evident, similarly to measuring with an accelerometer or a microphone. LDVs have been widely used in many vibro-acoustic and bio-acoustic applications (Ko et al., 2003; Suh et al., 2019; Tabatabai et al., 2013). In many vibro-acoustic applications, the objects under investigation are present. The vibration levels of these objects can be measured directly by the LDVs for modal analysis and other characterisations (Bissinger & Oliver, 2007; Suh et al., 2019; Zoran et al., 2012). In many acoustic sensing and control applications, on the other hand, the sound-originating sources can be inaccessible, or the particular point of interest for the pressure measurement is at a space in an air volume. The typical approach is to use one or multiple condenser microphones. However, as mentioned above, the physical presence of the traditional microphones and the cabling imposes various limitations.

Line-based Measurement

Another use of an LDV is the refracto-vibrometry, which is based on the acousto-optic effect - interaction between sound and light, can serve as an alternative to measure a sound field (Rothberg et al., 2017; Wissmeyer et al., 2018). Unlike taking vibration measurements of discrete locations, this technique provides projection/line-based measurements. Sound waves are compressional oscillatory disturbances that propagate in a fluid medium, such as air, as discussed in this thesis. The pressure and the density of the air are modulated with the resulting refractive index altering the light propagation, specifically regarding its amplitude and phase. These changes can be readily detected by the LDV, which is sensitive to path length fluctuations. Typically, these fluctuations are caused by surface vibrations at a point on a target of interest. However, when the reflecting surface is kept to be stationary, the highly sensitive measurement from the LDV only results from the variations in the optical path of the fluctuating sound field. Thus, any resulting velocity measurement is the integral of the sound information along its laser projection line. Since there is no physical sensor potentially disturbing the sound field, the refracto-vibrometry technique can be favourable to reconstructing a large sound field or a sound field that can be easily disturbed, e.g., ultrasonic waves.

Although one of the early works about the interaction between sound and light can be dated back to the early 1900s (Brillouin, 1922; Debye & Sears, 1932; Lucas & Biquard, 1932), it was not until the 1960s that the acousto-optic effect gained more attention (Gordon, 1966; Quate et al., 1965). However, at that time, sound was only used to characterise and manipulate light, rather than the opposite. For example, the acousto-optic effect was only researched to identify the diffraction of light. In addition, it was only for ultrasound from a few megahertz up to several hundreds of megahertz, and the media was mostly liquid or solid rather than air. In the 1990s and early 2000s, researchers began to study the effect in air and for audible frequency range sound (Lokberg et al., 1994; Oikawa et al., 2005; Zipser & Franke, 2008). Since then, there have been many studies devoted to using such an effect for sound field reconstruction. Note that the acousto-optic effect describes the general interaction between sound and light. The refracto-vibrometry technique refers to the use of LDVs to determine the phase shift of the laser due to sound. There are other optical arrangements, such as Schlieren (Chitanont et al., 2015, 2017), Moiré (Forno, 1988), TV holography (Lokberg et al., 1994), parallel phase-shifting interferometry (PPSI) (Ishikawa et al., 2016, 2017), that are not further discussed here.

Reconstructing a sound field in the audible frequency range in air using the refracto-vibrometry technique started by measuring an area close to a loudspeaker in a free field (Oikawa et al., 2005; Torras-Rosell et al., 2012). Later, more complicated sound fields with reflections and interference were investigated (Ikeda et al., 2016; Jackett et al., 2017; Malkin et al., 2014). Sound fields in rooms have also been evaluated (Fernandez-Grande et al., 2019; Verburg & Fernandez-Grande, 2019, 2021; Verburg et al., 2019). Meanwhile, there have also been studies incorporating acoustical model during the reconstruction to make the results more accurate. Yatabe et al. (2017); Yatabe & Oikawa (2014, 2015) added the Kirchhoff-Helmholtz integral equation and the Herglotz wave function for interpolation when the measurements were limited or noisy. Acoustic holography has also been explored. By including the plane wave physical model during the reconstruction, the reconstructed sound field can be extrapolated and thus only a partial area needed to be measured (Fernandez-Grande et al., 2013; Grande et al., 2019; Rosell et al., 2012; Verburg & Fernandez-Grande, 2019, 2021; Verburg et al., 2019).

1.5 Problem Description and Motivation

Based on the previous literature review of the development of ANC applications, particularly for headrests and windows, there are still many issues with these systems at the moment. The aforementioned ANC headrests, for example, require the passive material to be removed. The error sensors cannot be installed at the user's ears for reasons of convenience. The reference microphones should provide enough time advance for causality reasons and thus they need to be placed at a certain distance away from the secondary sources and error microphones. Yet, they cannot be too far away to maintain good signal coherence with the error signals. Using conventional microphones has presented many hurdles to be overcome, particularly their physical presence and accessories.

Similarly, a number of challenges remain for the application of ANC to windows and apertures. It has been found that the distributed layout of the secondary sources and error microphones can achieve the best performance when controlling noise propagating through an opening. However, undesirable visual obstructions are also made apparent. The secondary sources and error microphones can be installed on the boundary of the opening, but such a system requires a considerable number of additional transducers over and above those that would be required for an evenly distributed arrangement of equivalent performance.

Compared with conventional condenser microphones, LDVs can offer non-contact *and* non-invasive measurement, a characteristic that has been widely used in vibration and vibro-acoustic applications. It seems that LDVs can offer the remote sensing technique to potentially resolve the identified open challenges in both ANC headrests and in windows, which both suffer from the physical presence of conventional microphones. Little published work has been carried out on the use of LDVs for sound/noise measurement *and* control so far. Therefore, this thesis focuses on the investigation and development of laser Doppler vibrometry based remote sensing for ANC applications.

1.6 Thesis Contributions and Outline

This thesis describes in detail several significant and novel contributions towards understanding and developing ANC applications with remote sensing

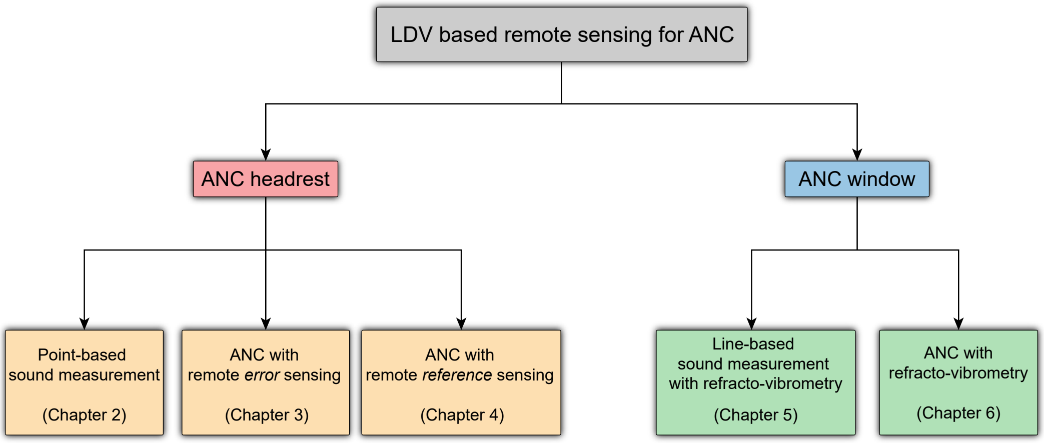

Figure 1.23: Major thesis contribution areas.

using an LDV (or multiple LDVs) due to its non-contact, remote functionality. The principle contribution areas and their relationships are shown in Fig. 1.23. Two main ANC applications, that are still undergoing development within the ANC community - headrests and windows, are investigated and extended using the remote sensing technique in place of conventional microphones.

The thesis outline is provided as follows with the corresponding contributions as described.

- **Chapter 2: Point-based sound measurement with LDVs**
  Similarly to measuring the sound pressure at one point as a conventional condenser microphone via a diaphragm, LDVs can also be used with an optical pick-up to acquire sound information, but remotely. The research and development of a remote acoustic sensing apparatus that consists of a retro-reflective membrane and an LDV at a remote location is reported. This system can measure acoustical pressure signals at remote locations with minimal instrumentation footprint. The small circular membrane pick-up without any cables can be placed at the location of interest, whereby the LDV can then measure the acoustically induced membrane surface vibration at that remote location. The membrane was purposefully chosen to be retro-reflective to allow a wide range of LDV laser beam incidence angles. A series of investigations are made to determine the optimal properties of such a configuration for effective sound pressure measurement.

- **Chapter 3: ANC with remote *error* sensing**
  The performance of an ANC headrest using a remote error sensing approach is investigated. The approach uses the aforementioned remote acoustic sensing configuration - an LDV and a small, lightweight and retro-reflective membrane pick-up placed in the cavum concha of a user's ear, thereby producing as little disturbance as possible. Such a system is illustrated in Fig. 1.24. The effects of its location on the system performance are explored with a head and torso simulator. Performance in the presence of different primary sound fields and diverse kinds of environmental noise are explored. A scanning LDV-based head tracking system is also developed to maintain the control performance during any possible head movements from the user. The results show that more than 10 dB of sound attenuation can be obtained for an ultra-broadband frequency range up to 6 kHz in the ears for multiple sound sources and various types of common environmental noise. The use of parametric array loudspeakers as the secondary sources makes it additionally possible not to increase the overall sound pressure levels at places other than at the error points while maintaining the same control performance.

- **Chapter 4: ANC with remote *reference* sensing**
  This chapter focuses on the reference sensors and signals in large ANC systems (that is, the secondary path is long compared to, for example, that in ANC headphones). It begins by examining some non-ideal reference signals affected by reflections and reverberation, which make it difficult to control the system. Long filters can be used and adaptive decorrelation filters can speed up the system convergence. Another solution is to use the hybrid ANC algorithm where the non-coherent signal component can be controlled in the feedback subsystem. Next, the locations of the reference sensors are studied. It is found that a typical non-minimum-phase secondary path requires a significant amount of time advance for the controller to have an adequate control performance, especially for low frequencies. The LDV-based remote acoustic sensing arrangement is also investigated for these reference signals. Results show that for a traditional reference microphone placed about 2.7 m

away from the error microphone and which must be physically connected to the ANC controller via cables, the remote reference sensing method can achieve a comparable performance outcome but without any physical connection.

- **Chapter 5: Line-based sound measurement with refracto-vibrometry**
  This chapter studies another LDV sound field measurement technique, which is line-based instead of discrete point-based. A sound field can be measured by an array of microphones distributed across the area of interest or by moving a smaller number of microphones sequentially. Such procedures can be time-consuming and expensive when high spatial resolution is required. Furthermore, the presence of physical microphones might disturb the sound field. Refracto-vibrometry is an LDV sound pressure measurement technique based on the acousto-optic effect. It can serve as an alternative method to measure sound pressure at all the points of interest without disturbing the sound field. In this chapter, three processing methods, the filtered back-projection, the truncated singular value decomposition and the Tikhonov regularisation methods, are used to evaluate the sound field at an enclosure opening. Quantitative comparisons with microphone array measurements show that the Tikhonov regularisation method yields the best result.

- **Chapter 6: ANC with refracto-vibrometry**
  This chapter investigates the use of refracto-vibrometry to measure the sound field as the error signals to control noise propagating through an opening, as illustrated in Fig. 1.25. Refracto-vibrometry can be preferable in opening applications since it does not impose any physical sensor challenges. Firstly, theoretical investigations are made to determine how many error signals are required for an effective control performance in a typical distributed layout regardless of which measurement technique. Both theoretical and experimental studies show that when the number of error signals is similar to that of the secondary sources, the high frequency noise can potentially increase. When using conventional microphones, since the number is limited, the ANC performance is com-

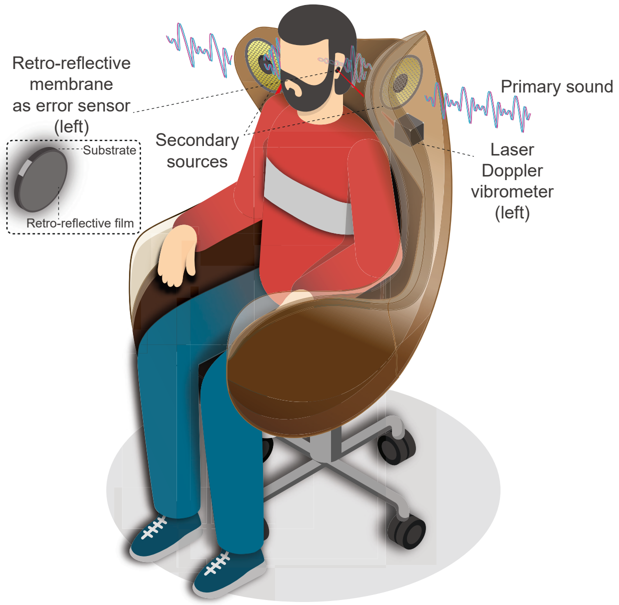

Figure 1.24: Demonstration of a "virtual ANC Headphone" - an ANC headrest with ultra-broadband control.

promised. The main advantage of using refracto-vibrometry lies in using a sufficiently large number of secondary sources controlling the high frequency noise. A large number of error signals are readily available from refracto-vibrometry while imposing no obstruction, which is favourable for opening applications. This technique can serve as a complementary error sensing method for controlling the high frequency noise, while low frequency noise can still be controlled using conventional microphones as error sensors.

- **Chapter 7: Conclusions and future works**
  The final chapter presents a summary of conclusions drawn from the work presented in the chapters and provides suggestions for future work.

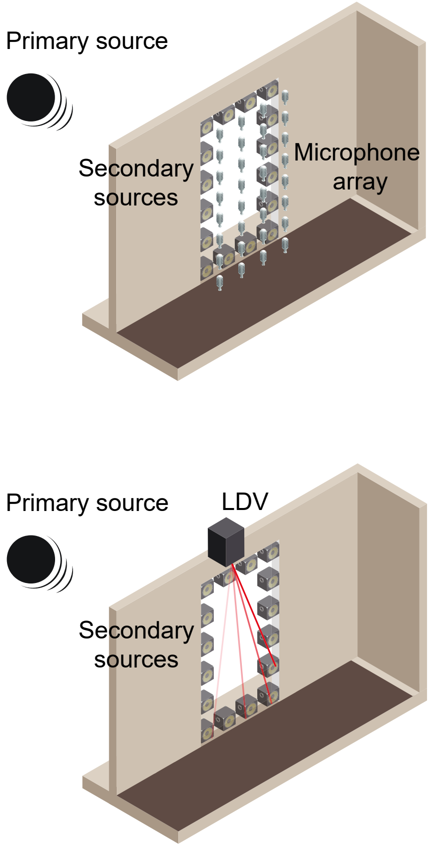

(b)

Figure 1.25: Demonstration of controlling noise through an opening by (a) a distributed microphone array. (b) refracto-vibrometry with an LDV.

CHAPTER 2

Point-based Sound Measurement with LDVs

2.1 Introduction

Condenser microphones, being the primary tools for measuring sound information, have been extensively studied and developed for many decades with their related theories well-established. It is the fundamental tool for sound pressure measurement at the points of interest. In recent years, micro-electro-mechanical-systems (MEMS) microphones have become more attractive due to their extremely small size. Certain special microphones, such as fibre-optic microphones (Bilaniuk, 1997; Garthe, 1991), also have special purposes for certain applications. However, while being sensitive and reliable, traditional microphones must be physically connected by cables for both power supply and for data transmission. In many sound field control applications in particular, for example, sound field reproduction and ANC, performance is limited by the physical presence and/or the wiring complication associated with traditional microphones (Eargle, 2012; Hansen et al., 2012).

In this chapter, an LDV is used as a part of the acoustic sensing element instead of an evaluation tool. The concept originates from the “optical microphone” or “laser microphone”, which can measure the vibration of objects at points projected from a laser beam when excited by the sound sources. A piece of retro-reflective tape is directly used as the diaphragm of the remote acoustic sensing arrangement instead of a piece of conventional ultrathin metallised polyester film or metal foil in conventional microphones (Eargle, 2012). One of the benefits is that the tape can be readily excited, which can lead to a wide dynamic range for the solution. Furthermore, the use of the retro-reflective material allows the laser beam to be at a wide range of angles with retained effective performance (Burgess et al., 2011a). More importantly, the medium between the LDV and the sensing retro-reflective membrane is simply air, requiring no physical connection between the physical quantity "pick-up" and the signal conditioning. Many applications can potentially benefit from this configuration. So far, there have been no comprehensive studies on the use of retro-reflective film as a direct acoustic pressure sensing component when combined with LDVs. Even though the dynamic behaviour of membranes has received significant attention, this has not yet included retro-reflective material membranes, and the related measured signal quality of LDVs when using them. These characteristics are crucial and must be determined before such pick-ups are used in acoustic sensing and control applications.

The remaining chapter is organised as follows: the design of the traditional condenser microphone and the response of the microphone diaphragm is examined by an LDV in Chapter 2.2. The theoretical analysis of the vibration of a circular membrane is presented in Chapter 2.3. An example of the membrane design is provided in Chapter 2.4, accompanied by some discussions of the design. The experimental performance validation in various aspects is reported in Chapter 2.5, followed by the practical application challenges presented in Chapter 2.6. Finally, the chapter is summarised in Chapter 2.7.

2.2 Traditional Microphone Diaphragm

2.2.1 Design and Theory

The governing equation for a circular membrane can be written as (Kinsler et al., 1999; Zuckerwar, 1978)

$$\nabla^2\eta(r,\theta)+K^2\eta(r,\theta)=\frac{p_{\mathrm{in}}}{T}-\frac{p(z,r,\theta)}{T}, \tag{2.1}$$

where $\eta(r,\theta)$ is the membrane displacement, r is the radial coordinate and θ is the azimuthal coordinate. p_{in} and p denote the incident sound pressure and the reaction pressure at the membrane surface, respectively. K is the

Table 2.1: Properties of the 1/2 in. microphone used for the analytical calculation.

Diaphragm parameter	**Symbol**	**Value**	**Unit**
Radius	a	4.445×10^{-3}	m
Thickness	h	5×10^{-6}	m
Density	ρ_{M}	8900	kg/m^3
Tension	T	3162.3	N/m

wavenumber of the membrane (Kang, 2017; Leissa, 1989) with

$$K = \sqrt{\lambda_{\mathrm{d}}^2 - \mathrm{i}\gamma_{\mathrm{d}}}, \quad \lambda_{\mathrm{d}} = \omega\sqrt{\frac{\sigma_{\mathrm{M}}}{T}}, \quad \gamma_{\mathrm{d}} = \beta\frac{\omega}{T}, \tag{2.2}$$

where i is the complex number, ω is the angular frequency, σ_{M} and T are the surface density and tension of the membrane, respectively. β is a damping factor.

By applying the Dirichlet boundary condition at the rim,

$$\eta(r,\theta)\big|_{r=a} = 0, \tag{2.3}$$

the zero-order solution for membrane displacement and velocity can be expressed as

$$\eta(r,\theta) = \frac{1}{K^2 T} p_{\mathrm{in}} \left[\frac{J_0(Kr)}{J_0(Ka)} - 1\right], \tag{2.4}$$

$$v(r,\theta) = \frac{\mathrm{i}\omega}{K^2 T} p_{\mathrm{in}} \left[\frac{J_0(Kr)}{J_0(Ka)} - 1\right], \tag{2.5}$$

where i is the complex number, a is the membrane radius. J_0 is the zero-th order Bessel function of the first kind. The membrane displacement is proportional to the incident sound pressure, whereas the velocity is scaled by the frequency ω.

The specifications of the Brüel & Kjær Type 4134 microphone shown in Table 2.1 are used to calculate the relationship between the sound pressure and the velocity of the microphone diaphragm. Assuming the incident sound is white noise with an ideally constant sound pressure of 1 Pa, the magnitude of the velocity of the microphone diaphragm is shown in Fig. 2.1.

The magnitude of the velocity is relatively low in the low frequency range. For example, the magnitude of the membrane velocity at 1 kHz is –87.8 dB.

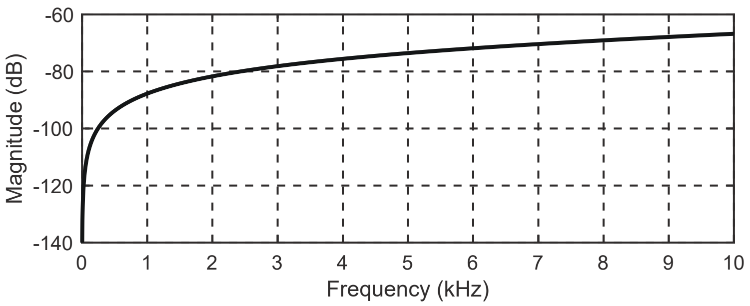

Figure 2.1: The analytical model of the membrane velocity using the specifications of the Brüel & Kjær Type 4134 (1/2 in.) microphone.

At 10 Hz and 100 Hz, the magnitude becomes –127.8 dB and –107.8 dB, respectively. It is clear that much greater energy is required to excite the membrane in the low frequency range below 1 kHz. The signal-to-noise ratio (SNR) in this frequency range can drop to a low value, making it difficult to obtain useful information.

2.2.2 Experimental Examinations

The microphone used in the testing is the Antysound Anty M1212 1/2 inch omni-directional free-field microphone. The protection grid was removed in the experiment to make its diaphragm exposed to the laser beam from the LDV. The LDV used in the experiments was the Polytec PDV-100 portable digital vibrometer with a frequency range of 0.5 Hz to 22 kHz. The velocity resolution is < 0.02 um $\mathrm{s}^{-1}/\sqrt{\mathrm{Hz}}$. A loudspeaker located approximately 0.5 m away from the microphone was driven by white noise. The diagram and the experimental setups are shown in Fig. 2.2.

The frequency response of the membrane velocity from the LDV corresponding to the white noise is shown in Fig. 2.3. It is apparent that the experimental result agrees well with the analytical model. The magnitude of the membrane velocity in the low frequency range (e.g. below 500 Hz) is considerably low and increases as the frequency increases.

The coherence between the loudspeaker signal and the sound pressure from the microphone and the membrane velocity from the LDV respectively is shown in Fig. 2.4. The coherence between the loudspeaker signal and the sound pressure is high (> 0.99) above 100 Hz. The coherence between the loudspeaker signal and the membrane velocity measured from the LDV is high

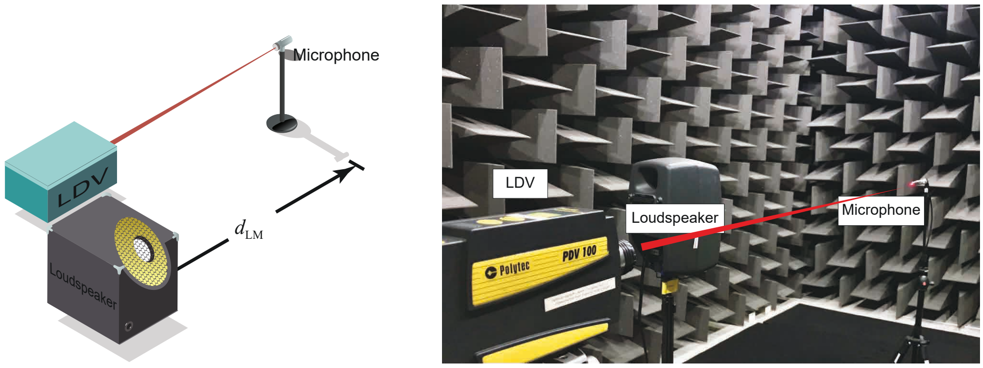

(a) (b)

Figure 2.2: (a) Diagram of the system setup. (b) The experimental setup in a hemi-anechoic chamber.

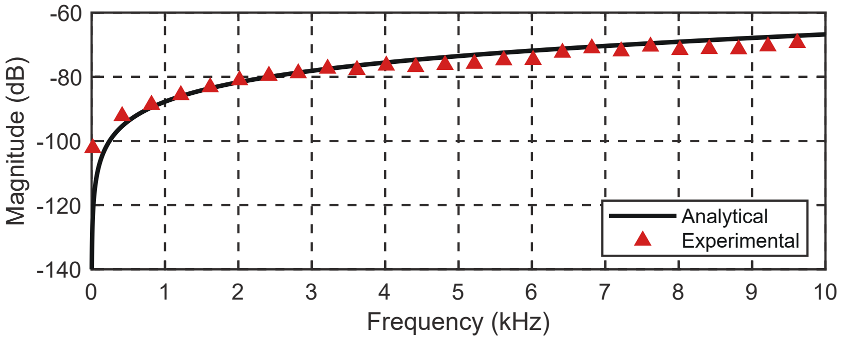

Figure 2.3: The magnitude of the membrane velocity measured from the LDV corresponding to the white noise from a loudspeaker, compared to the analytical model.

above approximately 300 Hz. The low coherence value below 300 Hz makes it difficult to convert the membrane velocity to the sound pressure.

The relatively low coherence value below 300 Hz is most likely due to the low magnitude of the membrane velocity measurement, which is demonstrated in Figs. 2.1 and 2.3. The low magnitude of the membrane velocity, accompanied by high background noise in this region, can easily result in low SNR, hence leading to a low coherence value.

2.3 Membrane Theoretical Development

The governing equation for a circular membrane shown in Fig. 2.5 should also satisfy Eqs. (2.1) and (2.2).

When satisfying the boundary condition in Eq. (2.3), the solution for

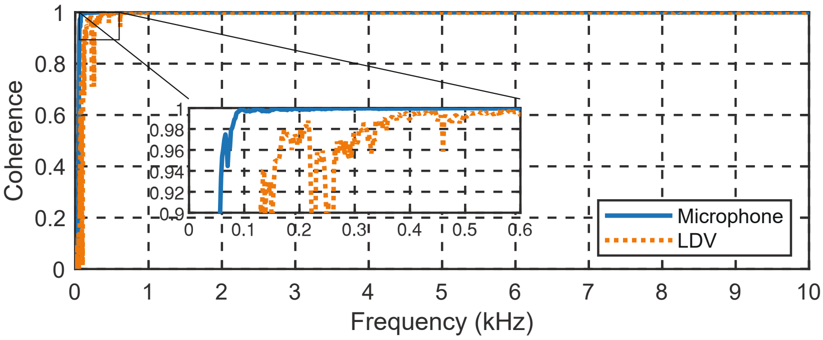

Figure 2.4: Coherence between the loudspeaker signal and the sound pressure from the microphone and the microphone diaphragm velocity measured from an LDV.

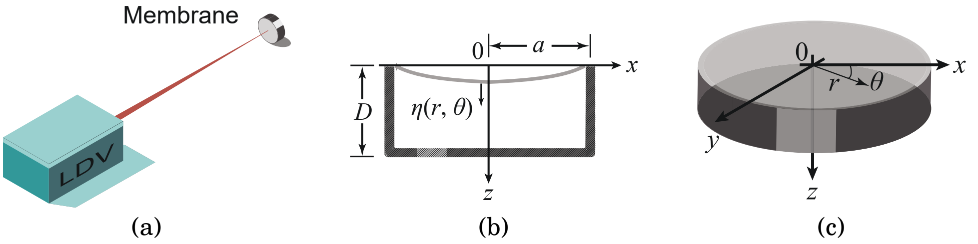

(a) (b) (c)

Figure 2.5: (a) Schematic diagram of the demonstrated remote acoustic sensing apparatus, where the LDV measures the acoustically induced vibration of the membrane at the point of testing. (b) Cross section of the membrane with a backing cavity. (c) Isometric view of the membrane.

Eq. (2.1) can also be written as

$$\eta(r,\theta)=\sum_{m=0}^{\infty}\sum_{n=1}^{\infty}A_{mn}\Psi_{mn}(r,\theta), \tag{2.6}$$

where $\Psi_{mn}(r,\theta)$ is the *in vacuo* modal shape of the membrane (Kinsler et al., 1999), i.e.,

$$\Psi_{mn}(r,\theta)=\mathrm{Re}\left[J_m\left(K_{mn}r\right)\cos(m\theta)\right], \tag{2.7}$$

where $J_m(x)$ is the m-th order Bessel function of the first kind. K_{mn} can be obtained with Eq. (2.2) by using the natural frequency ω_{mn} determined by the boundary condition $\mathrm{Re}\left[J_m\left(K_{mn}a\right)\right]=0$.

The modal coefficients A_{mn} in Eq. (2.6) can be obtained as (Lavergne et al., 2010)

$$A_{mn}=\frac{1}{T\left(K^2-K_{mn}^2\right)}\int_S\left[p_{\mathrm{in}}-p(z,r,\theta)\right]\Psi_{mn}(r,\theta)dS, \tag{2.8}$$

where S is the membrane area.

The reaction sound pressure inside the backing cavity is governed by the Helmholtz equation (Morse & Ingard, 1986),

$$\nabla^2 p(z,r,\theta) + k^2 p(z,r,\theta) = 0, \tag{2.9}$$

where $k = \omega/c_0$ is the acoustic wavenumber with c_0 being the speed of sound in air. the boundary conditions are

$$\left.\frac{\partial p(z,r,\theta)}{\partial r}\right|_{r=a} = 0, \tag{2.10a}$$

$$\left.\frac{\partial p(z,r,\theta)}{\partial z}\right|_{z=D} = 0, \tag{2.10b}$$

$$\left.\frac{\partial p(z,r,\theta)}{\partial z}\right|_{z=0} = -\rho_0\omega^2\eta, \tag{2.10c}$$

where ρ_0 is the air density, and D is the depth of the cavity.

The solution to Eq. (2.9) can be expressed with the modal expansion

$$p(z,r,\theta) = \sum_{s=0}^{\infty}\sum_{q=1}^{\infty}\left(B_{sq}\mathrm{e}^{\mathrm{i}k_z z} + C_{sq}\mathrm{e}^{-\mathrm{i}k_z z}\right)\Phi_{sq}(r,\theta), \tag{2.11}$$

where $k_z = \sqrt{k^2 - k_{sq}^2}$, and the modal shape $\Phi_{sq}(r,\theta)$ can be written as

$$\Phi_{sq}(r,\theta) = J_s(kr)\cos(q\theta). \tag{2.12}$$

By substituting Eq. (2.11) into Eq. (2.10a), one can obtain the eigenvalues k_{sq} from $J_s'(k_{sq}a) = 0$. In addition, substituting Eq. (2.11) into Eq. (2.10b) and (2.10c) yields, respectively,

$$B_{sq}\mathrm{e}^{\mathrm{i}k_z D} - C_{sq}\mathrm{e}^{-\mathrm{i}k_z D} = 0, \tag{2.13}$$

$$\mathrm{i}k_z\left(B_{sq} - C_{sq}\right)\Phi_{sq}(r,\theta) = -\rho_0\omega^2\eta. \tag{2.14}$$

Applying Eq. (2.11) into Eq. (2.8) with $z = 0$ and integrating over the membrane surface derives

$$T\left(K^2 - K_{mn}^2\right)A_{mn} + L_{mn,sq}\left(1 + \mathrm{e}^{2\mathrm{i}k_z D}\right)B_{sq} = P_{\mathrm{in},mn}\ , \tag{2.15}$$

where Eq. (2.13) is used to eliminate C_{sq}, $L_{sq,mn}$ denotes the coupling between the membrane vibration and the sound pressure inside the cavity (Morse & Ingard, 1986), which can be expressed as

$$\begin{aligned} &L_{mn,sq} \\ &= \int_S \Phi_{sq}(r,\theta)\Psi_{mn}(r,\theta)dS \\ &= \mathrm{Re}\left\{\frac{2\pi a\cdot\delta_{ms}\cdot\varepsilon_{ms}}{k_{sq} - K_{mn}}\left[K_{mn}J_s\left(k_{sq}a\right)J_{m-1}(K_{mn}a) - k_{sq}J_m\left(K_{mn}a\right)J_{s-1}\left(k_{sq}a\right)\right]\right\}, \end{aligned} \tag{2.16}$$

where δ_{ms} is 1 for $m = s$ and 0 for $m \neq s$, ε_{ms} is 1 for $m = n = 0$ and 0.5 for $m = s \neq 0$.

The (m,n)th mode modal coefficient of the incident sound pressure at the membrane surface in Eq. (2.15) can be written as

$$P_{\text{in},mn} = \int_S p_{\text{in}} \Psi_{mn}(r,\theta) dS = \begin{cases} \frac{2\pi a p_{\text{in}}}{K_{0n}} J_1(K_{0n}a), & m = 0 \\ 0, & m \neq 0 \end{cases}, \tag{2.17}$$

where the incident sound pressure p_{in} is assumed to be uniform over the membrane surface.

Similarly, substituting Eq. (2.6) into Eq. (2.14) yields

$$\rho_0 \omega^2 \sum_{m=0}^{\infty} \sum_{n=1}^{\infty} A_{mn} \Psi_{mn}(r,\theta) + \mathrm{i} k_z \left(1 - \mathrm{e}^{2\mathrm{i}k_z D}\right) \Phi_{sq}(r,\theta) B_{sq} = 0. \tag{2.18}$$

Multiplying $\Psi_{mn}(r,\theta)$ on both sides of Eq. (2.18) and integrating over the membrane surface generates

$$\pi a^2 \rho_0 \omega^2 \Lambda_{mn} A_{mn} + \mathrm{i} k_z \left(1 - \mathrm{e}^{2\mathrm{i}k_z D}\right) L_{mn,sq} B_{sq} = 0, \tag{2.19}$$

where $\Lambda_{0n} = [J_1(K_{0n}a)]^2$ and $\Lambda_{mn} = 1/2[J_{m-1}(K_{mn}a)]^2$ for $m > 0$.

By solving Eqs. (2.15) and (2.19) simultaneously, the modal coefficients A_{mn} and B_{sq} can be obtained, and C_{sq} can then be derived from B_{sq} in Eq. (2.13). After the modal coefficients are derived, both the membrane displacement and sound pressure inside the cavity can be calculated from Eqs. (2.6) and (2.11), respectively. As the wavelength for the sound pressure in the frequency range of interest (up to 4 kHz) is much larger than the size of the membrane and the cavity, both the membrane vibration and sound pressure inside the cavity are assumed to be axisymmetric, which means the subscript m should be 0 in all the above equations.

2.4 Retro-reflective Membrane Design and Modelling

Fig. 2.6 shows an example of the illustrated membrane specimen, where a piece of retro-reflective film (half shown for illustration purpose) had been applied upon a cylindrical enclosed tube (inner diameter = 5.6 mm, depth of the backing cavity = 3 mm) made of 3D printed acrylonitrile butadiene styrene. the

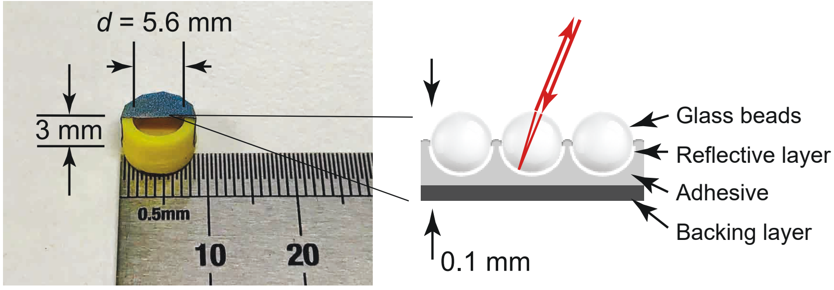

Figure 2.6: Membrane specimen (including the backing cavity) with a piece of retro-reflective film (half shown here for illustrating the backing cavity) and its composition; detailed specifications provided in Table 2.2.

commercial retro-reflective film (3M—Scotchlite Sheeting 7610) (Burgess et al., 2011a) was pre-coated with glass beads and a reflective layer to ensure that the reflected laser illumination could be directed in the same direction as in the inbound path back to the LDV optics. the thickness of the retro-reflective film was about 0.1 mm, with the size of the glass beads about 40 um. the material of the supporting base tube can be either polymeric or metallic, even though polymeric material is preferable in certain applications, such as near a magnetic resonance imaging machine, or applications requiring the membrane to be lightweight. When the membrane is stretched over the supporting base, it can be either clamped by an outer ring as in conventional condenser microphones (Hu et al., 1992), or adhered to the side of the supporting base tube. the latter design was chosen here for simplified construction as shown in Fig. 2.6. Table 2.2 provides the parameters of the membrane specimen with its backing cavity.

Using the parameters in Table 2.2, the displacement of the membrane specimen excited by a broadband white noise can be calculated using the analytical solution provided above. Three values of the membrane tension T at 20 N/m, 34 N/m and 90 N/m were investigated with a corresponding damping factor β of 100, 180 and 300, retrospectively, selected. the diameter of the membrane was 5.6 mm in this case. the resulting displacements are compared in Fig. 2.7a. For T = 20 N/m, the vibration resonance occurred at about 4.2 kHz. Although the overall level was the highest among the three examples when subject to the same SPL, i.e., 1 Pa, the working frequency range was only below 2 kHz, which cannot meet requirements in many applications. When T = 90 N/m; however, the resonant frequency occurred at approximately 9 kHz. Although

Table 2.2: Parameters of the designed membrane specimen with the backing cavity.

Quantity		**Symbol**	**Unit**	**Value**
Membrane Specimen (including the backing cavity)	Diameter	d	mm	4.0, 5.6, 7.0
	Thickness	h	mm	0.1
	Density	ρ_M	kg/m^3	204
	Tension*	T	N/m	20, 34, 90
	Damping factor	β	–	100, 180, 300
	Cavity depth	D	mm	3
Air	Sound speed	c_0	m/s	340
	Density	ρ_0	kg/m^3	1.205

* Tension of a membrane is determined by the measured resonance (Zuckerwar, 1978).

the working frequency range was wider (up to 6 kHz), the overall level was low, indicating a low sensitivity that is not desirable in some situations. When T = 34 N/m, the resonance occurred at 5.5 kHz, allowing the working frequency range of the demonstrated apparatus to be up to approximately 4 kHz. Meanwhile, the overall level (i.e., the sensitivity) was not significantly reduced. Therefore, it was reasonable to choose the design when the tension of the membrane is 34 N/m with a damping factor of 180.

In addition, the diameter of the membrane d was considered. Fig. 2.7b shows three examples when the diameter is 4.0 mm, 5.6 mm and 7.0 mm. the tension and the damping factor remained the same at 34 N/m and 180, respectively. Similar to the case of the membrane tension, when d = 4.0 mm, the vibration resonance was at 7.8 kHz, but the sensitivity was significantly low. On the other hand, when d = 7.0 mm, the sensitivity was increased; however, the resonance decreased to 4.3 kHz, leaving a working frequency range below 3 kHz only. When d = 5.6 mm, the working frequency range was up to 4 kHz with a satisfactory sensitivity compared to other scenarios.

In summary, the membrane tension is an important design factor. Increasing the membrane tension, decreasing the diameter or decreasing the surface density can increase the resonance frequency, thus extending the working frequency range. However, the sensitivity and the dynamic range are reduced

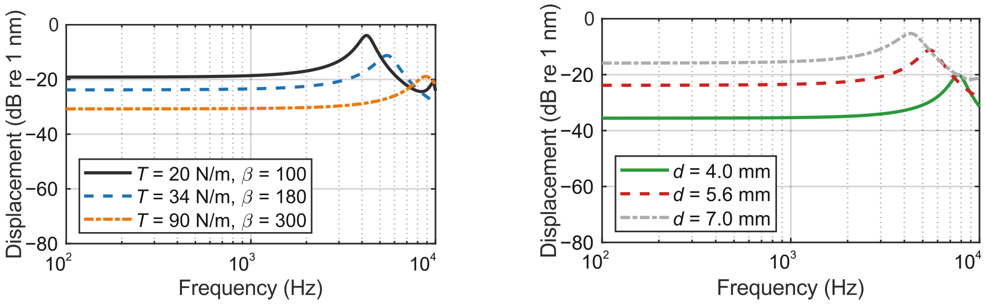

(a) (b)

Figure 2.7: The analytical displacements of the membrane (a) with three tension values and the adjusted damping factors, and (b) with three diameter values.

correspondingly (Kinsler et al., 1999). Therefore, for a given microphone design and material, i.e., a fixed diameter and surface density, this retro-reflective membrane should be properly stretched to have a balance between a sufficient sensitivity and a high natural frequency for specified applications.

With the frequency range of the membrane demonstrated hereinafter, the parameters of the retro-reflective membrane were chosen as d = 5.6 mm, T = 34 N/m and β = 180 such that the presented remote sensing system can measure various types of sound and noise, including human speech, which is generally below 4 kHz.

2.5 Experimental Validation

As shown in the previous sections, the displacement of the membrane is proportional to the incident sound pressure, and the output signal from the LDV can be multiplied by the sensitivity, converting the electrical signal from the LDV to the corresponding sound pressure. This is a similar approach to that used for condenser microphones, which use a sensitivity to convert the measured capacitance (converted to voltage) into sound pressure. As the sound pressure at the exact point of the membrane is unknown, a reference microphone (or multiple microphones) can be placed extremely close to the membrane specimen to monitor the sound pressure for calibration. Fig. 2.8a shows the system configuration for calibration and evaluation. the experimental setup, shown in Fig. 2.8b, was carried out in a hemi-anechoic chamber. the membrane under test was placed on a metal rod with an adjacent reference microphone (Brüel

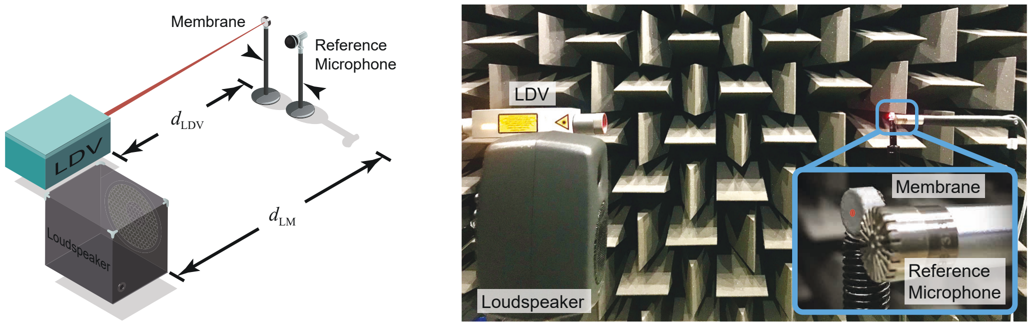

(a) (b)

Figure 2.8: (a) System configuration. (b) Experimental setup.

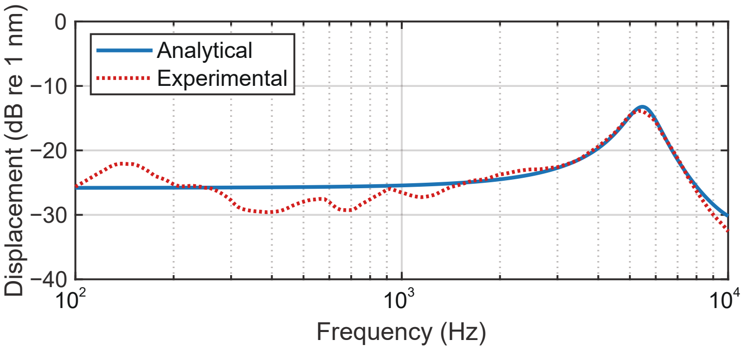

Figure 2.9: Analytical and experimental spectrum of the displacement of a membrane specimen obtained with white noise excitation, where resonance occurs at about 5.5 kHz.

& Kjær Type 4191) placed a distance of 0.01 m (d_{MM}) away. the LDV (Polytec NLV-2500-5) was located approximately 1.3 m (d_{LDV}) away with a displacement sensitivity setting of 50 nm/V. the laser beam was maintained at the centre of the membrane throughout the experiments. A loudspeaker (Genelec 8010A) was placed approximately 1.0 m (d_{LM}) from the microphone. the SPL measured by the reference microphone was 90 dB.

The spectrum of the membrane displacement was obtained initially and compared with the analytical solution in Fig. 2.9. It can be seen that the trend of the experimental results generally agrees with the analytical equivalent. There is a little discrepancy in the low frequency range, which might be caused by some minor distortion in the membrane and some minor reflections from the hemi-anechoic chamber. Nonetheless, the analytical model is valid for predicting the behaviour of the membrane.

2.5.1 Sensitivity

Conventional microphones use capacitance to represent the displacement of the microphone diaphragm, whereas the remote acoustic sensing apparatus uses the LDV to measure the membrane vibration displacement directly. the unit of sensitivity becomes nm/Pa instead of mV/Pa as for conventional microphones. However, the sensitivity of the proposed sensor cannot be made exactly like that of a condenser microphone. the sensitivity can be calculated by comparing the membrane displacement from the LDV to the SPL from the adjacent reference microphone. Fig. 2.10 shows the both the displacement measurement from the LDV and the SPL measured by the reference microphone and the signals were recorded using the “Steady-State Response (SSR) Analyzer” in the Brüel & Kjær Pulse LabShop software. the sensitivity of the membrane was calculated from the difference between the two as about 6.7 nm/Pa (or 16.6 dB re. 1 nm/Pa) for the range of 200 Hz to 4 kHz.

Notice that the previous fluctuations in the displacement measurement are also present in the reference microphone, which can confirm some minor reflections in the testing environment. When the sensitivity was calculated, the fluctuation was reduced to about ±2 dB from 200 Hz to about 4 kHz. However, the magnitude of the sensitivity is still high below 200 Hz, e.g., about 7 dB difference at 100 Hz, even though the displacement measurement from Fig. 2.9 was in agreement with the analytical result. This may be caused by the sensor head vibration from the LDV, which is more likely excited by low frequency sound. This issue has been extensively studied and solutions can be found in (Halkon & Rothberg, 2021).

Also notice the unit of the sensitivity of the membrane is nano-metre per Pascal (nm/Pa), whereas the one of the conventional condenser microphone is typically milli-volt per Pascal (mV/Pa). As reviewed in Chapter 1.4.1, the acoustically induced microphone diaphragm displacement is represented by the capacitance, *ergo* the unit is in (milli-)volt. The LDV directly measures the displacement, hence, the unit is expressed in (nano-)metre. Thus, direct comparison with the conventional microphones is not straightforward. However, as analysed in the next section, the noise floor and the dynamic range of the membrane will show the sound measurement capability.

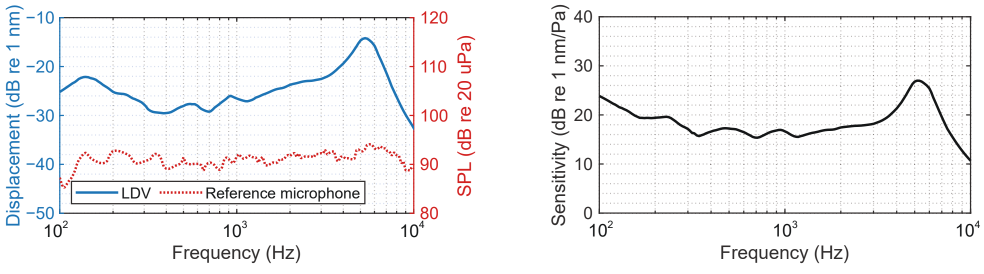

(a) (b)

Figure 2.10: (a) Spectrum of the membrane displacement from the LDV and the SPL by the reference microphone and (b) the corresponding sensitivity of the membrane as in displacement with respect to SPL monitored by the reference microphone.

2.5.2 Noise Floor and Limits

The overall background sound pressure level in the hemi-anechoic chamber measured by the reference microphone was approximately 23 dBA to 20 uPa. Meanwhile, the total background noise of the LDV was measured to be about −51 dBA re 1 nm, which was determined by pointing the LDV to the floor of the hemi-anechoic chamber. the background noise of the LDV cannot be simply translated to a sound pressure level using the sensitivity because the membrane displacement may not be proportional at a very low sound pressure level. To investigate this, the sound source with white noise was decreased from a total value of 90 dB to 50 dB with a step of 10 dB. As shown in Fig. 2.11a, the decrements were mostly consistent across the spectrum. In addition, three tonal signals at 500 Hz, 1 kHz and 4 kHz were set to various levels from 90 dB to 10 dB to observe the corresponding membrane displacement, which is shown in Fig. 2.11b. Overall, the membrane displacement is valid only when the SPL is above an overall level of about 60 dB. Below this level, the change in the membrane displacement is not proportional to the one in the SPL. This can also be observed in Fig. 2.11, where the decrements of the displacement from 20 dB to 10 dB below 300 Hz did not follow the trend. To measure an even lower SPL, a larger membrane can be used, though the effective frequency range may be reduced as discussed previously. the maximum SPL in these tests was only up to 90 dB due to the rating of the sound source (96 dB maximum). However, the upper limit of the proposed system could be well beyond this, likely above 130 dB.

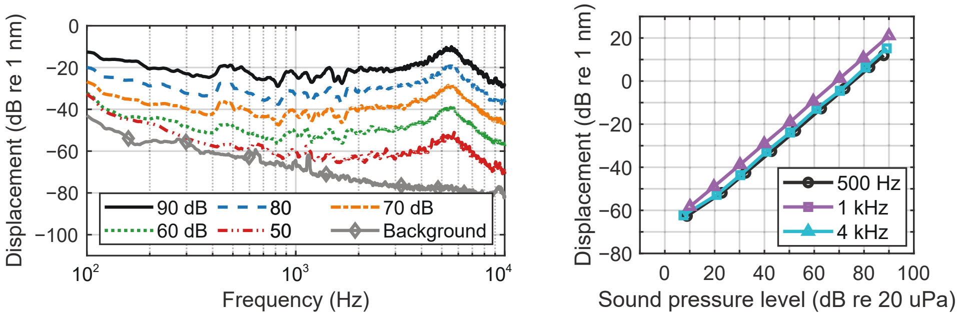

(a) (b)

Figure 2.11: Membrane displacement measurements with different SPLs from (a) an overall value of 90 dB to 50 dB and the background noise of the LDV, and (b) 90 dB to 10 dB measured by a reference microphone at 500 Hz, 1 kHz and 4 kHz.

2.5.3 Total Harmonic Distortion (THD)

The harmonic distortion is an important property in evaluating a microphone for sound measurements. Because the LDV measures the vibration of the target, the main sources contributing to the distortion are anticipated to be the membrane itself and the supporting base. the total harmonic distortion (THD) at a frequency can be calculated with

$$\mathrm{THD} = \sqrt{\frac{A_2^2 + A_3^2 + A_4^2 + A_5^2}{A_1^2 + A_2^2 + A_3^2 + A_4^2 + A_5^2}} \times 100, \tag{2.20}$$

where A_j is the amplitude of the j-th harmonic. the THD spectrum measured by the reference microphone and the constructed membrane is shown in Fig. 2.12. As a well-designed and manufactured sensor, the THD of the reference microphone is small overall, which is below 3% above 150 Hz and below 1% above 300 Hz. the custom-made retro-reflective membrane has a similar result, except for some slightly higher THD at a few frequencies below 300 Hz. Above 300 Hz, the THD for the custom-made retro-reflective membrane is also approximately 1%. When it is used for noise control applications, for example in Chapter 3, the THD is not so severe as to cause any noticeable performance degradation.

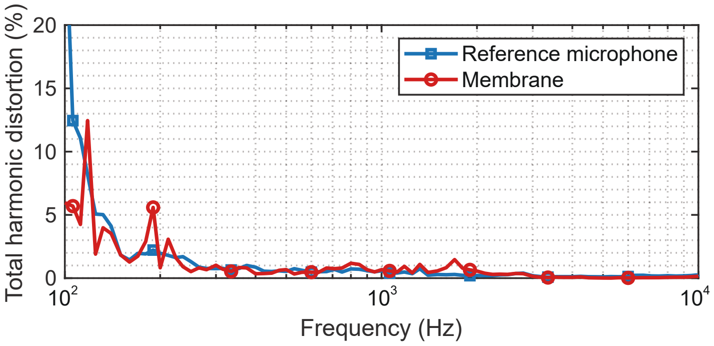

Figure 2.12: THD spectrum obtained by the reference microphone and the membrane specimen.

2.6 Practical Challenges

2.6.1 Laser Beam Incidence Location

The circular membrane displacement $\eta(r,\theta)$ is related to the radial distance r, which is expected to be the most significant at the centre of the membrane. When the laser beam projection point on the membrane deviates from the centre, the detected vibration level drops. the vibration level at the edge should ideally approach zero. However, due to the lightweight nature of the structure, the boundary is not completely free of vibration, particularly in the low-frequency range. Fig. 2.13 shows the experimental results, where five laser beam incidence points on the membrane from the centre to the edge, each separated by 0.7 mm, are shown. the membrane vibration level drops significantly in the higher frequency range for increased distance from the centre. For example, at 5.5 kHz, the sensitivity of the sensor dropped from about 32.7 dB at the centre to about 31.3 dB, 28.1 dB, 14.2 dB and −7.0 dB at off-centre points #1, #2, #3 and at the edge, respectively. Sensitivity is also reduced in the low-frequency range but by a diminished amount. This is primarily caused by the vibration from the whole structure, which mostly occurs at low frequencies. If any deviation occurs in the application, adjustment should be made to equalise the measurement.

2.6.2 Laser Beam Incidence Angle

LDVs have been used for many instruments with polished metallic surfaces, for example, a microphone diaphragm (Suh et al., 2019; Xiao et al., 2021a).

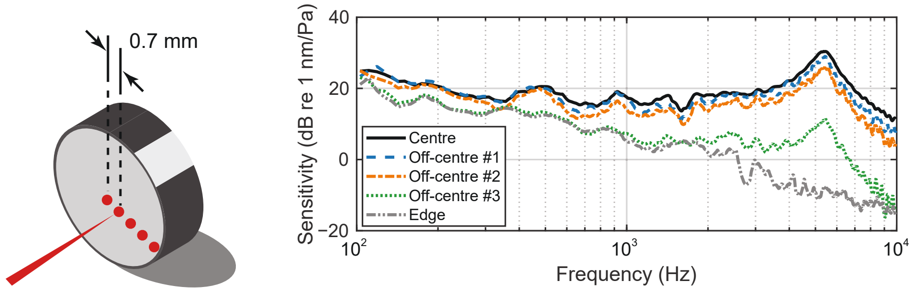

(a) (b)

Figure 2.13: (a) Five evaluation points for the laser beam on the membrane specimen - centre, off-centre #1, off-centre #2 and the edge. the interval of the points is about 0.7 mm. (b) Sensitivity of the membrane specimen at the five points.

However, these mirror-like surfaces only allow the laser beam incidence to be in the normal direction. By using retro-reflective film as the membrane, the laser beam from the LDV can be projected onto the membrane from a wide range of non-normal incidence angles. Fig. 2.14 presents the membrane vibration levels when the laser beam from the LDV was kept at the centre but with various incidence angles. When in the normal direction, the measured membrane vibration level was the most significant. As the incidence angle increases, the overall vibration level reduces. the magnitude of the displacement should be applied with $\cos(\varphi)$ such that it has the most significant value when $\varphi = 0$, that is, the normal direction; it has the least significant value when $\varphi = 90$, that is, the laser beam is parallel with the membrane. For example, at 5.5 kHz, the magnitude was approximately 32.4 dB. When the incident angles are at 10 and 20 degrees, there was no obvious difference, as the difference, in theory, is less than 1 dB. When the incidence is at 30 degrees, the magnitude is reduced to 31.5 dB. At 40, 50 and 60 degrees, the magnitude dropped to 31.0 dB, 29.0 dB and 27.7 dB, respectively. This reduction follows the expectation. When the incidence is below 30 degrees, the reduction in the magnitude is less than 1 dB, which is not large to cause significant errors. When the incidence is beyond 30 degrees, the reduction in the magnitude cannot be neglected and adjustments must be made for correct measurements.

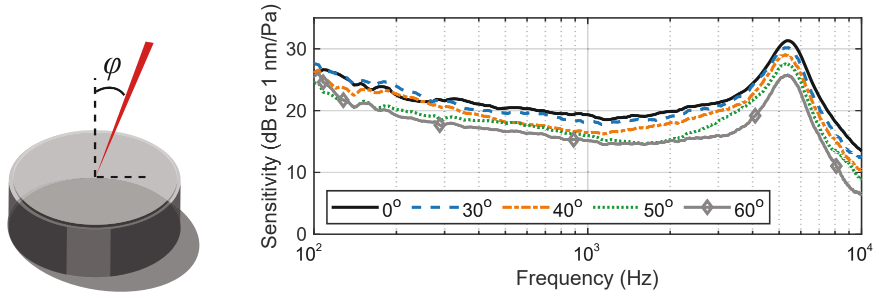

(a) (b)

Figure 2.14: (a) Incidence of the laser beam with an angle φ. (b) Sensitivity of the membrane specimen with different incoming angles.

2.6.3 Signal Delay

Due to the electronic signal conditioning components within the LDV, delay of the measured signal should be investigated. With the configuration and setup shown in Fig. 2.8, signals from the reference microphone and the LDV were recorded synchronously. the distances from the loudspeaker to the membrane and the reference microphone are the same because they are close to each other. Thus, the acoustical transmission delays for the two sensors are the same. By only comparing the displacement signal from the LDV (Polytec NLV-2500-5) with the SPL measurement from the reference microphone, it was found that there was only 3-sample delay when the sampling rate of the recorded data was set to 65.536 kHz, i.e., there is about 46 us delay of the LDV signal with respect to microphone signal.

2.7 Summary

A remote acoustic sensing apparatus that consists of a retro-reflective membrane and an LDV at a remote location has been reported. This system can measure acoustical pressure signals at remote locations with a minimal instrumentation footprint. The small circular membrane pick-up without any cables can be placed at the location of interest, whereby an LDV can then measure the acoustically induced membrane surface vibration at that remote location. The membrane was purposefully chosen to be retro-reflective to allow a wide range of LDV laser beam incidence angles. The sensitivity of the proposed sensor was calculated, and the noise floor of the LDV and the THD were reported. In addition, some practical issues in applications, such as the exact laser beam incidence location on the membrane, the incidence angle and the signal latency, were addressed. The demonstrated membrane has a working frequency range from 200 Hz to 4 kHz, which is sufficient in some acoustic sensing, speech measuring applications.

However, it should be noted that there are some factors potentially limiting the functionality of the proposed system. First, although the system allows for remote and wireless acoustic measurements, small membranes are still required as the acoustic pick-ups. Second, since the measurements are made from the LDVs placed at a remote location, the paths for the laser beams must be cleared and thus the placement of these devices can be limited. One possible solution can be to include one or multiple small galvanometer-driven beam-steering mirrors to redirect the laser beams depending on a specific application. Last, the laser beams from LDVs might be disturbing or hazardous particularly when human users are involved. Although eye-safe, such a system should be designed such that these hazards shall be minimised.

Future work will include designing the membrane to yield a solution with a wider frequency range. For example, using a thinner material (e.g., graphene) treated to be retro-reflective can possibly be used to both broaden the frequency range and improve the sensitivity.

CHAPTER

3

ANC with Remote Error Sensing

3.1 Introduction

Long-term exposure to either occupational or environmental noise can lead to a series of diseases, both auditory (Zhou & Merzenich, 2012) and non-auditory (Stansfeld et al., 2005; Stansfeld & Matheson, 2003). ANC headphones are commonly used by passengers and aircrew in aircrafts, where the cabin noise during long haul flights is known to be detrimental to health and wellbeing (Stansfeld et al., 2005; Zevitas et al., 2018). However, longer-term use of such solutions can cause discomfort and/or fatigue because of the requirement to create a sealed volume around the ear which requires extra earcup clamping pressure. Solutions that can deliver sound reduction performance on par with that of earmuffs-based ANC headphones, but without the need to wear anything, would have value in many scenarios such as for machinery or equipment operators, for drivers of vehicles and for people working in open plan offices.

A substantial amount of effort has been made to move the required secondary loudspeakers and error sensors of ANC systems away from the user's ears and head while still realising effective noise reduction (Buck et al., 2018; Elliott & Jones, 2006; Garcia-Bonito et al., 1997; Jung et al., 2019; Olson & May, 1953; Rafaely et al., 1999). Indeed in an ANC headrest system (also known as an active headrest in some literature), both the secondary loudspeakers and the error microphones can be installed within the seat to reduce the primary sound at both of user's ears (Olson & May, 1953). Due to the difference between the sound pressure measured at these remote microphone locations and that at the user's ears, such a solution cannot guarantee sufficient sound reduction, particularly in the higher frequency range. Since the first proposal of ANC headrest technology in 1953 (Olson & May, 1953), many virtual error sensing algorithms have been proposed which estimate the sound pressure at the ears based on the signals obtained from physical microphones positioned at alternative remote locations (Cazzolato, 1999; Elliott & David, 1992; Elliott et al., 2018; Jung et al., 2018; Moreau et al., 2008; Roure & Albarrazin, 1999). The upper-frequency limit for effective sound control remains relatively low with a recently proposed system consisting of an array of four microphones and a head tracking system still only achieving sound reduction up to 1 kHz for a single sound source (Elliott et al., 2018; Jung et al., 2017, 2019). While this may be sufficient for certain low frequency ambient or machine induced noise, it is less effective for speech or other higher pitch sounds. In addition, the number of microphones required can be significant when using such a technique for real-world applications; this is not desirable in many applications.

In this chapter, a remote acoustic sensing approach using an LDV (Rothberg et al., 2017) and a small membrane "pick-up" is examined in a real-time ANC headrest system. This arrangement includes a retro-reflective film as the membrane pick-up located at the user's ear with an error-sensing LDV being positioned at a location remote from the user. Chapter 3.2 describes the remote error sensing system design, which also includes the ANC algorithm used in the system, the developed head tracking system and the optimal placement of the membrane. Chapter 3.3 demonstrates the ANC performance of the proposed system dealing various types of noise and when the head motion from the user is present. Chapter 3.4 extends the demonstrated system even further by using the parametric array loudspeakers as the secondary sources. Some discussions are provided in Chapter 3.5 and then it is summarised in Chapter 3.6.

3.2 System Design

LDVs typically have very high sensitivity with commercially available instruments able to resolve vibration displacements down to pm and velocities down to nm/s resolution. The membrane pick-up can be designed to be small and lightweight and have a wide dynamic range. Furthermore, being retro-reflective, the membrane can tolerate a wide range of inbound laser beam incidence angles, making this combination suitable even when the user's head moves (in combination with measurement point tracking as also described). Importantly, however, such a remote acoustic sensing approach can be highly attractive in an ANC application because the bulk of the signal processing components are located away from the user. The only minor encumberment on the user, to yield a practically realisable solution, is that they must wear a small optical pick-up, of no more mass nor volume than a typical piece of ear jewellery, on or ideally close to each ear canal.

Since the system does not include any largely intrusive actuators, sensors or bulky materials around the user's ears, it is described as a "virtual ANC headphone". It neither installs any bulky error microphones with accessories on or near to the user's head, nor uses a large number of microphone arrays with certain virtual sensing algorithm methodologies to estimate the sound pressure at the ears based on measurements from elsewhere. As will be shown in the remainder of the chapter, this virtual ANC headphone system has significantly better performance than any other virtual error sensing solutions in the published literature thus far. While there remains further work to yield a commercially viable practical version of the solution, it is proposed that the technical benefits justify its proposal and continued investigation.

A schematic showing the proposed system components and their arrangement is shown in Fig. 3.1. Two secondary loudspeakers are placed behind a user's head (as they would be if integrated into a headrest), one at either side to control the primary sound from the surrounding environment at each ear and to thereby place the user in a quieter environment. An LDV is used to determine the acoustical signal at the ear canal entrance by measuring the surface vibration of a small, lightweight and retro-reflective membrane pick-up located nearby. While Fig. 3.1a shows two inbound laser beams, one to each ear, a single-ear solution is considered and described herein for the sake of brevity and clarity but with no loss of generality for the two-ear equivalent.

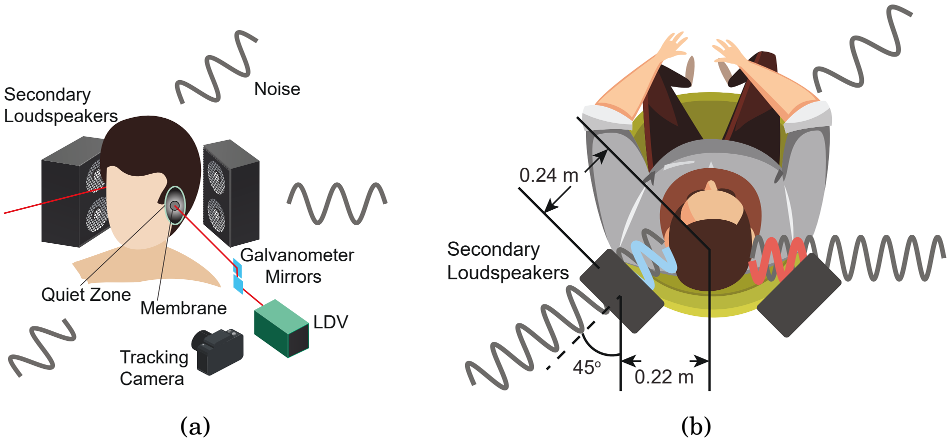

Figure 3.1: A virtual ANC headphone. (a) A quiet zone is formed in each ear by using a nearby secondary loudspeaker pair to reduce the sound in the ear, the required error signal being determined from an LDV measurement of the vibration of a small membrane pick-up located close to the ear canal. Movement of the user is accommodated by a camera-based tracking system, which actively controls the galvanometer-driven mirrors to steer the laser beam and maintain its position on the membrane. (b) The locations of the secondary loudspeakers. Each secondary loudspeaker generates anti-noise signals through the ANC controller (not shown).

For ANC systems, a quiet zone is defined as a region in which more than 10 dB sound attenuation is achieved, with the zone size being about a tenth of the wavelength of the sound in a diffuse sound field (Nelson & Elliott, 1991). When the membrane is placed close to the ear canal, such a quiet zone can be created around it, thereby reducing the sound propagating to the tympanic membrane (eardrum). The two secondary loudspeakers presented here were placed 0.44 m apart with an azimuth angle of 45 degrees pointing to the user as shown in Fig. 3.1b. The controller takes the surface vibration velocity of the membrane from an LDV as the error signal for the adaptive control, the details of which can be found in the Methods - Noise control algorithm subsection.

Normal head movements can be accommodated by a relatively straightforward camera-based tracking system, outlined in Fig. 3.1a, which actively controls a pair of orthogonal, galvanometer-driven mirrors to maintain the probe laser beam incidence on the centre of the membrane. Through the application of a bespoke image processing algorithm, the LDV can thereby remotely obtain the acoustical error signal in real-time.

The experimental setup is presented in Fig. 3.2a. The experiment was

Table 3.1: The measured parameter values of the retro-reflective material used in the system.

Parameters	Symbol	Value	Unit
Thickness	h	0.1	mm
Density	ρ_{M}	204	kg/m^3
Tension	T	33	N/m
Young's modulus	E	205	MPa

performed in a quiet room with a background sound pressure level of 38.5 dBA (A-weighted SPL, dB re. 20 uPa). A head and torso simulator (HATS, Brüel & Kjær Type 4128-C) with right and left ear simulators was used to measure the sound that would be experienced at the eardrums in a user's ears. Fig. 3.2b shows the design and the configuration of the membrane pick-up used in this system. The pick-up consists of a piece of retro-reflective film (3M - Scotchlite Sheeting 7610) (Burgess et al., 2011b), 0.1 mm in thickness, stretched over and adhered to a short, enclosed polymeric cylindrical tube with a diameter of 9.2 mm, a depth of 4.6 mm and a mass of approximately 0.2 g. The resulting combination is therefore as minimally invasive as practically possible in terms of size and mass. The film was used as the membrane so as to maximise the backscattered optical signal in relation to the inbound laser beam, irrespective of a non-normal beam incidence, this being advantageous in the presence of inevitable head movements. The membrane works similarly to a microphone diaphragm, converting the acoustical pressure induced mechanical vibration ultimately to an electrical signal. However, in this case, there is neither any electronic components inside (e.g. a preamplifier to process the measured signal), nor the need for wiring for signal transmission. Instead, signal conditioning and conversion are completed remotely in the LDV opto-electronics. Detailed parameters for the retro-reflective material and the frequency response of the membrane pick-up have been determined and can be found in Figs. 3.3 and 3.4 and the Table 3.1.

It should be noted that the laser type used in the experiment was the Class 2 Helium-Neon 633 nm. While eye-safe, it may cause an undesirable effect and distract/dazzle the user if visualised, even briefly. Alternatively, invisible infrared-based LDVs could be used in future developments.

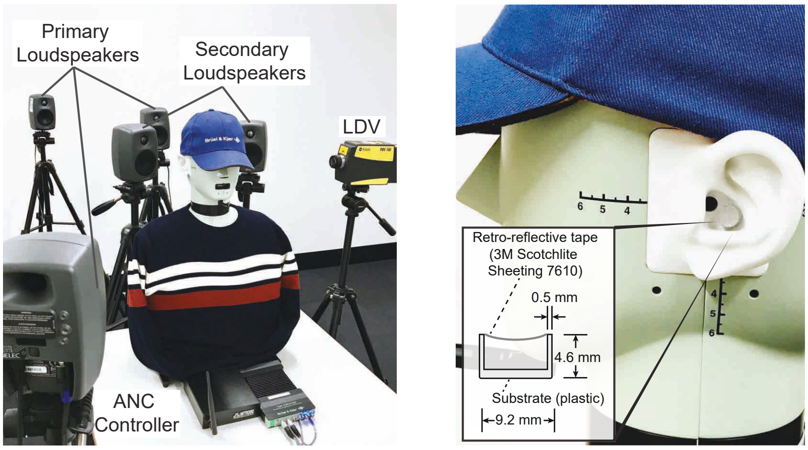

(a) (b)

Figure 3.2: Experimental setup for a stationary HATS. (a) Two secondary loudspeakers were placed behind the HATS for sound control. Multiple primary loudspeakers (three shown) were located arbitrarily to simulate unwanted sound from different directions. The probe laser beam from the LDV was directed toward the membrane in the ear. (b) A membrane was placed close to the ear canal of the left synthetic ear of the HATS. The LDV remotely determines the surface velocity of the membrane as the error signal for the ANC controller.

The data acquisition system is at a remote location along with the LDV in the proposed arrangement. The LDV (Polytec PDV-100) has a measurable frequency range from 20 Hz to 22 kHz. The LDV was mounted on a tripod, vibration isolated from the HATS and the loudspeakers (Genelec 8010A). The sampling rate of the ANC controller (Antysound TigerANC WIFI-Q) was set to 32 kHz, and the filter lengths for both primary and secondary paths were set to 1024 taps. It should be noted that the adaptive control algorithm simply took the measured membrane velocity signal directly and attempted to minimise it. While the velocity signal could potentially be converted into sound pressure by some means, this was not necessary - the outcome would be the same whether it be the raw signal or some derivative of it.

3.2.1 ANC Algorithm

The ANC controller uses the feedforward structure with the filtered-x least mean square (FxLMS) algorithm (Hansen et al., 2012). The block diagram of the algorithm is shown in Fig. 3.5. Subscripts L and R are used in place of “Left” and “Right”. For each side of the ear, the reference signal $x(n)$ was

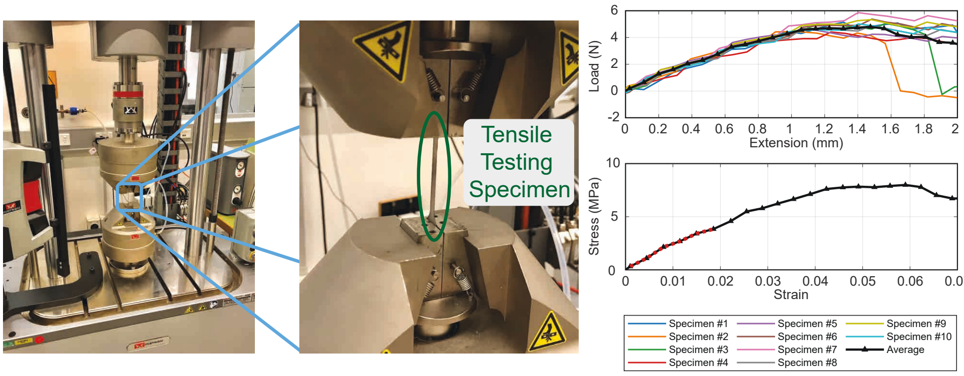

(a) (b)

Figure 3.3: (a) Photos of the tensile testing using an Instron ElectroPuls E10000 Test System to determine the properties of the retro-reflective material used in the system. Ten ASTM dog-bone specimens were cut out for the tensile testing. (b) Top - The load-extension curve of ten specimens from the tensile testing and the average value. Bottom - The stress-strain curve of the average value converted from the load-extension curve. The dotted part shows the elastic region of the testing material.

taken from the primary source for the adaptive ANC controller to calculate the control signal $y(n)$ for the secondary loudspeaker. An LDV measures the error signal $e(n)$, which can be represented as

$$e(n) = p(n) + \mathbf{w}^{\mathrm{T}}\mathbf{r}(n), \tag{3.1}$$

where $\mathbf{w}$ is the vector of controller coefficients and $\mathbf{r}(n)$ is the estimated filtered reference signal vector, with $\mathbf{r}(n) = \hat{s}(n) * \mathbf{x}(n)$, where $\hat{s}(n)$ is the impulse response of the estimated secondary path filter and $\mathbf{x}(n)$ is the reference signal vector. The * symbol represents signal convolution. The controller coefficients are updated with

$$\mathbf{w}(n+1) = \mathbf{w}(n) - \mu\mathbf{r}(n)e(n), \tag{3.2}$$

where μ is the convergence coefficient. The error signal $e(n)$ in this case is the membrane surface vibration velocity measurement from the LDV.

3.2.2 Head Tracking System

The LDV used with the tracking system was a Polytec NLV-2500-5 laser vibrometer, which was placed about 0.3 m away from the left ear of the HATS. The measurement sensitivity was set to 5 mm/s/V leading to a typical velocity resolution of 20 nm/s/$\sqrt{}$Hz (Polytec GmbH, 2019). The controller used in the

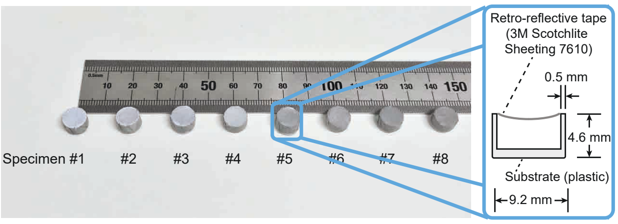

(a)

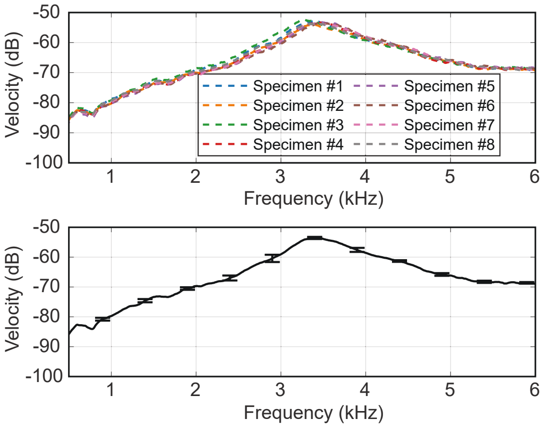

(b)

Figure 3.4: (a) Eight nominally identical membrane specimens were used to determine the surface vibration frequency response performance. Membranes were placed in an environment within a semi-anechoic chamber and subjected to white noise excitation from a nearby loudspeaker. An LDV (Polytec PDV-100) was used to measure the resulting surface vibration from the centre of each membrane. (b) Top - The frequency response of the eight membrane specimens. Bottom - The mean value of the eight membrane specimens.

demonstration for the object tracking was a Raspberry Pi 3B+, accompanied by a 30 fps, 5MP Omnivision 5647 camera module. A circular piece of yellow tape was adhered to the ear lobule as a marker for object tracking purposes (shown in Fig. 3.6). After setting the laser beam to the centre of the membrane in the initial, stationary head stage, the controller detected any subsequent movement of the marker and therefore of the membrane. The movement of the membrane can then be translated into the movement of the marker in the controller. Revised galvanometer outputs, which are directly related to the position of the point-of-interest in two orthogonal directions (x and y) in the plane of the motion, were derived. An MCP4725 digital-to-analogue converter was used to convert the digital signals from the Raspberry Pi to analogue voltage signals for the galvanometer mirror controller. The galvanometer mirrors were from GSI Lumonics with a matching, tuned for position, precision

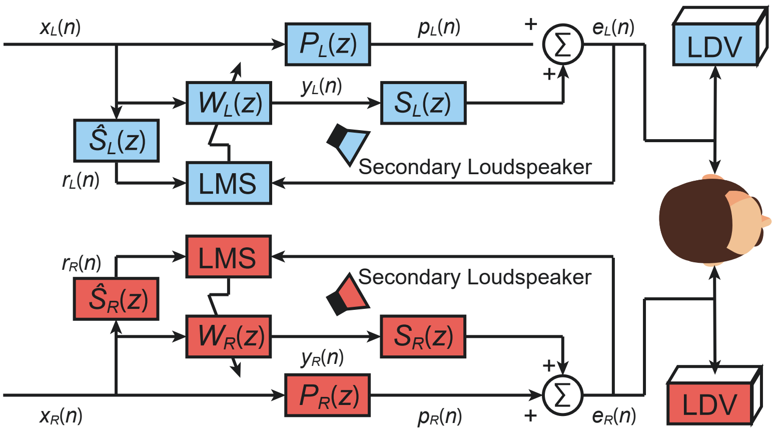

(a)

Figure 3.5: The block diagram of the adaptive active control algorithm for controlling the vibration velocity of the membrane measured by an LDV at each ear. At each side, the error signal is controlled separately by the corresponding secondary loudspeaker instead of being controlled simultaneously.

driver, MiniSAX. As a result, the steering mirrors adjusted the laser beam path such that it remained on the membrane enabling the LDV to measure the membrane surface velocity as the error signal for the ANC system.

The recognition of the object was implemented through colour extraction in OpenCV. The marker was extracted using an adequate threshold of a series of colour images. The image becomes binary as

$$B(x,y) = \begin{cases} 1, & (I(x,y) \geq \lambda) \\ 0, & (I(x,y) < \lambda) \end{cases}, \tag{3.3}$$

where $I(x,y)$ and $B(x,y)$ are the pixel value of the original image and the binarised image, respectively. λ is the threshold for the chosen marker.

Due to the circular shape of the marker, the mass centre of the target object can be readily determined, this being the centre of the marker. Between adjacent frames, the pixel shift of this centre was used to obtain the moving velocity of the object $\mathbf{v}_\mathrm{p}(x,y)$. This in turn can translate to the velocity of the target object in reality $\mathbf{v}_\mathrm{r}(x,y)$, which is expressed as

$$\mathbf{v}_\mathrm{r}(x,y)|_D = \beta \mathbf{v}_\mathrm{p}(x,y), \tag{3.4}$$

where β is a scaling factor for a given distance D between the camera and the target object. The value of β was determined during the setup and calibration stage, where the parameters of the tracking system, such as the distance D and the offset between the marker and the membrane, were specified.

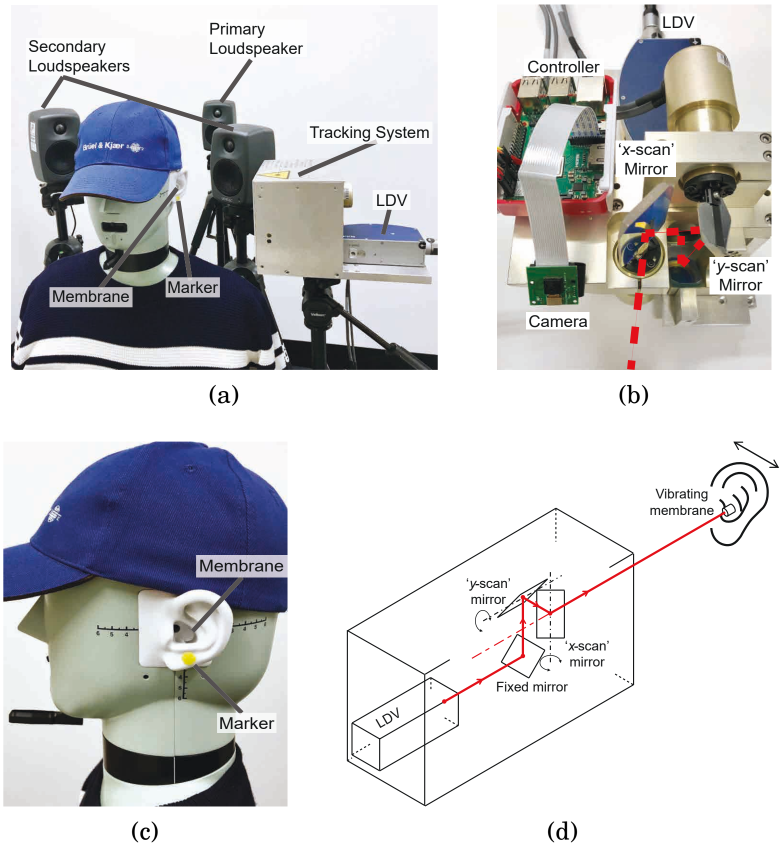

Figure 3.6: (a) Configuration of the head tracking system with a single primary loudspeaker. The tracking system and the LDV are placed to the left side of the head. (b) The construction of the tracking system with a pan and a tilt mirror for steering the laser beam. The camera is attached to the controller for the target object tracking. (c) A yellow marker is placed below the membrane on the ear lobule as the target object. (d) Schematic of the camera-based tracking system showing the laser beam path from the scanning LDV.

3.2.3 Membrane Placement

Although obvious to place the membrane pick-up as close to the ear canal as possible, it is not immediately clear which specific location/s were more feasible/optimal and what the ANC performance might be for each. Four possible pick-up locations are considered, where location #1 is on the anterior notch of the pinna, location #2 the tragus, location #3 the cavum concha, and location #4 the lobule. The experiments were performed in the left synthetic ear of the HATS. Only one loudspeaker, located 0.6 m away directly to the rear of the HATS, is used here as the primary source. The primary source signal was a broadband grey noise with a customised Fletcher-Munson curve

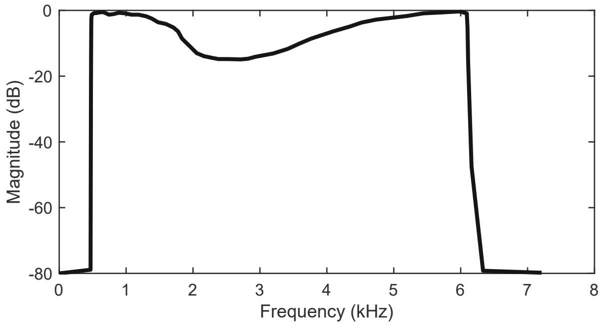

Figure 3.7: The spectrum of a customised Fletcher-Munson curve filter.

filter (Fletcher & Munson, 1933) from 500 Hz to 6 kHz* shown in Fig. 3.7. The filter was applied here to yield a measured SPL with a flat frequency response inside the HATS. The overall SPL at the left tympanic membrane was 77.7 dB (re. 20 uPa - omitted hereafter for brevity) with ANC off.

The ANC performance is presented in Fig. 3.8. With ANC on, the performances at locations #1 and #2 were similar with the overall SPL being 69.2 dB and 70.9 dB, respectively. However, the sound reduction was only significant at frequencies below 4 kHz. The reason may be that the sound pressures measured at these two points are only similar to that at the ear canal below 4 kHz. Thus, the control performances at the two points are also limited up to 4 kHz. The sound reduction at location #3 was the best with an overall SPL of 63.5 dB when ANC was on. The overall SPL was reduced by 14.2 dB over the entire frequency range from 500 Hz to 6 kHz. Location #4, the lobule, was further away from the ear canal than any of the other selected locations. The effective frequency range of the sound reduction was only up to approximately 3 kHz with an approximately 6 dB increase in fact observed over the 5 to 6 kHz range†. Based on the outcomes from this membrane location performance analysis, location #3 (the cavum concha) was identified as the optimal location for the membrane; in the remaining experimental investigations described herein, this is therefore the membrane position employed.

---

*The work presented herein focuses on the high frequencies above 500 Hz. When ANC headrest is used in an enclosure, e.g., in a vehicle cabin, global control works well below 300 Hz (Elliott, 2000), and thus lower frequencies are not considered.

†There are possible solutions to improve the ANC performance when the membrane cannot (or not preferred to) be placed at location #3. One possible solution is to use a remote sensing technique (e.g., RM, VMC, or AF-VS as reviewed in Chapter 1.3.2). This issue will be further discussed in Chapter 7.2.

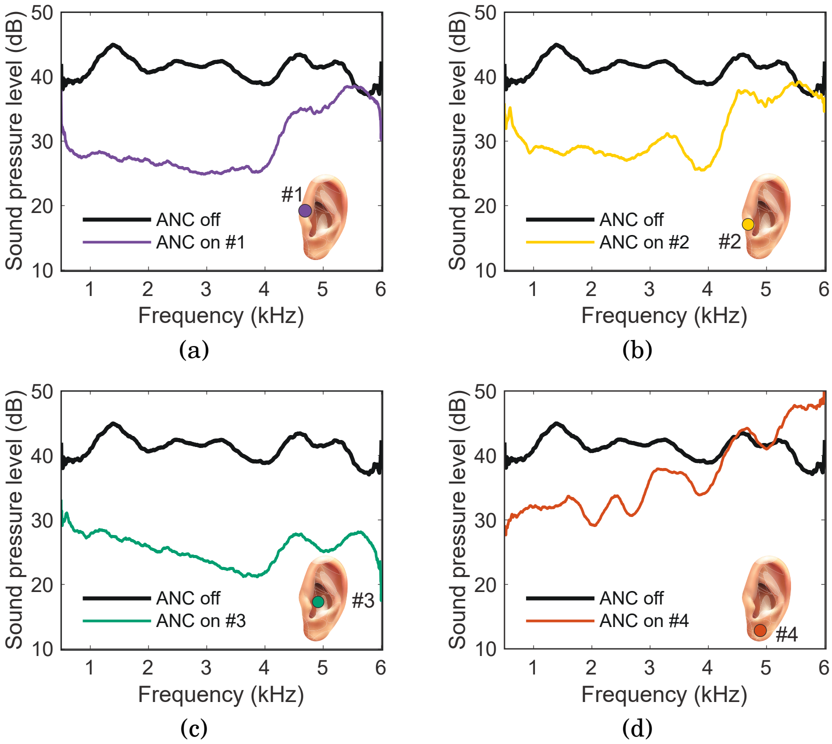

Figure 3.8: The SPLs (dB re. 20 uPa) measured from the left ear simulator of a HATS, simulating the sound that a user experiences at the left tympanic membrane with and without ANC, when the membrane was at (a) location #1 - anterior notch; (b) location #2 - tragus; (c) location #3 - cavum concha; and (d) location #4 - lobule of the HATS left synthetic ear.

3.3 ANC Performance

3.3.1 Broadband Noise

Fig. 3.9 shows the measured noise spectra for each ear without and with ANC for three different primary sound field scenarios. Loudspeaker(s) driven with common signals were arranged to create increasingly complex surroundings with one or multiple reflectors. The signal used was again the broadband grey noise equivalent to that used to obtain the results presented in Fig. 3.8. All the test results were obtained by averaging over a 15-second data length. Fig. 3.9a shows the setup where a single primary source was located 0.6 m away directly to the rear of the HATS to simulate the sound coming from a nearby source without considering any reflections from the surroundings. After enabling ANC, almost 15 dB attenuation was realised with the overall

SPL[*] being reduced from 78.1 dB to 63.8 dB and from 77.3 dB to 62.0 dB at the left and right ears respectively. This scenario is similar to that presented in the current state-of-the-art system (Elliott et al., 2018), where the sound up to 1 kHz was controlled, albeit here the improvement achieved is over a much wider frequency range, up to 6 kHz. Note that the tests were still performed at each side separately instead of being taken simultaneously in this case.

Fig. 3.9b shows the setup and results from a situation in which two primary loudspeakers were placed arbitrarily at two different locations. This can represent a situation when the user is close to a large rigid reflecting surface, such as a table or a wall. In this case, the acoustic signals from the original source and the reflector are coherent. Approximately 13 dB attenuation was obtained with the overall SPLs being reduced from 80.2 dB and 77.9 dB to 66.0 dB and 65.2 dB at the left and right ears, respectively. Fig. 3.9c shows a more general situation where multiple reflectors exist. Four primary loudspeakers were arbitrarily positioned at various locations around the head to achieve this. Approximately 11 dB attenuation was obtained with the overall SPL reduced from 80.4 dB to 68.9 dB and from 80.1 dB to 69.4 dB at the left and right ear respectively. In all three of these example scenarios, the demonstrated system yielded a minimum 10 dB reduction across the entire 500 Hz to 6 kHz frequency range. It is worth noting that the placements of these primary sources were created arbitrarily, however, the control performances observed are expected to be similar for any other similar configuration.

To examine the effects of the noise floor of the LDVs, different levels of the primary source signal have been studied. Similar to the reference (Elliott et al., 2018), where the primary source was placed about 1.2 m directly behind the HATS, the right ear was controlled using the proposed method. Three tests were performed with the grey noise described in the manuscript as the primary sound. These tests were carried out in a hemi-anechoic chamber to eliminate the interference from other sound sources. Note that the background SPL in the chamber is about 23 dBA. This background noise observed by the HATS is slightly higher than this value due to the ear simulators.

The ANC results of the error signals from the LDV and the SPLs observed by the HATS are shown in Fig. 3.10, and the corresponding overall values are

---

[*] The overall SPL sums the energy at all the frequencies. It is calculated as SPL (dB) = $10\log_{10}\left(\frac{p^2_{\text{overall}}}{p^2_{\text{ref}}}\right) = 10\log_{10}\left(\frac{\sum_{i=1}^{N} p_i^2}{p^2_{\text{ref}}}\right)$, where $p_{\text{ref}} = 20$ uPa, N is the total number of frequencies.

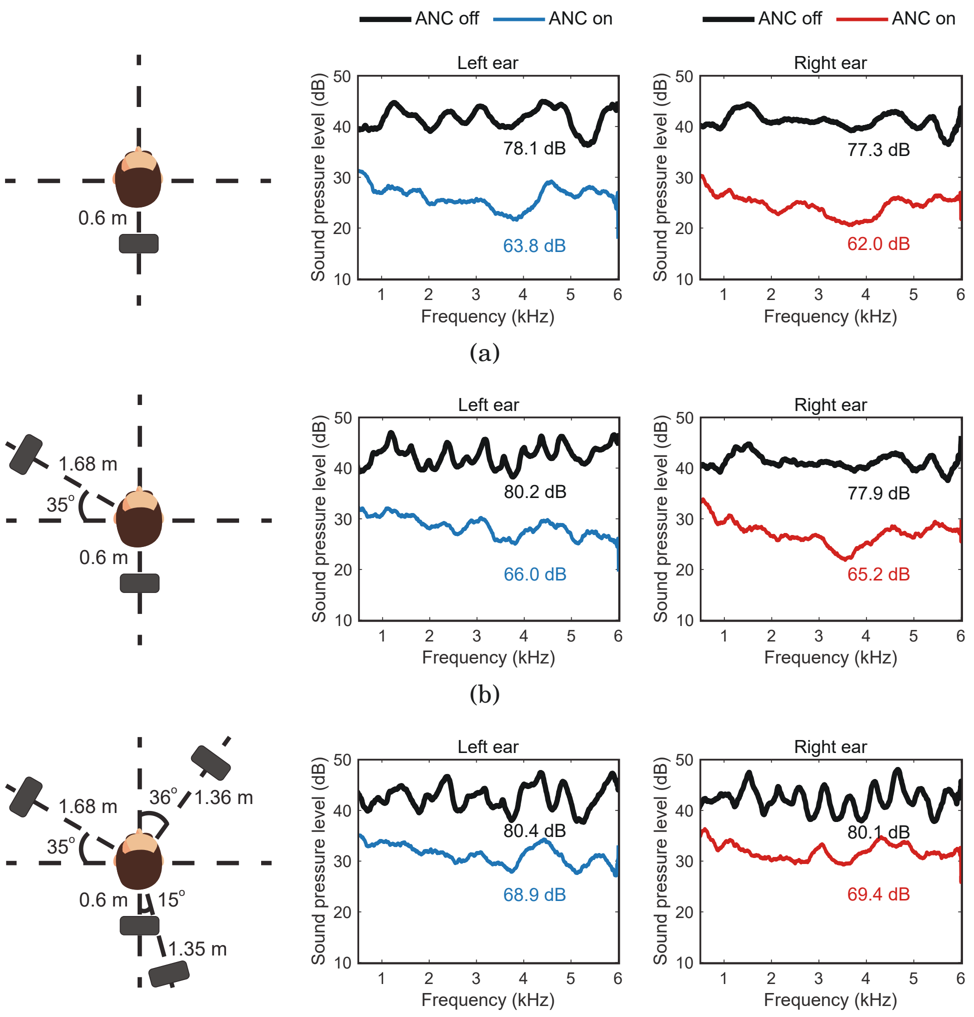

(a)

(b)

(c)

Figure 3.9: Three configurations of the primary loudspeakers and the corresponding SPL (dB re. 20 uPa) with and without ANC at both ears. (a) A single primary loudspeaker was used to simulate the sound from a single source nearby. (b) Two primary loudspeakers were used to simulate two sound sources nearby or a single sound source with a nearby reflecting surface. (c) Four primary loudspeakers were used to simulate sound from multiple directions, approximating a general case in practice.

shown in Table 3.2. It is clear that noise floor of the LDV signal is sufficiently low in these cases and does not cause any problem for the active control in this research. It is also interesting to note that ANC performance observed by the HATS in Test 2 is slightly better than that in Fig. 3.9a. A possible reason is that the background noise in this case is lower than the one presented in Fig. 3.9a with a background noise of about 38.5 dBA.

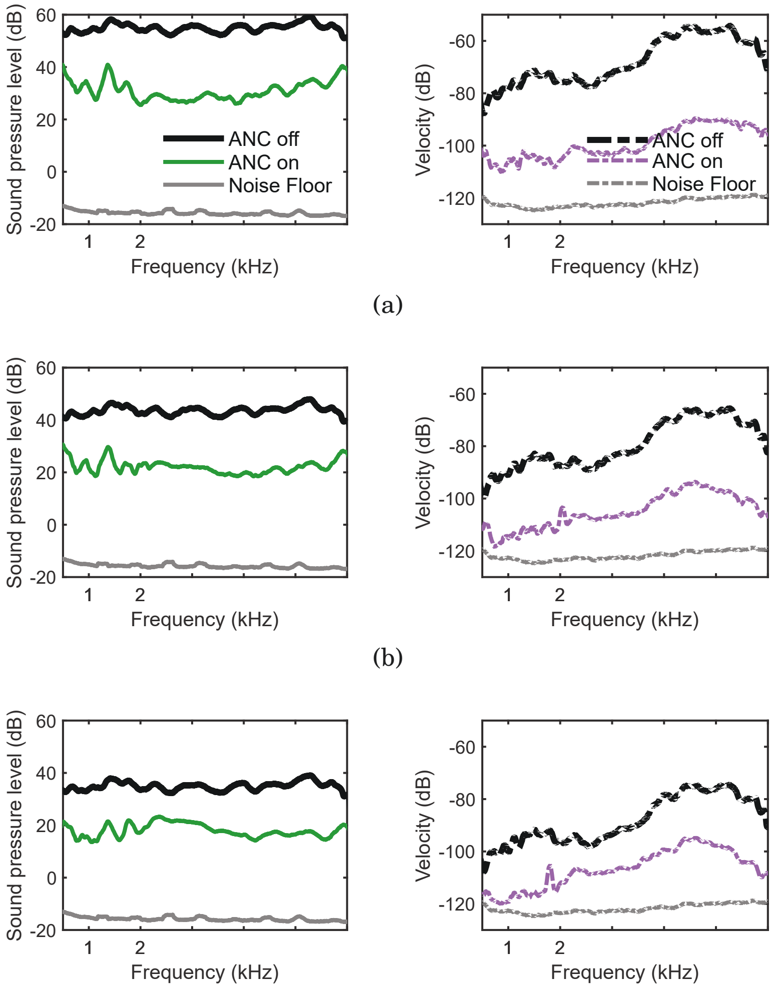

(a)

(b)

(c)

Figure 3.10: The SPLs (left) and the magnitude of the LDV signal (right) without and with ANC for (a) test 1, (b) test 2 and (c) test 3.

Table 3.2: The overall SPL and the velocity from the LDV without and with ANC under three levels of sound.

	Overall SPL (dB)		**Overall velocity (dB)**	
	Without ANC	**With ANC**	**Without ANC**	**With ANC**
Test 1	93.1	71.4	–23.3	–57.5
Test 2	81.8	61.7	–34.7	–63.0
Test 3	73.1	57.0	–43.4	–64.2
Noise Floor	34.3		–83.8	

3.3.2 Environmental Noise

To further demonstrate the capability of the proposed solution, performance in the presence of three different kinds of pre-recorded common environmental noise scenarios was assessed. Similar to the configuration implemented recently, the primary source was located about 1.2 m directly behind the HATS, with only one channel (right ear) being controlled. The three experiments were performed in a hemi-anechoic chamber. Firstly, a recording of aircraft interior noise (Transportation Ambience, 2019) was used as the primary source signal. The 15-second signals observed by the HATS before and after ANC are shown in Fig. 3.11a with the corresponding spectra averaged over this duration also shown. The overall SPL was significantly reduced from 74.7 dB to 59.6 dB - a greater than 15 dB improvement. Secondly, an example of an aircraft flyby noise (Airplane Sound Effects, 2019) was examined. Fig. 3.11b shows the time-domain signal observed by the HATS of such non-stationary noise before and after ANC and the spectrum (averaged from 3 to 8 s only). Again, there was a significant reduction over the 500 Hz to 6 kHz range. Indeed, where the noise was the most pronounced, i.e. from 3 to 8 s, the overall SPL was reduced from about 82.1 dB to 61.6 dB - a greater than 20 dB sound attenuation. Lastly, a recording of a crowd of people talking was used as the primary source signal (BBC Sound Effects, 2019). Fig. 3.11c shows the 15-second time-domain and the frequency-domain signals before and after ANC again. The overall SPL was controlled from 75.5 dB to 59.8 dB; over 15 dB reduction was achieved. Table 3.3 summarises the averaged overall SPLs without and with control using the proposed system for these new scenarios, where 15-20 dB noise reduction up to 6 kHz can be achieved using the proposed system. The audio recordings before and after ANC can be experienced through Supplementary Movie 1. It is important to note that the current state-of-the-art virtual sensing ANC solution, with a quoted upper frequency performance of around 1 kHz, would not yield as impressive a performance as the virtual ANC headphone presented herein since, as can be observed in Fig. 3.11, the more significant frequency content in all three example signals primarily exists in the 2 to 4 kHz range.

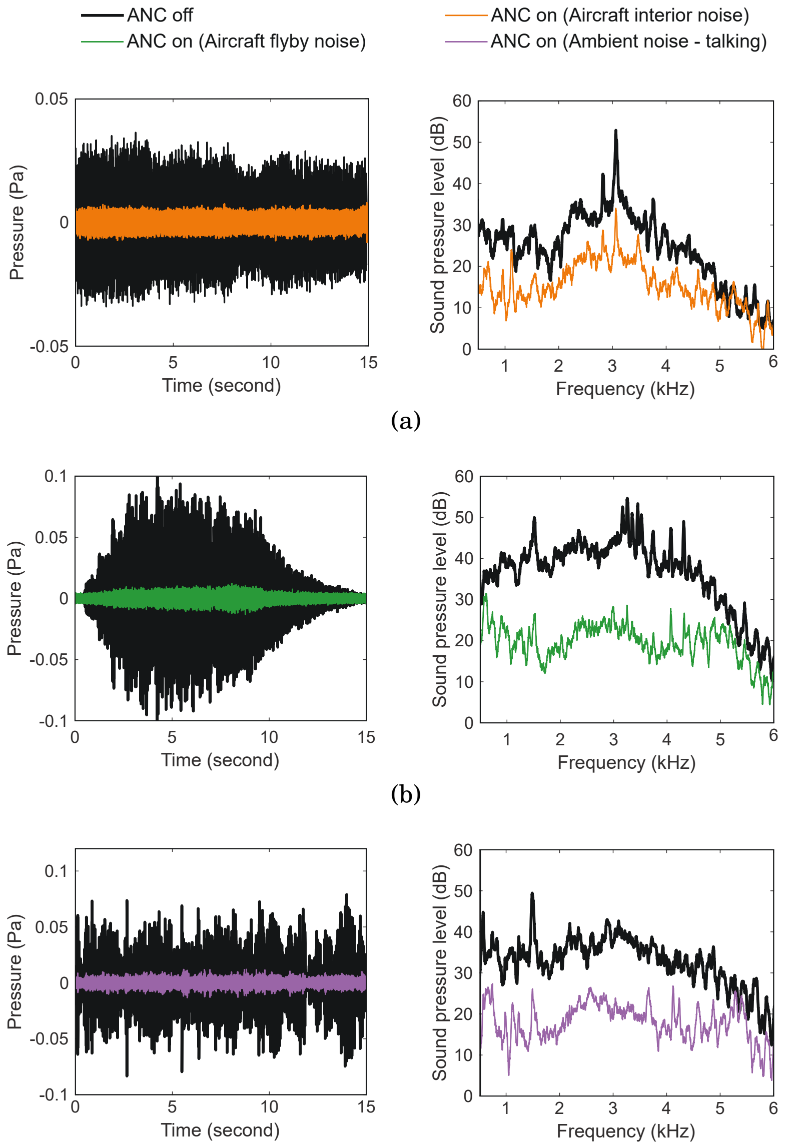

(a)

(b)

(c)

Figure 3.11: The time-domain signal observed by the HATS and the corresponding sound pressure level (dB re. 20 uPa) without and with ANC for (a) aircraft interior noise, (b) aircraft flyby noise and (c) ambient noise of people talking.

Table 3.3: The averaged overall SPL without and with proposed ANC system for three types of synthetic example environmental primary noise.

Noise type (average duration)	**Averaged overall SPL (dB)**		
	Without ANC	**With ANC**	**Noise reduction**
Aircraft interior (0-15 s)	74.7	59.6	15.1
Aircraft flyby (3-8 s)	82.1	61.6	20.5
Ambient speech (0-15 s)	75.5	59.8	15.7

3.3.3 Head Motion

A person is prone to exhibit continuous head motion, therefore, the probe laser beam from the LDV should be able to track the corresponding arbitrary motion of the membrane in the ears. Such tracking LDV solutions have been widely researched, developed and applied for numerous complex measurement tasks (Rothberg et al., 2017); the scenario herein represents a further interesting application. A simple tracking system shown in the previous section was therefore implemented to demonstrate the proof of concept. The scenario used here is the same as the one described in Fig. 3.9a, i.e. that with a single sound source immediately to the rear.

The movement of a marker on the ear lobule of the HATS, as illustrated in Fig. 3.6c was determined by the image processing-based tracking system to maintain near-optimal laser beam incidence on the membrane and yield a useful error signal. Chapter 2 has presented the effects of off-centre measurements and different laser beam incident angles on the system performance. Overall, the performance was not particularly sensitive to the precise location of the laser beam on the membrane, with it therefore deemed not necessary for the laser beam incidence to be precisely at the geometrical centre. With the laser beam slightly off-centre, ANC performance is maintained. Furthermore, the incidence angle of the laser beam did not affect performance significantly. With incidence at a quite remarkable 60 degrees, the LDV signal drops by around 5 dB, which, again, has a minimal detrimental effect on the ANC performance.

To quantitatively examine this, the LDV was placed at another two locations (rotated by 15° and 30°) as shown in Fig. 3.12a; the corresponding SPLs

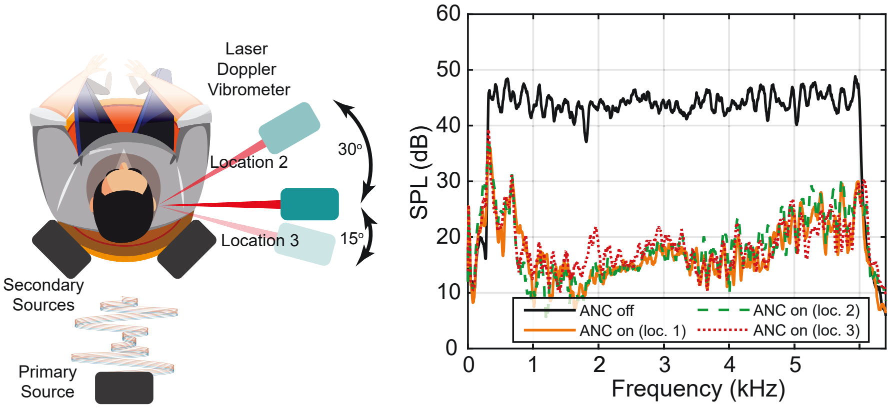

(a) (b)

Figure 3.12: (a) Illustration of the alternative two locations for the LDV. (b) The sound pressure reduction levels observed by the HATS for the grey noise at three locations.

observed by the HATS are depicted in Fig. 3.12b. The control performances with the laser beam from the two alternative angles remained the same as that for the normal incidence. Therefore, using the retro-reflective material makes it possible to maintain the control performance if movements from the user should lead to non-normal laser beam incidence.

Fig. 3.13 shows four control performances - when ANC is off (i) and on (ii) for a stationary HATS and when ANC is on with the head tracking system disabled (iii) and enabled (iv) for a moving HATS. The movement of the HATS was implemented manually with a forward-backward movement used to simulate a person moving back and forth while seated. The maximum distance the HATS travelled in the Supplementary Movie 2 was approximately 0.08 m peak-to-peak with a maximum speed of about 0.04 m/s. Fig. 3.13a shows the 15-second sample of the time-domain measurement for each case with the same configuration as in Fig. 3.9a. Fig. 3.13b shows the corresponding averaged frequency spectrum for each case for the entire duration. Similar to the results previously presented in Fig. 3.9a, the total SPL was reduced from 81.1 dB to 64.1 dB over the frequency range from 500 Hz to 6 kHz range for the stationary situation.

When the HATS moved with ANC on but with tracking disabled, the head (therefore the membrane) moved away from the probe laser beam; the LDV signal thereby “dropped out” or made a vibration measurement not representative of the sound pressure at the ear. This can easily make the

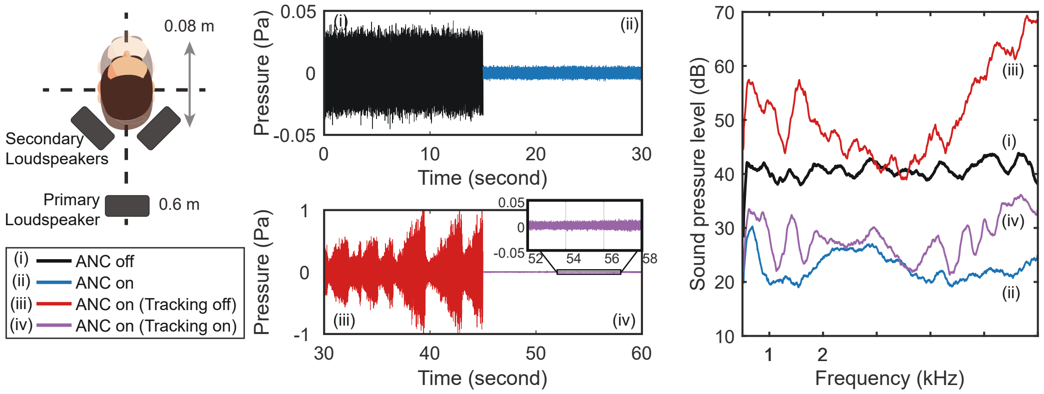

(a) (b)

Figure 3.13: ANC performance with the developed head tracking system. (a) Four 15-second samples of the time-domain signal observed by the HATS. The upper 30 s duration shows the sound pressure with ANC off and on for the stationary situation, while the lower 30 s duration shows the sound pressure with ANC on with the tracking system off and on for a moving HATS. (b) The corresponding sound pressure level (dB re. 20 uPa) of the four signals.

control system diverge and, as shown in Fig. 3.13b, the overall SPL in fact increased significantly from 81.1 dB to 99.5 dB. When the tracking system was enabled, the mirrors maintained the laser beam incidence on the membrane as the HATS moved. Thus, the LDV measurement remained valid for the adaptive control. As shown in Fig. 3.13b, the system reduced the sound from 81.1 dB to 70.4 dB over the entire frequency range. The control performance maintained at least a 10 dB reduction during the movement of the HATS, demonstrating the necessity of using a tracking system for the ANC system. Again, these audio recordings can be experienced in the Supplementary Movie 2.

3.4 Parametric Array Loudspeakers

When a secondary source is used to control the noise at a single location, the size of the created quiet zone is found to be about one tenth of the wavelength of the controlled sound in a diffuse sound field (Elliott et al., 1988a; Guo & Pan, 1998). However, the sound pressures in the other areas might increase due to the sound generated by the omni-directional secondary sources (Guo et al., 1997; Tanaka & Tanaka, 2010). Placing a secondary source close to the control point can mitigate the increase of total energy in the other areas

(David & Elliott, 1994; Joseph et al., 1994), but it brings obstructions to the person. Some studies have demonstrated the capabilities and potentials of using directional loudspeakers to cope with this problem (Hu & Tang, 2019; Tanaka & Tanaka, 2010). For example, a directional source consisting of two closely located loudspeakers with pre-adjusted phase difference have been used to reduce the noise in the shadow zone behind a barrier (Chen et al., 2011).

Parametric array loudspeakers (PALs), where the highly directional audio sounds are generated due to the nonlinear interactions of ultrasonic carrier waves in air, have sharper radiation directivity than existing traditional loudspeakers (Gan et al., 2012). The advantages of using PALs in ANC systems have been demonstrated in a single-channel system where a 1.5 kHz sound wave at the target point was reduced without affecting sound fields in the other areas (Tanaka & Tanaka, 2010). A two-channel ANC system using PALs have been used to reduce the factory noise from 500 Hz to 2.5 kHz (Tanaka et al., 2017). However, the feasibility of using them to reduce the noise with a broader bandwidth remains to be investigated.

As shown previously, the remote acoustic sensing apparatus has been proposed, which placed a custom-made membrane pick-up at the point of interest, and the membrane vibration measured by an LDV was used to determine the acoustic information at the point from a remote location. The membrane pick-up was placed in the person's ear and the estimated signal from the LDV was used as the error signal in the ANC system. It has been demonstrated the upper limit frequency of effective control can be significantly improved up to 6 kHz. Therefore, it is feasible of applying this technique to broaden the effective frequency range of ANC experimentally with a PAL as the secondary source.

3.4.1 System Setup

The experiments were conducted in a hemi-anechoic room with dimensions of 7.20 m × 5.19 m × 6.77 m (height). The schematic diagram and the photos of the experiment setup are shown in Fig. 3.14. A broadband primary noise (1 kHz to 6 kHz) was generated by a traditional loudspeaker (Genelec 8010A) at 6 m away from the HATS. The custom-made membrane was placed in the left synthetic ear of the HATS, and the radius and thickness of the membrane

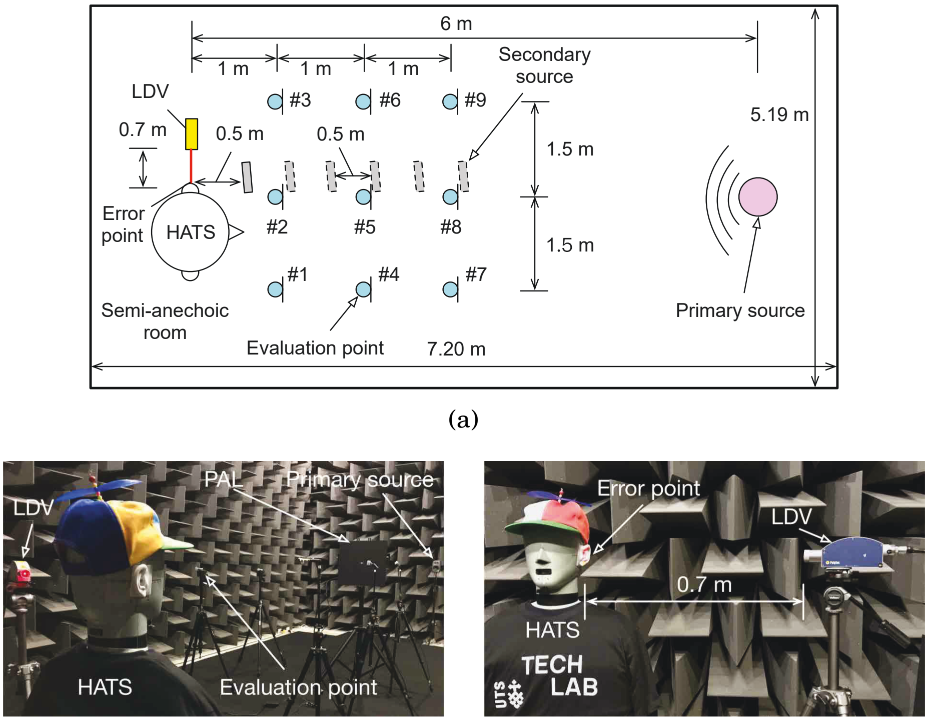

(a)

(b) (c)

Figure 3.14: (a) Schematic diagram of the experiment setup; (b) A photo of the experiment setup in the hemi-anechoic room; and (c) A photo of the LDV error sensing system.

were 10.5 mm and 0.1 mm, respectively. The LDV (Polytec NLV-2500-5) was placed at a stand-off distance of 0.7 m away from the membrane in the left ear. All the equipment was at the same height during the experiments. The error signal was obtained by measuring the vibration of the membrane and was then fed into a commercial ANC controller (Antysound TigerANC WIFI-Q).

A PAL (Holosonics Audio Spotlight AS-16i with the surface size of 40 cm × 40 cm) was used as the secondary source, and the performance of the ANC system using it was compared with that using the traditional omni-directional loudspeaker. Six groups of experiments were carried out, where the secondary source was placed in front of the error point at the distance from 0.5 m to 3 m with an interval of 0.5 m. To investigate the effects of the secondary source on the sound fields in the other areas, 9 evaluation microphones (Antysound Anty M1212) were placed in front of the HATS as shown in Figs. 3.14a and 3.14b. The acoustic signals at all the microphones and the HATS were recorded with a sampling rate of 12.8 kHz. The fast Fourier transform (FFT) analyzer in PULSE Labshop was used to obtain the FFT spectral.

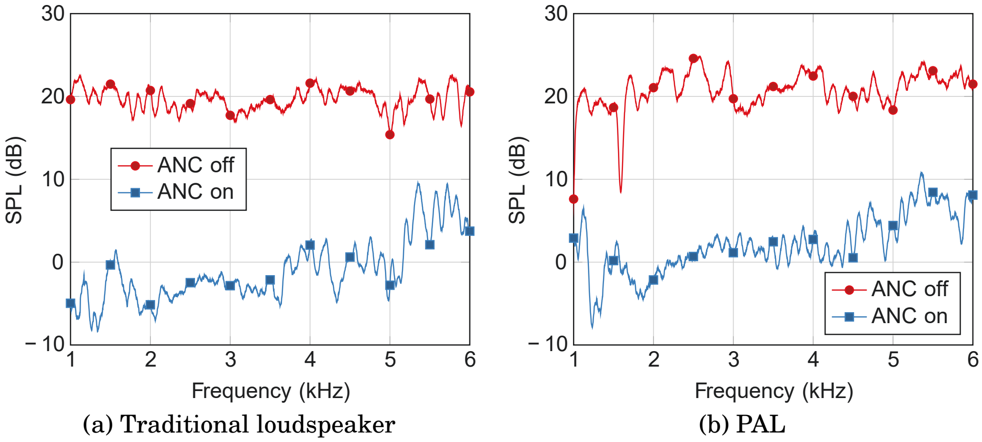

(a) Traditional loudspeaker

(b) PAL

Figure 3.15: The SPLs measured by the left ear simulator of the HATS with and without ANC, where the secondary source was (a) a traditional loudspeaker and (b) a PAL, at a distance of 1 m from the error sensing point.

3.4.2 Experimental Evaluations

Fig. 3.15 shows the SPLs measured by the left ear simulator of the HATS with and without ANC when the distance between the secondary source and the error point was 1 m. The overall noise reductions from 1 kHz to 6 kHz measured by the HATS were 18.7 dB and 17.8 dB when the traditional loudspeaker and the PAL were used as the secondary source, respectively. It is clear that both types of loudspeakers can reduce the noise at the ear effectively. There are two troughs near 1 kHz and 1.6 kHz on the curve of the primary noise without ANC in Fig. 3.15b, which might be caused by the scattering effects of the square PAL used in experiments.

To investigate the effects of the secondary source on the sound fields in the other areas, the SPLs at two typical evaluation points #2 (closest to the secondary source) and #7 (farthest away from the secondary source) with and without ANC are presented in Fig. 3.16, where the distance between the secondary source and the error point was again 1 m. Both types of loudspeakers had little effect on the SPLs at point #7 because it was away from the secondary source as shown in Fig. 3.14a. However, at point #2 which was close to the traditional loudspeaker, the SPLs changed significantly with ANC on due to the omni-directional secondary source, and the overall noise reduction from 1 kHz to 6 kHz of the ANC system was –4.9 dB indicating that the overall sound energy at this point increased with ANC. The overall noise reduction of the ANC system using the PAL at point #2 was only –0.2 dB due to its sharp

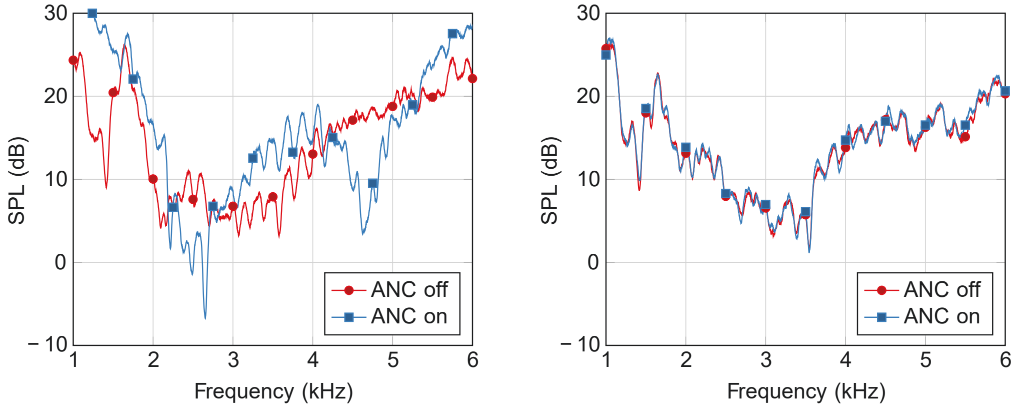

(a) Traditional loudspeaker, Point #2

(b) PAL, Point #2

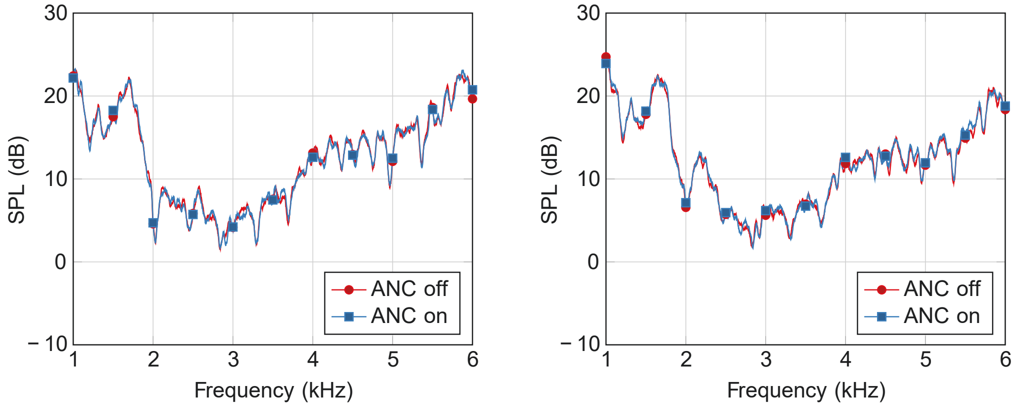

(c) Traditional loudspeaker, Point #7

(d) PAL, Point #7

Figure 3.16: The SPLs at point #2 when the secondary source was (a) a traditional loudspeaker and (b) a PAL; and at point #7 when the secondary source was (c) a traditional loudspeaker and (d) a PAL. The distance between the secondary source and the error point was 1 m.

directivity. Therefore, using a PAL has little effect on the sound fields in the other areas for an ANC system.

Fig. 3.17 shows the overall noise reductions from 1 kHz to 6 kHz measured by the left ear simulator of the HATS and at the 9 evaluation points with ANC on when the distance between the secondary source and the error point, which is denoted by d_{se}, was varied from 0.5 m to 3 m. It can be seen in Fig. 3.17a that the noise reductions using the PAL were similar to those when using the traditional loudspeaker, and are generally between 18 dB and 20 dB. Fig. 3.17b demonstrates that the noise reduction levels at all evaluation points were generally increased as the distance between the traditional loudspeaker and the error point increased. Fig. 3.17c indicates that the sound pressures at

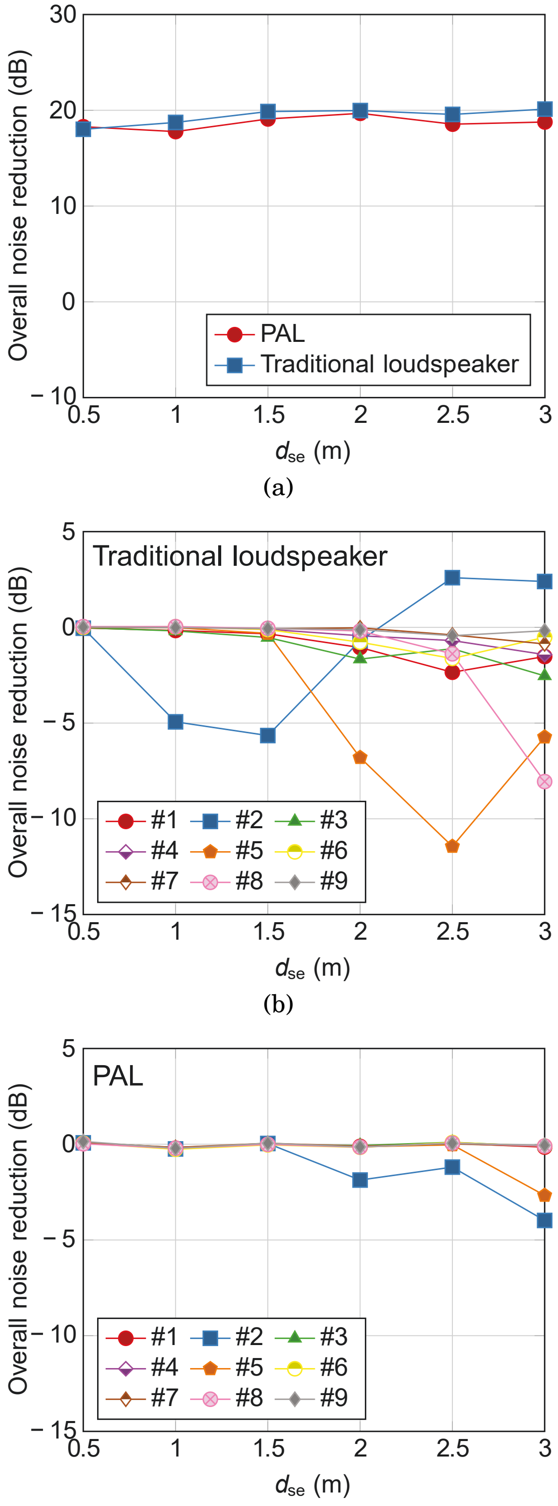

(a)

(b)

(c)

Figure 3.17: Overall noise reductions from 1 kHz to 6 kHz (a) at the left ear of the HATS, and at the evaluation points, where the secondary source was (b) a traditional loudspeaker and (c) a PAL.

evaluation points were almost unchanged with the PAL except at points #2 and #5. The noise reduction levels at these two points were negative, indicating that the sound pressure increased with ANC on. The reason is that the two points were close to the radiation axis of the PAL as shown in Fig. 3.14a, and the SPL variation around them was large with and without ANC. The audio sound waves generated by the PAL decayed slowly by distance, so the amplitude of the generated secondary sounds changed a little when the distance between the PAL and the error point increased. Therefore, the sound pressure in the other areas was less affected by the ANC system when the PAL was used far away from the ear.

The results demonstrate that the overall noise reductions from 1 kHz to 6 kHz at the person's ear were similar with both types of loudspeakers. The SPLs in the other areas were almost unchanged when the PAL was placed away from the ear in the ANC system, while the overall sound pressure levels became higher with the traditional loudspeaker being used at a great distance from the ear. The PAL and the LDV system can be compactly placed away from the person without deteriorating the broadband noise reduction performance.

3.5 Discussions

Like many other systems, the demonstrated solution also faces certain limitations. Particularly, while the demonstrated system using the remote error sensing approach can achieve an ultra-broadband control, the cost (Li et al., 2013) of the required LDVs can be high. However, it is possible that these can ultimately be made smaller and at a lower cost with the entire system thereby being designed to be sufficiently compact and low cost to be used in headrests for example in airplanes or in (driverless) automotive applications in the future.

Some further limitations of the solution are also acknowledged. Firstly, the performance of such a virtual ANC headphone (or ANC headrests in general) is still inferior when compared to that of ANC headphones. In particular, sound attenuation achieved in the higher frequency range by active control is below that which can be simply achieved through passive control, i.e. earmuffs, with these often delivering over 30 dB reduction (Ang et al., 2017; Rudzyn & Fisher, 2012). However, such a comparison is unfair since the aim of an ANC headrest system is to eliminate the use of the passive attenuation materials which deliver such reduction.

Secondly, while multiple primary sources were used to simulate unwanted sound from multiple, arbitrary directions, the reference signals for the ANC controller were taken directly from these loudspeaker signals; in a real-world situation, this would clearly not be possible. The reason for taking the reference signal directly from the primary source was to focus on the proposed remote error sensing approach. Future developments include incorporating one or multiple actual reference sensors into the system. The locations of these reference signal sensors are less constrained than those of the error signal sensors. However, they should still be close to the entire system, including the secondary sources. The constraint of the possible locations would affect the control performance and this remains a topic to be further studied in Chapter 4.

Thirdly, the head tracking system shown for illustration purposes was only capable of tracking two-dimensional motions. A more robust head tracking system with a higher frame rate camera and auto-focus could be implemented to accommodate faster, three-dimensional head movements in the future.

Lastly, it has been demonstrated that PALs can be used as secondary sources to control noise at high frequencies from 1 kHz to 6 kHz. However, it may be commanding for PALs to control low frequencies, e.g., below 500 Hz. This is due to the inherent issue of the PALs, which have a poor response at low frequencies. For example, Yoneyama et al. (1983) showed that the pressure generated by a PAL, $P_s(\omega)$, is proportional to ω^2, where ω is the angular frequency. Thus, at low frequencies, the amplitude of sound pressure is much lower than that at high frequencies. Other works that employed PALs for ANC applications have also faced a similar problem where noise below 500 Hz is difficult to control (Tanaka et al., 2017; Tanaka & Tanaka, 2010). This topic remains to be studied further in the field.

3.6 Summary

The performance of an ANC headrest using a remote error sensing approach, proposed to provide a significantly quieter environment for a user, is investigated. The approach uses an LDV and a small, lightweight and retro-reflective membrane pick-up placed in the cavum concha of a user's ear, thereby producing as little disturbance as possible. The membrane design was presented and analysed, and the effects of its location on the system performance were explored. The noise spectra in the ears without and with ANC for different primary sound fields and diverse kinds of environmental noise were reported. A simple head tracking system was also developed to maintain the control performance during any possible head movements from the user. The results show that more than 10 dB sound attenuation can be obtained for an ultra-broadband frequency range up to 6 kHz in the ears for multiple sound sources and various types of common environmental noise. The use of the PAL makes it possible not to increase the overall sound pressure levels at places other than the error points, while maintaining the same control performance. Future work will include enhanced membrane material design, a more robust head tracking system and the incorporation of reference signal sensors in place of signals taken directly from the primary sources.

CHAPTER 4

ANC with Remote Reference Sensing

4.1 Introduction

When an ANC system is not considering the influence of the reference sensors and signals, commonly, it either takes an ideal reference signal, that is, the primary signal, or places the reference sensors close to the primary source. In these cases, the reference signals are in good agreement with an ideal solution. However, in practice, the primary source can be remote or even inaccessible. The placement of reference sensors is constrained by the given space with signal quality also being affected by the surrounding environment such as reverberations. Current work lacks relevant analyses on the reference sensors and the corresponding signals.

In this chapter, the effects of the reference signals on ANC performance are systematically evaluated. The ANC system has a long secondary path as in ANC headrests. Chapter 4.2 analyses the reference signal quality, particularly reverberant reference signals, on the ANC performance, and the improvement methods. Chapter 4.3 discusses the influence of the reference sensor location on the ANC performance. The associated problems are difficult to solve but can be alleviated by the remote reference sensing method with LDVs, which is presented in Chapter 4.4. Finally, the summary is provided in Chapter 4.5.

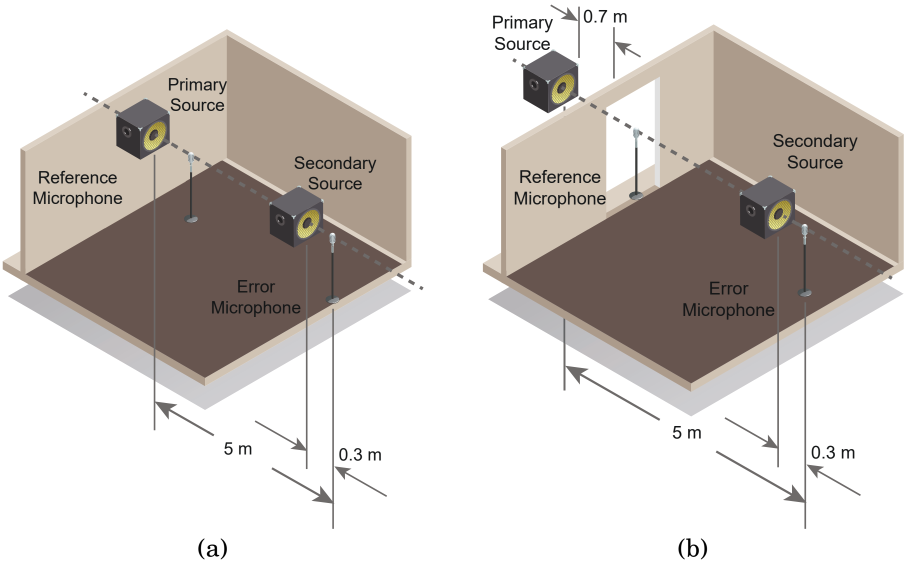

Figure 4.1: System configuration when (a) all the devices are in the hemi-anechoic room and with a lightly padded floor and (b) the primary source is outside the room.

4.2 Signal Quality on the ANC Performance

4.2.1 Reverberant Reference Signal

Two single-channel ANC system configurations are shown in Fig. 4.1. The first configuration is located in an hemi-anechoic room with a lightly padded floor and sound-absorbing walls. The environment is almost anechoic and ideal. The second configuration has its primary sound source outside the hemi-anechoic room and 0.7 m away from the doorway. Its exterior environment can be defined as a strongly reverberating room with sound-hard walls. In both configurations, the error microphone is 0.3 m away from the secondary source and 5 m away from the primary source. The reference microphone is moved to various locations e.g., 0.3 m, 1 m and 3 m away from the primary source.

The first configuration is used as a reference case due to its relatively simple environment. The main purpose of the second configuration is to examine whether the reference signal is away from the primary source and to test whether it is ideal. For a system set up in an enclosed space, the reference signal is affected by the reflections and reverberations as seen later, the ANC performance will be significantly degraded.

Experiments are carried out as described above to observe the ANC performance. The primary and secondary sources are the Genelec 8010A Studio Monitors and the reference and the error microphones are the Antysound Anty M1212 1/2 inch condenser microphones. The controller is the Antysound TigerANC-WIFI-Q active noise controller. The sampling rate is set to be 32 kHz and the filter lengths have 1024 taps. The primary source signal is applied with white noise.

The experimental results for the two configurations and the reference microphone at different locations are shown in Fig. 4.2. Every row represents the different locations of the reference microphone. The “ideal” reference signal is taken directly from the primary source, which is used for evaluation purposes only. From the left column of Fig. 4.2, it can be seen that when the environment is relatively low in reverberations, the ANC performance is generally consistent for different reference microphone locations. It can be observed from the spectra that there is a slight reverberation, which results in a moderate comb-filtering effect, which is, however, not significant enough to cause problems.

On the other hand, as shown in the right column of Fig. 4.2, strong reverberation effects are present. Particularly, as the reference microphone moves further away from the primary source, reverberation effects become increasingly severe. The spectra of the corresponding reference signals are illustrated in Fig. 4.3. When the reference microphone is 3 m away from the primary source (or 2 m away from the error microphone), some frequencies cannot be controlled properly. Fig. 4.3 demonstrates that these uncontrolled frequencies are at troughs of the reference signal, which is a result of the reverberations.

The following section will show the simulation confirmation, which is convenient for further analyses. It will be shown that the issue is not due to the feedback effect but due to insufficient filter lengths. Although a typical solution to deal with reverberations is to increase the filter length, some complications are not desired, e.g., increased demand for controller memory and a slow convergence rate.

4.2.2 Simulation Confirmation

The systems presented in Fig. 4.1 may seem complex in comparison. The problem statement can be further simplified into a single configuration as shown in Fig. 4.4. In this case, all the devices are in the hemi-anechoic chamber,

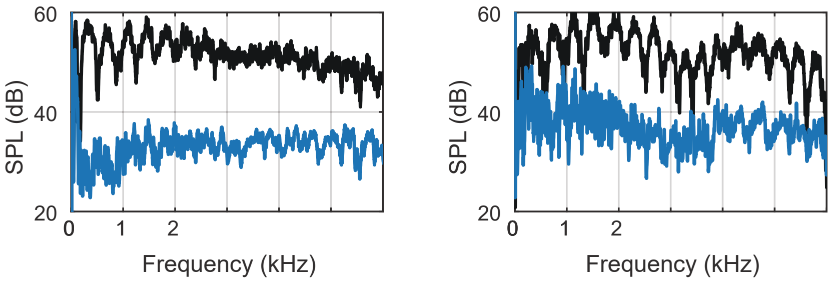

(a) Ideal (b) Ideal

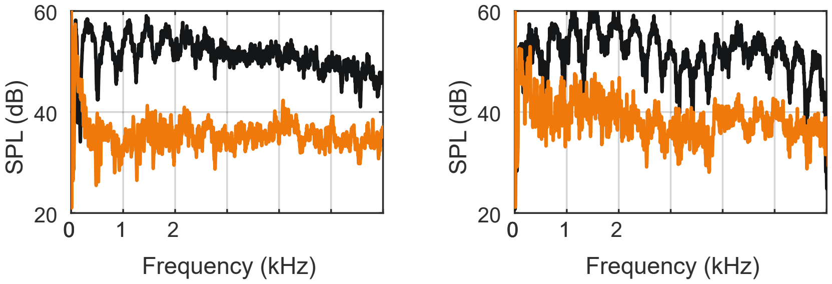

(c) 0.3 m (d) 0.3 m

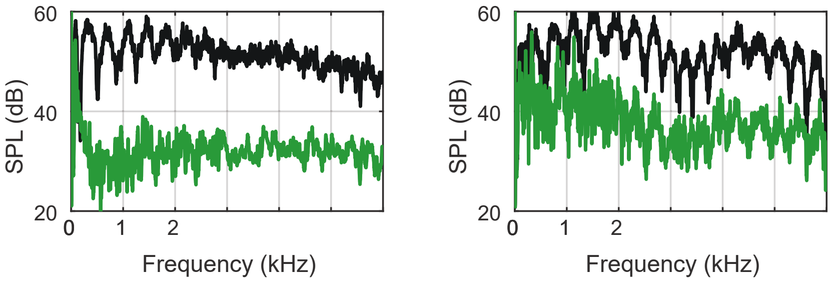

(e) 1 m (f) 1 m

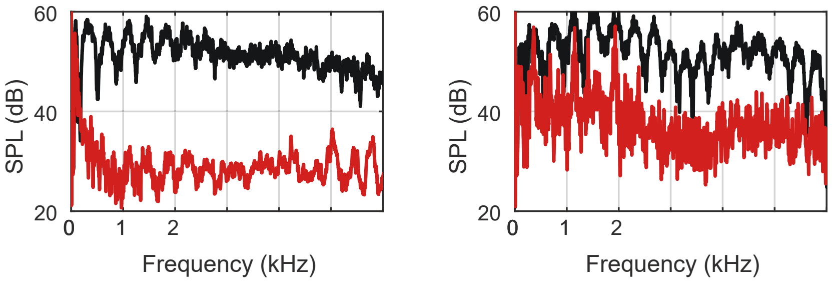

(g) 3 m (h) 3 m

Figure 4.2: The spectra of the *error* signal with ANC off and ANC on when the system is in the hemi-anechoic room (left column) and when the primary source is outside the room (right column). The reference microphone is (a, b) ideal, (c, d) 0.3 m, (e, f) 1 m and (g, h) 3 m away from the primary source.

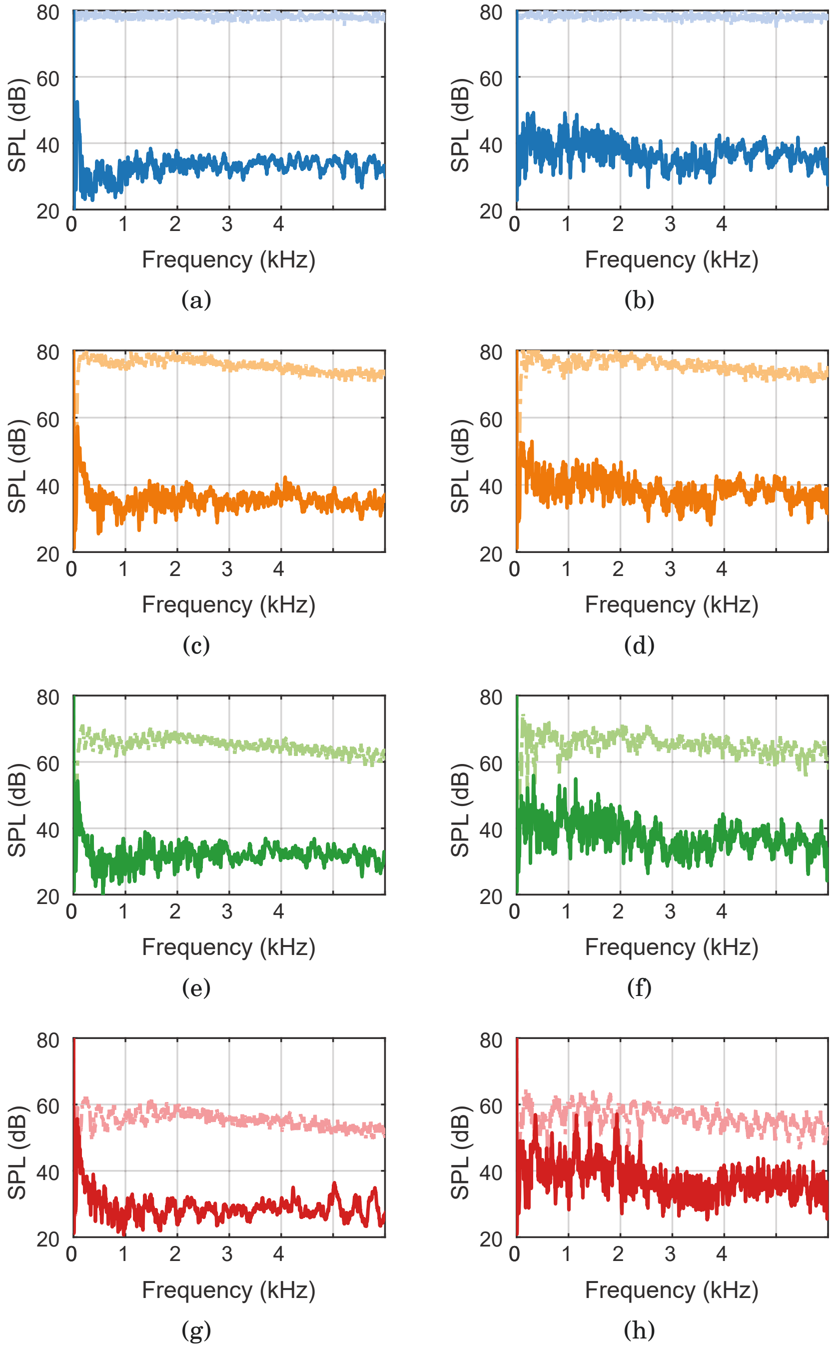

(a) (b) (c) (d) (e) (f) (g) (h)

Figure 4.3: The spectra of the *reference* signal and the *error* signal with ANC off and ANC on when the system is in the hemi-anechoic room (left column) and when the primary source is outside the room (right column). The reference microphone is (a, b) ideal, (c, d) 0.3 m, (e, f) 1 m and (g, h) 3 m away from the primary source.

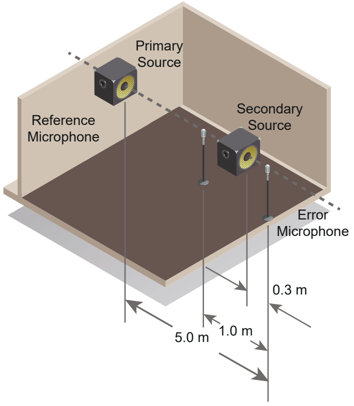

Figure 4.4: System configuration when all the equipment is in the hemi-anechoic room. The floor is either concrete floor or padded with sound-absorbing material to reduce the reflection.

except for one situation with sound absorbing material padded floor and another one with a bare concrete floor. Other configurations of the system remain the same as in the two environments as shown in Fig. 4.1.

The calculated results are shown in Fig. 4.5. By comparing the reference signals (or the error signals with ANC off), one can observe the comb-filtering effect is more significant for hard surfaces. Simulations are carried out to confirm the FxLMS solution with an optimal performance using the Wiener solution (filter lengths 1024 taps). No feedback neutralisation is made in the simulation and both results agree in general with the experimental solution.

Using the measured paths, the simulation result also shows certain uncontrolled frequencies as shown in Fig. 4.5b. One can conclude that it is due to the system itself but other factors. In the subsequent chapter, it will be shown that the filter lengths should be significant for reverberant signals. Optimisations should be made to improve the drawbacks of using long filters.

4.2.3 Improvement Methods

The block diagram of the FxLMS algorithm used in the simulation hereinafter is shown in Fig. 4.6a, with the measured paths shown in Fig. 4.6b. $v(n)$ represents white noise, which passes through the path $R(z)$ to get to the reference signal $x(n)$. $P(z)$ is the primary path, $z^{-\Delta_\mathrm{s}}$ represents the secondary path with $\Delta_\mathrm{s} = 20$ as a pure delay of 20 samples (i.e., 1.2 ms). $\hat{S}(z)$ is the estimated version of $S(z)$. $d(n)$ is the disturbance signal, $y(n)$ is the secondary source

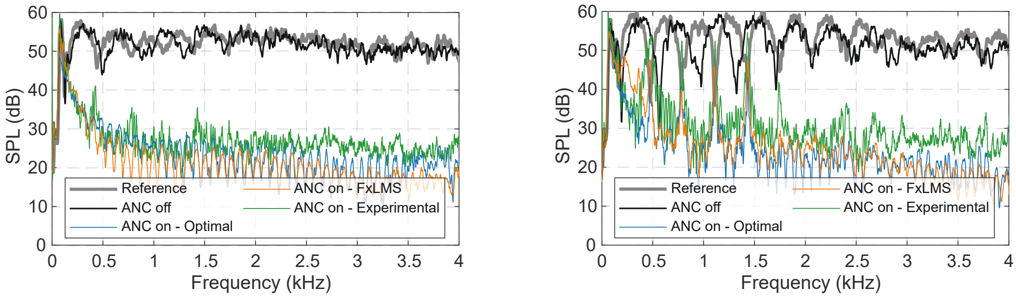

(a) (b)

Figure 4.5: The spectra of the reference signal, the error signal with ANC off, with ANC on using the optimal Wiener solution and the FxLMS algorithm in the simulation, and the error signal with ANC on from the experiment, when (a) in sound absorbing padded hemi-anechoic room, (b) hemi-anechoic room with concrete floor.

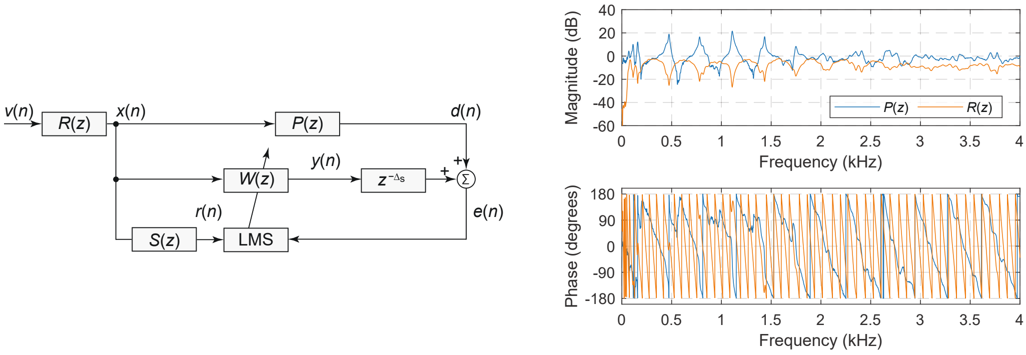

(a) (b)

Figure 4.6: (a) Block diagram of the FxLMS algorithm used in the simulation, the secondary path is a pure delay by Δ_s. (b) Frequency response of $P(z)$ and $R(z)$.

signal, $r(n)$ is the filtered-reference signal and $e(n)$ is the error signal. Other configurations remain the same as described previously.

Improvement via Long Filter Length

Reverberant signals require long filters to be controlled. Although a relatively long filter length of 1024 taps has been applied previously, the length should be further increased. Fig. 4.7 shows the results of the previous case with 1024-tap filters (left column) and the one with 2048-tap filters (right column). The first row shows the MSE and the convergence rate, the second row shows the impulse response of the control filter $W(z)$ and the third row shows the spectra of the signals using the last 20% of the data. By comparing Figs. 4.7e and 4.7f,

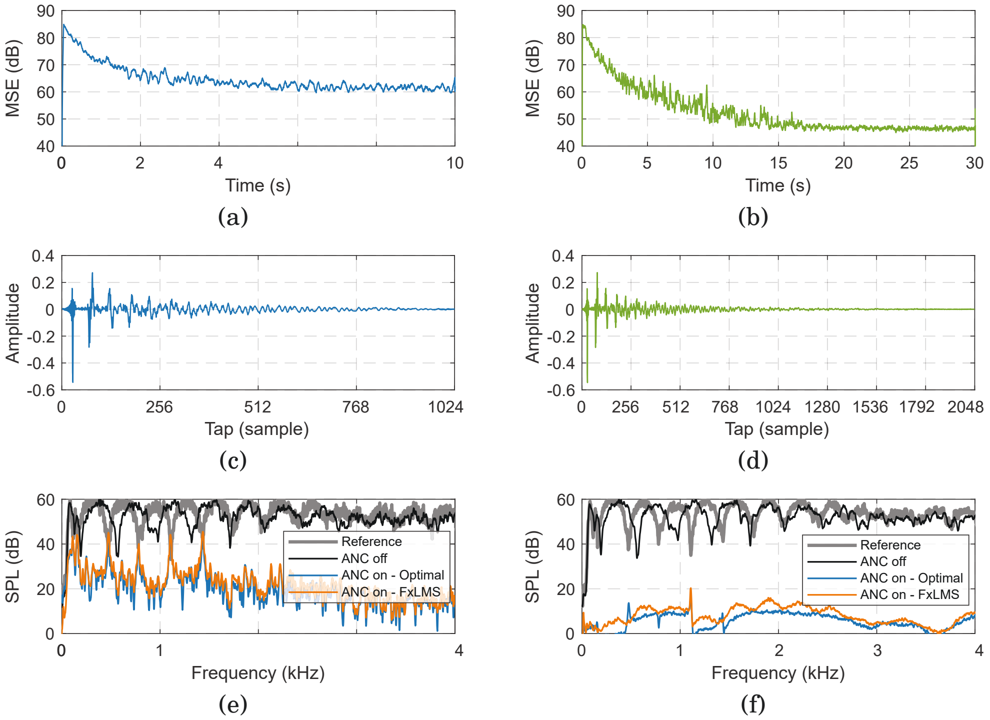

(a) (b) (c) (d) (e) (f)

Figure 4.7: Simulation results using the FxLMS algorithm when with 1024-tap filter lengths (left column) and with 2048-tap filter lengths (right column). (a, b) The MSE in the time domain, (c, d) the impulse response of the control filter $W(z)$ and (e, f) the spectra of the signal from the last 20% of the data.

it is shown that the ANC performance is significantly improved. However, as shown in Fig. 4.7b the system takes around 20 seconds to converge. This rate is too slow for a practical system and it also requires a significant amount of memory even in the form of a single-channel system.

One of the contributing factors to the slow convergence is the long filter lengths, which are fixed at this stage. Another important factor is the flatness of the reference spectrum, which is related to the spread of the eigenvalues (non-flat spectral content) in the correlation matrix of the reference signal. Compared to the minimum value of unity from a random white noise signal, the eigenvalue spread of the correlation matrix of the reference signal in Fig. 4.7f is calculated to be 47830. A large eigenvalue spread results in slow convergence while a small one usually leads to fast convergence. One of the potential methods to overcome this issue is to pre-whiten the reference signal. As shown in Fig. 4.8, the whitening process is accomplished by adding an adaptive decorrelation filter $D(z)$, which mainly consists of a one-step forward prediction filter as illustrated as z^{-1} and $F(z)$. The output of the one-step forward prediction filter $x_f(n)$ is decorrelated to the original reference signal and then used to update the control filter $W(z)$ in the LMS algorithm. The decorrelation filter $D(z)$ is also applied to the error signal such that $x_f(n)$ and $e_f(n)$ are synchronised. $D(z)$ and $F(z)$ have the relationship of

$$\mathbf{d}(n) = [1 \ \ -f(n) \ \ -f(n-1) \ \ldots \ -f(n-L+1)]^{\mathrm{T}} = [1 \ \ -\mathbf{f}^{\mathrm{T}}(n)]^{\mathrm{T}}. \tag{4.1}$$

The filter $f(n)$ which consists of the tap weights of $F(z)$ in the time domain, is calculated using the NLMS algorithm as

$$\mathbf{f}(n+1) = \mathbf{f}(n) + \mu_f \frac{\mathbf{x}(n)}{\mathbf{x}^{\mathrm{T}}(n)\mathbf{x}(n) + \gamma} x_f(n), \tag{4.2}$$

where $\mathbf{x}(n) = [x(n-1)\ x(n-2)\ \ldots\ x(n-L)]^{\mathrm{T}}$ and L is the filter length, μ_f is the step size, γ represents the regularisation factor. The decorrelated reference signal $x_f(n)$ can be found by

$$x_f(n) = x(n) - \mathbf{x}(n-1)^{\mathrm{T}}\mathbf{f}(n). \tag{4.3}$$

The control filter $\mathbf{w}(n)$ for the secondary source is calculated as

$$\mathbf{w}(n+1) = \mathbf{w}(n) - \mu_w \mathbf{r}_f(n) e_f(n), \tag{4.4}$$

where μ_w is the step size for $\mathbf{w}(n)$, $\mathbf{r}_f(n) = \left[r_f(n)\ r_f(n-1)\ \ldots\ r_f(n-L+1)\right]^{\mathrm{T}}$ is the filtered decorrelated reference signal. $e_f(n) = e(n) * \mathbf{d}(n)$, where symbol $*$ denotes signal convolution.

The result of using the decorrelation filter to pre-whiten the reference signal is shown in Fig. 4.9. The control filter still has 2048 taps and the spectra are acquired by the last 20% of the data. In particular, Fig. 4.9 also shows the pre-whitened reference signal. Compared to the original, the spectral content becomes flatter. The eigenvalue spread has a value of 2261, which is significantly reduced from the previous 47830. The advantage is that, as shown in Fig. 4.9a, the system converges within 10 seconds instead of the previous 20 seconds. This is a significant improvement, though the filter lengths still remain to be substantial.

Improvement via Hybrid ANC

Another method of dealing with a reverberant reference signal is to use the hybrid algorithm. Fig. 4.7 (left column) shows frequencies weakly excited in

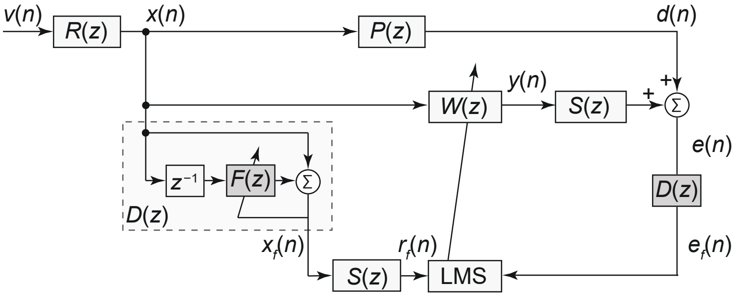

Figure 4.8: Block diagram of the FxLMS algorithm with the adaptive decorrelation filter for pre-whitening.

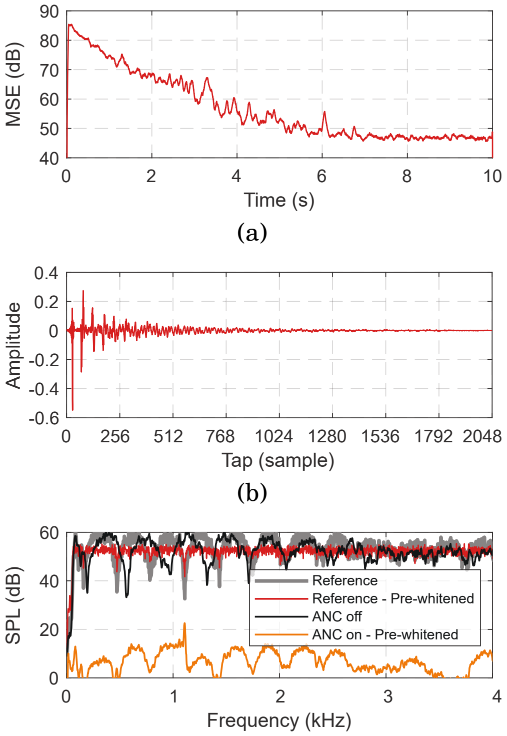

(c)

Figure 4.9: Simulation results using the FxLMS algorithm with the adaptive decorrelation filter with 2048-tap filter lengths. (a) The MSE in the time domain, (b) the impulse response of the control filter $W(z)$ and (c) the spectra of the signal from the last 20% of the data.

the reference signal due to reflections and reverberations, which cannot be properly controlled at the error microphone of insufficient filter lengths.

This problem can be solved by the hybrid ANC algorithm as shown in Fig. 1.7f previously. The hybrid ANC algorithm combines both the feedforward and the feedback architectures. The feedforward subsystem controls the correlated broadband signals, and the feedback subsystem can control the uncorrelated predictable signals, i.e. narrowband signals. In the case shown in Fig. 4.7e, one can take advantage of the hybrid ANC algorithm to reduce the uncontrolled frequencies without using long-tap filters.

The control filter $W_1(z)$ in the feedforward subsystem is found by

$$\mathbf{w}_1(n+1) = \mathbf{w}_1(n) - \mu_1 \mathbf{r}(n) e(n), \tag{4.5}$$

and the control filter $W_2(z)$ in the feedback subsystem is found by

$$\mathbf{w}_2(n+1) = \mathbf{w}_2(n) - \mu_2 \hat{\mathbf{d}}(n) e(n), \tag{4.6}$$

where $\hat{\mathbf{d}}(n)$ is the estimated disturbance signal. At time $n+1$, it can be found by

$$\hat{d}(n+1) = e(n) - \hat{\mathbf{s}}^{\mathrm{T}} \mathbf{y}(n). \tag{4.7}$$

The simulation results are shown in Fig. 4.10. Both control filters have only 512 taps. Compared to the results in Fig. 4.7 (left column), the ANC performance using two 512-tap filters in the hybrid algorithm is superior to the traditional FxLMS algorithm with one 1024-tap filter. The previous uncontrolled frequencies are significantly reduced due to the feedback subsystem.

4.3 Location Constraint of Reference Sensors

Previously, the effect of the reference signal quality on the ANC performance has been thoroughly discussed. In addition, the locations of the reference sensors can also significantly affect the ANC performance. Similarly, some preliminary experimental results are shown first to demonstrate the problem.

4.3.1 Problem Statement

Fig. 4.11a shows the system configuration in the hemi-anechoic room with padded sound-absorbing materials on the ground to reduce reflections. The secondary source and the error microphone have a distance of $L = 0.2$ m and the primary source is $10L = 2$ m away from the error microphone. The distance between the reference and the error microphones l_r will vary resulting in different ANC performances (Fig, 4.11b). As in previous examples, the sampling rate of the controller is 32 kHz and the filter lengths are 1024 taps, which is sufficient for the non-reverberant environment.

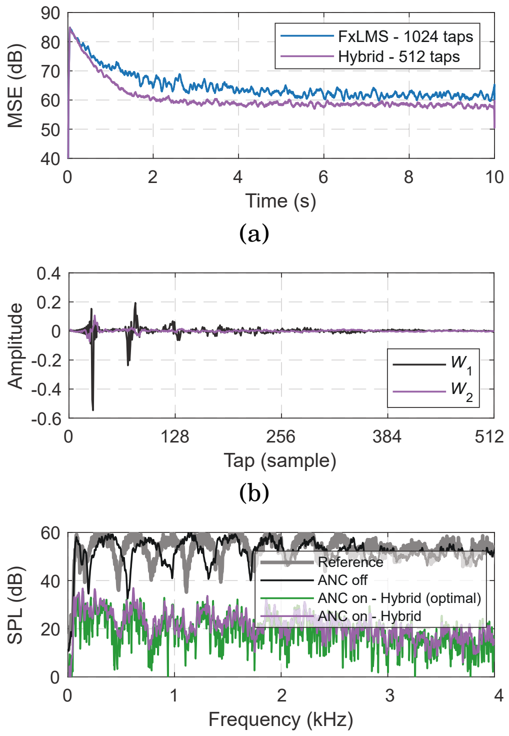

(a)

(b)

(c)

Figure 4.10: Simulation results using the hybrid algorithm with 512-tap filter lengths. (a) The MSE of using the original FxLMS algorithm with 1024 taps and using the hybrid algorithm with 512 taps, (b) the impulse response of the control filters $W_1(z)$ and $W_2(z)$ and (c) the spectra of the signal from the last 20% of the data.

The ideal situation here refers to the case where the reference signal is taken directly from the primary source, which provides the best performance for the given configuration. The reference signal is then taken from the reference microphone, which moves from $l_r = 9L = 1.8$ m to $l_r = 1L = 0.2$ m. It is clear from the results that until $l_r = 5L$, the noise reduction performance remains similar, which is close to the ideal situation. However, as the reference microphone is moved closer to the error microphone, the degradation in the low frequency range becomes more severe than that in the high frequency range[*].

The system environment has been designed to be relatively ideal, that is, the effect of the reflections and reverberations discussed previously have been kept at a minimum, however, the location of the reference microphone

---

[*] The reason for this is provided in the subsequent section about the secondary path being non-minimum-phase.

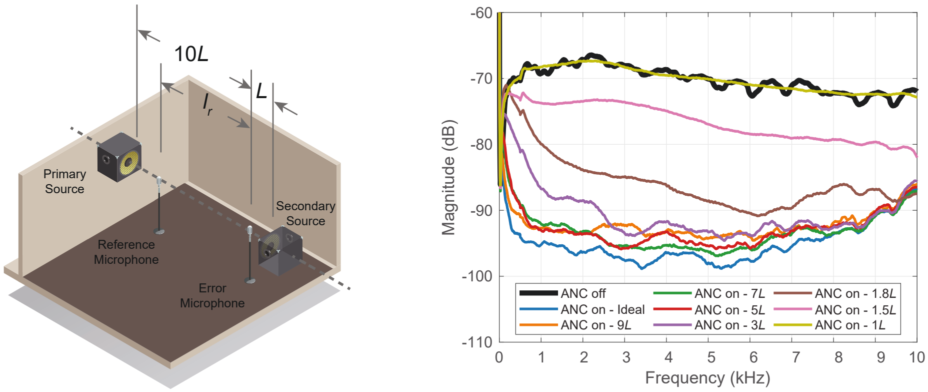

(a) (b)

Figure 4.11: (a) System diagram of examining the ANC performance with different locations of the reference microphone. (b) The spectra of the error signal when ANC is off, when ANC is on with an ideal reference signal taken directly from the primary source, and when ANC is on with the reference microphone at various locations between 1*L* - 9*L*.

is constrained to a certain range to obtain a satisfactory ANC performance. If the reference sensor is close to the error microphone, even though the causality constraint is not violated, the control performance, particularly at low frequencies, can be reduced. This problem is crucial since many ANC applications deal with environmental noises, which have significant energy in the low frequency range. The subsequent section will show the reason is due to the secondary path being non-minimum-phase.

4.3.2 Non-minimum-phase Filters

For brevity purposes, we simplify the ANC paths and signals hereinafter for our analyses. As shown in Fig. 4.12, the reference signal $x(n)$ consists of a Gaussian white noise signal and $v(n)$ is the uncorrelated background noise which is 40 dB lower than $x(n)$. The primary path is a pure delay $z^{-\Delta_\mathrm{p}}$ and the control filter $W(z)$ is calculated from the optimal Wiener solution. To ensure the causality is fulfilled, the delay in the primary path is assumed to be 200 samples hereinafter unless specified otherwise.

First, we consider a minimum-phase secondary path

$$S(z) = \frac{(z-0.95)}{[z-(0.9+0.3\mathrm{j})][z-(0.9-0.3\mathrm{j})]}, \tag{4.8}$$

where there is only one zero which is within the unit circle.

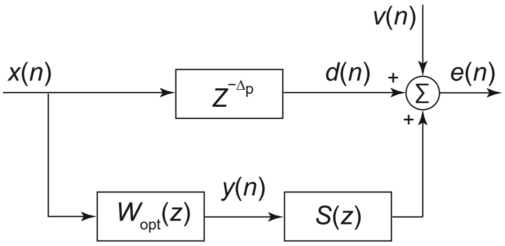

Figure 4.12: Block diagram of a simplified feedforward ANC system, where the primary path is a pure delay $z^{-\Delta_\mathrm{p}}$. The performance is evaluated when the secondary path $S(z)$ is either minimum-phase or non-minimum-phase.

Finding $W(z)$ is equivalent to finding the inverse of $S(z)$. Since $S(z)$ is minimum-phase, its inverse is also minimum-phase requiring no delay theoretically. Fig. 4.13a shows that the noise is fully controlled to the background floor from the Wiener solution. Fig. 4.13b shows the impulse response of $W(z)$, for which the beginning of the impulse is zero until the 200-th tap is reached. It is also important to note that the pulse falls slowly to zero after the spike.

Next, we consider a non-minimum-phase secondary path

$$S(z) = \frac{(z-1.05)}{[z-(0.9+0.3\mathrm{j})][z-(0.9+0.3\mathrm{j})]}, \tag{4.9}$$

where the poles remain the same once the zero is out of the unit circle. Here, the optimal solution is also found using the Wiener solution, as shown in Fig. 4.14a. Although the noise is also fully controlled down to the background noise level, the assumption made is that the primary path has 200-tap delays, that is, the delays between the reference and the error sensors. Fig. 4.14b shows the impulse response of $W(z)$ in this case. Note $W(z)$ is almost the reverse of the previous one. The pulse gradually increases in the front part and then the main spike occurs. If, for example, the delays in the primary path have only 20 samples, the ANC performance is significantly reduced as shown in Fig. 4.15a. The performance in the low frequency range is worse than that in the high frequency range. As shown in Fig. 4.15b, a portion of the original impulse response in Fig. 4.14b essentially becomes anti-causal. This part is also a low-pass filter due to its waveform, thus leading to worse ANC performance, particularly at low frequencies. Fig. 4.16 shows the comparison of the optimal ANC performance with a non-minimum-phase secondary path for various delays in the primary path. The trend is similar to what is found in the experimental results depicted in Fig. 4.11.

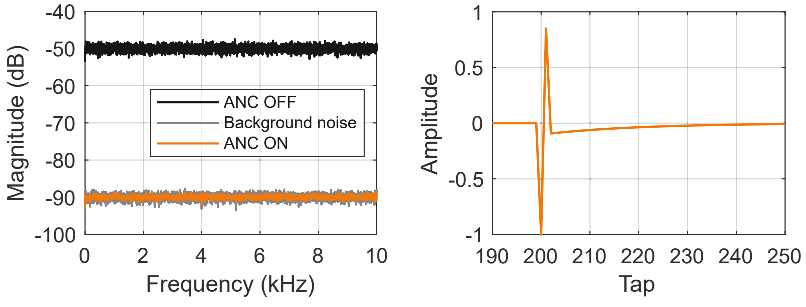

(a) (b)

Figure 4.13: (a) The spectra of the error signal when ANC is off and when ANC is ON and the background noise. The secondary path is minimum-phase and the primary path has 200-tap delays. (b) The impulse response of $W(z)$.

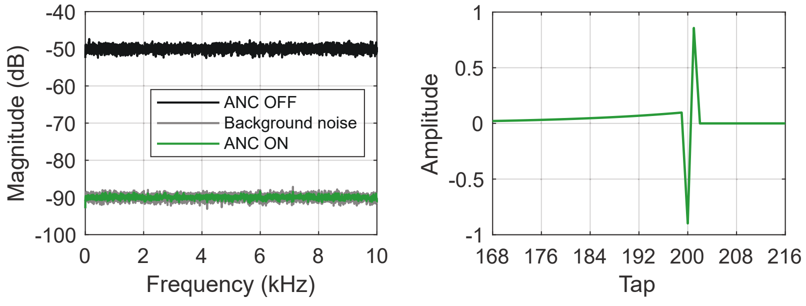

(a) (b)

Figure 4.14: (a) The spectra of the error signal when ANC is off and when ANC is ON and the background noise. The secondary path is non-minimum-phase and the primary path has 200-tap delays. (b) The impulse response of $W(z)$.

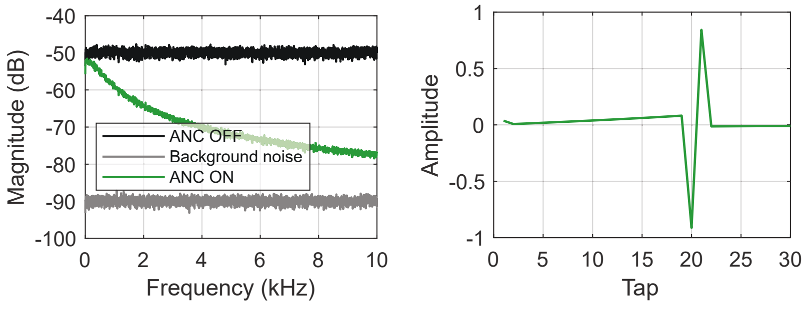

(a) (b)

Figure 4.15: (a) The spectra of the error signal when ANC is off and when ANC is ON and the background noise. The secondary path is non-minimum-phase and the primary path has 20-tap delays. (b) The impulse response of $W(z)$.

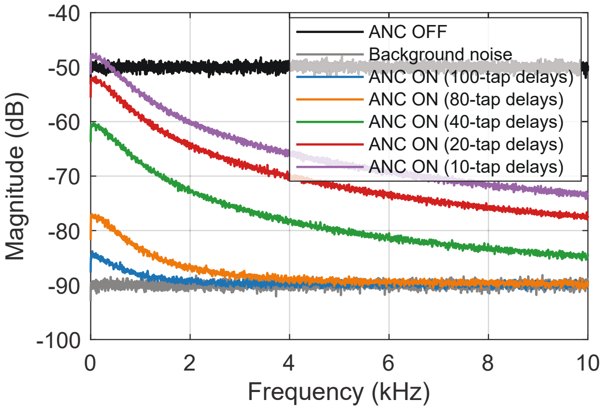

Figure 4.16: The spectra of the error signal when ANC is off, when ANC is on but with different delays in the primary path, and the background noise. The secondary path is non-minimum-phase.

In practice, the secondary path is always non-minimum-phase, which is mainly due to the hardware constraint, e.g., response of the loudspeaker, electrical components, *etc*. In addition, different positions of the zeros outside of the unit circle may have different impacts. Some zeros, even though they are outside of the unit circle, do not degrade the performance significantly, while some do. The analyses of a causality problem are famously known to be difficult. Since ANC systems do not allow any signal shift, once a part of the control filter becomes anti-causal, the information is lost. The typical approach is to re-design the secondary path if possible, which can also be laborious to achieve. If the secondary path is constrained, the positions of the reference sensors must be far away from the error sensors and the secondary sources for a satisfactory ANC performance in the low frequency range.

4.4 Remote Reference Sensing with LDVs

4.4.1 Problem Statement

As demonstrated and discussed in Chapters 4.2 and 4.3, both the quality of the reference signal and the locations of the reference sensors affect the ANC performance. Issues caused by the quality of the reference signal can be solved by algorithms such as pre-whitening with long filters or the hybrid ANC algorithm. The location constraint of reference sensors is more challenging since the problem is directly related to the causality of the system. To have a satisfactory ANC performance, particularly at low frequencies such as below 500 Hz, the distance between the reference sensors and the secondary loudspeakers should be adequate. This problem is more notable in ANC systems with long secondary paths, for instance, in ANC headrest systems.

However, the locations of the reference sensors are practically limited in many applications. The ideal case is to integrate the reference sensors with the headrest or even the whole seat. As analysed previously, the low frequencies can be left uncontrolled. Therefore, the reference sensors must be located away from the main system (i.e., the error points and the secondary sources). As reviewed in Chapter 1, the placement of the reference sensors in personal vehicles has been somewhat explored and the ANC performances for road and engine noise have been validated. The main issues related to the reference sensors and signals in vehicles are about providing enough time advance and having good coherence with error signals. In practice, choosing the best locations for reference sensors can be very complicated.

Once chosen, they are fixed with respect to the main system (the seat and the headrest). There are no concerns regarding the wiring yet. Although can be very long, the cables can be embedded within the seat and the chassis in vehicles. However, the wiring issue can be especially significant in other emerging systems, such as indoor ANC headrests in households or open offices. Fig. 4.17 shows a concept diagram of an indoor ANC headrest system subject to traffic noise from the outside. The noise can also be originated within the enclosed space. Compared to headphones, the distances between the secondary sources and the error signal locations are much greater, e.g., more than 0.2 m. As studied previously, when the secondary path has a distance of 0.2 m, the reference microphone needs to be considerably far (e.g., at least 1 m) away from the error microphone to have a satisfactory performance across the spectrum. If the space is allowed, the reference microphone can be placed close to the window and far away from the headrest to measure the traffic noise. However, it is evident that the seat with the headrest will most likely be non-stationary. The wiring makes it highly undesirable in such a scenario. Similar issues are also present in other spread-out ANC systems when either the reference microphones cannot be located far away from the system or the wiring makes it impractical.

It should be noted that wireless transmission is typically not preferred in ANC systems since the signal delays in wireless communications can be too

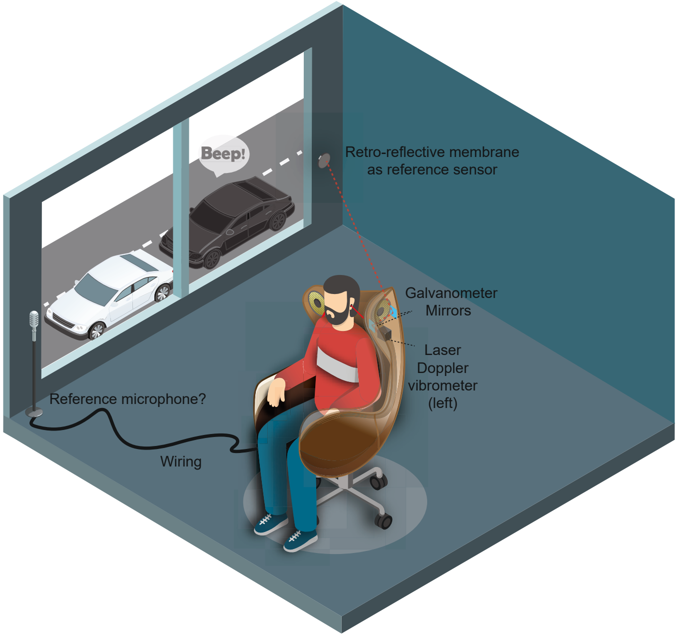

Figure 4.17: Concept diagram of either using the traditional microphone or using the remote reference sensing method with the LDV to measure the reference signal for an indoor ANC headrest system.

great, e.g., in the degree of milli-seconds. As analysed previously, the locations of the reference sensors, which are equivalent to the time advances provided for the control filters, can be crucial to the control performance. If a wireless configuration was used, the causality of the control system could be adversely affected.

To solve this issue, the concept of remote error sensing with LDVs in Chapter 3 can be applied to acquiring the reference signals. As illustrated in Fig. 4.17, instead of using the traditional microphones with long wiring, the LDVs originally used for remote *error* sensing can also be for remote *reference* sensing. Some retro-reflective membranes can be placed across the space and the laser beams from the LDVs can be steered by galvanometer-driven mirrors. The constructions of the membrane and the laser beam steering system have been demonstrated in Chapter 3. The main advantage of the remote reference sensing system, similar to remote error sensing, is that there is no physical connection between the reference points and the error (or the secondary) point. The laser beam from the LDVs can be steered to the retro-reflective membrane at convenient locations, which can be substantially far to provide time advance. Similar benefits have been discussed in Chapter 3. However, some issues, such as the convergence speed, are particularly dependent on the reference signals, which should be particularly addressed. This starts by re-examining the retro-reflective membranes for remote reference sensing purposes.

4.4.2 Membrane Design for Remote Reference Sensing

As understood in Eq. (2.5) and demonstrated in Fig. 2.3, the velocity of a membrane has a scale factor of the angular frequency ω with respect to the incident sound pressure. Therefore, the velocity magnitude of a membrane is comparatively low in the low frequency range (e.g., below 300 Hz). This is particularly problematic for using such a signal for the reference signal, since not only is the coherence degraded, but also the convergence rate for ANC is reduced due to the non-flat spectral content.

Recall that for traditional microphone designs, the resonance of the diaphragm should be out of the frequency range of interest. For a general-purpose microphone, the resonance of the diaphragm is commonly above 10 kHz or 20 kHz (Eargle, 2012), thus leaving the spectral content below the resonance to be flat for sound measurements. However, this may not be the design concept for remote reference sensing with LDVs measuring the velocities of the retro-reflective membranes for ANC purposes. Instead, the resonance of the membranes should be designed to be as low as possible, so that the low velocity magnitude measurement at the low frequencies from the LDVs can be compensated. From Chapter 2.4, it is known that the resonance of the membrane can depend on the following factors,

$$\text{Resonance of the membrane} \propto T \propto \frac{1}{d} \propto \frac{1}{\rho_{\mathrm{M}}}, \tag{4.10}$$

where T is the membrane tension, d is the membrane diameter, ρ_{M} is the membrane density. The resonance frequency decreases as the membrane tension decreases, the membrane diameter increases, or the membrane density increases. In the context of this thesis, the material of the retro-reflective film is not within the topic of discussion. Thus, membrane density ρ_{M} is fixed. The size of the membrane remains to be the only factor to be examined.

Based on the design and development discussed previously, four different sizes of the retro-reflective membranes were constructed as shown in Fig. 4.18. The four membranes - model #1, #2, #3 and #4 - with inner diameters of 5.50 mm, 8.45 mm, 9.65 mm and 12.00 mm, respectively, used the same retro-

Table 4.1: Parameters of the four models of the membrane.

Membrane parameter	Symbol	Unit	Value (Model #1, #2, #3, #4)
Diameter	d	mm	5.50, 8.45, 9.65, 12.00
Tension	T	N/m	24, 21, 20, 23
Damping factor	β	–	200, 50, 35, 30

reflective film as in Chapters 2 and 3. The analytical solution to each model was calculated using the theory studied in Chapter 2.3. The related parameters were modified as shown in Table 4.1 and other parameters remained the same as in Table 2.2. The frequency responses of the membranes were also examined experimentally. Each model had five specimens to confirm the repeatability of the membrane response. Using the setup shown in Fig. 2.8, the frequency responses of the velocity measurement from the LDV for the four membrane models were determined and shown in Fig. 4.19 when subject to the same level of white noise. Each frequency response shows all five specimens where the solid coloured line represents the mean and the shaded area represents the deviation. It is apparent that the frequency responses are consistent with no significant deviation.

The analytical and the experimental solutions in Fig. 4.19 agree well around the first resonance, which is the main focus of this discussion. The resonance frequencies for the four models are 4.75 kHz, 2.85 kHz, 2.50 kHz and 2.15 kHz, respectively. It is apparent that the resonance frequency decreases as the size of the membrane increases. In particular, the velocity magnitude below 1 kHz increases by over 15 dB in general by comparing model #4 to model #1. Such an increment means the increment of signal coherence in the corresponding region. Therefore, the ANC performance can be potentially improved when using such a membrane with the LDV to measure the reference signal remotely.

4.4.3 ANC Performance with Reference Sensing

Similar to the setups from the previous discussions, a single-channel ANC was set up as shown in Fig. 4.20. The secondary loudspeaker (Genelec 8010A) was

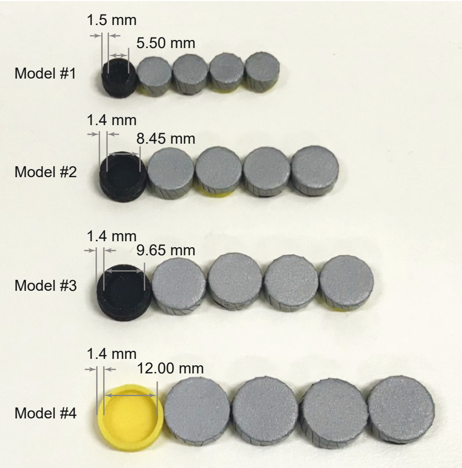

Figure 4.18: Four models of the retro-reflective membranes, with five specimens for each model. Models #1, #2, #3 and #4 have a inner diameter of 5.50 mm, 8.45 mm, 9.65 mm and 12.00 mm, respectively.

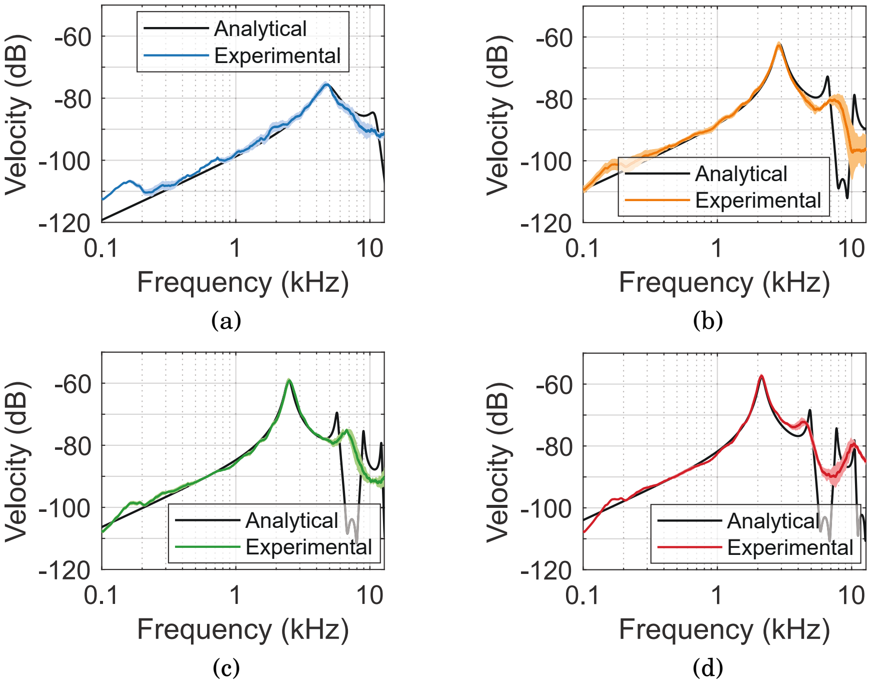

Figure 4.19: The frequency response of the membrane velocity measurement from an LDV with the analytical solution and the experimental measurement when excited by the same level of white noise. The shaded areas show the deviation of the five specimens for the (a) model #1, (b) model #2, (c) model #3 and (d) model #4.

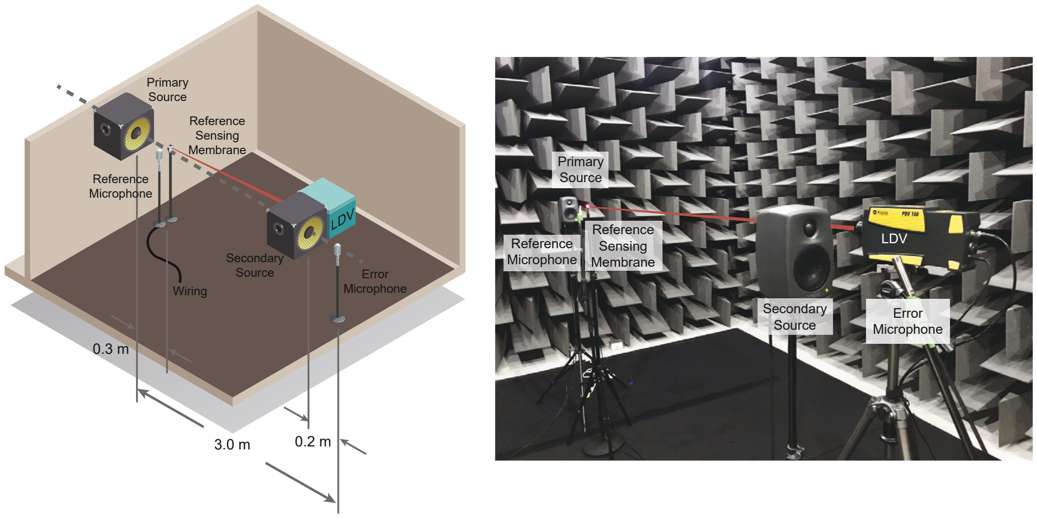

(a) (b)

Figure 4.20: (a) System diagram and (b) experimental setup of the remote reference sensing.

0.2 m away from the error microphone[†] (Antysound Anty M1212). The primary loudspeaker (Genelec 8010A) was 3.0 m away from the error microphone to simulate a noise coming from a distance. As understood in Chapter 4.3, the reference microphone should have a sufficient distance from the error microphone. Thus, a traditional microphone was placed 2.7 m away from the error microphone as the benchmark. The proposed remote reference sensing system was also under test. For comparison purposes, the membrane (each of the four models) was placed close to the microphone. An LDV (Polytec PDV-100) was placed next to the secondary loudspeaker, such that the LDV, the secondary loudspeaker and the error microphone can be treated as an integrated system in, for example, an ANC headrest. The primary signal was a broadband noise with a cut-off frequency of 4 kHz. The ANC controller (Antysound TigerANC WIFI-Q) was set to 32 kHz, and the filter lengths were set to 1024 taps.

First, the coherence function between the remote reference signal from the LDV with each membrane and the disturbance signal from the error microphone should be assessed. It is known that the noise reduction level (NRL) in an ANC system is bounded by the coherence function $\gamma_{xd}^2(\omega)$ between

---

[†] Since the topic of the current discussion is the reference sensors, the error sensor being used in this case is the traditional condenser microphone instead of the previous remote error sensing setup.

the reference signal x and the disturbance signal d,

$$\begin{aligned}\text{NRL (dB)} &= -10\log_{10}\left(1-\frac{|S_{xd}(\omega)|^2}{S_{xx}(\omega)S_{dd}(\omega)}\right)\\ &= -10\log_{10}\left(1-\gamma_{xd}^2\right),\end{aligned} \tag{4.11}$$

where $S_{xx}(\omega)$ and $S_{dd}(\omega)$ are the auto-power spectral density of x and d at frequency ω, respectively. $S_{xd}(\omega)$ is the cross-power spectral density of x and d. For example, a coherence value $\gamma_{xd}^2(\omega) = 0.9$ means 10 dB reduction could be potentially achieved.

Fig. 4.21 shows the coherence function between the reference signal from the LDV and the disturbance signal from the error microphone for each model. The two signals were measured when excited by the same level of white noise. The low magnitude at the low frequencies observed in Fig. 4.19 is also reflected in the coherence functions. The coherence value below 1 kHz for model #1 is the lowest among the four models. For coherence value above 0.99, model #1 has a range of about 1 kHz - 7 kHz. Models #2, #3 and #4 are similar, with model #4 being the best. It has a range of about 200 Hz - 6.2 kHz. However, the coherence value for model #4 is still below 0.85 below 200 Hz due to the low magnitude.

Both the simulation and the experimental solutions using the FxLMS algorithm have been performed for each membrane model. The simulation solution can provide the result closely presenting the practical system. The results are also compared to that using the traditional microphone as the reference as shown in Fig. 4.22. Being a well-developed sound measurement tool, the microphones when used as the reference sensor, provide a good ANC performance of about 20 dB throughout the spectrum (mainly above 100 Hz). The ANC performances with the membranes as the reference sensors are not as ideal as expected, especially in the low frequency region. For example, for model #1 shown in Fig. 4.22a, effective control only occurs above 1 kHz. Particularly, the 20 dB NRL is above 2.5 kHz. Although model #4 is the best, where 20 NRL is above 1 kHz and 5 - 15dB NRL is between 200 Hz - 1 kHz, the performance below 1 kHz is still less than that with the traditional microphone. The reason is partially due to the coherence shown in Fig. 4.21, but more importantly, is due to the low magnitude of the membrane velocity measurement shown in Fig. 4.19. The signals in the low frequency range, e.g., below 1 kHz, are weakly excited compared to the ones at the high frequencies.

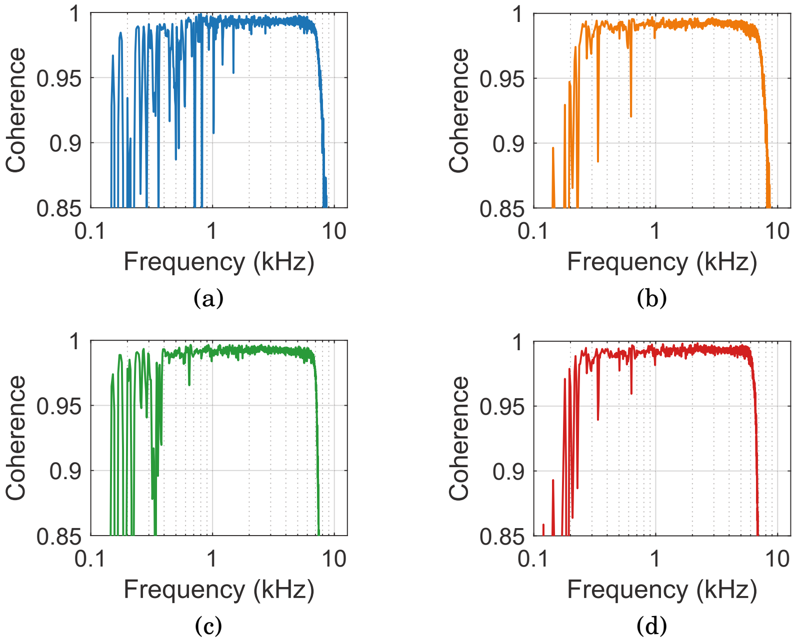

Figure 4.21: The coherence function between the reference signal from the LDV and the disturbance signal from the error microphone for the (a) model #1, (b) model #2, (c) model #3 and (d) model #4.

Therefore, not only is it more difficult to be controlled, but also it takes more time for the control system to adapt to the FxLMS algorithm. As discussed in Chapter 4.2.3, this problem can be alleviated by using the pre-whitening process.

Using the decorrelated FxLMS algorithm to pre-whiten the reference signal, the results have seen both the speedup in the learning curve and the improvement in the spectral content. Fig. 4.23 shows the normalised mean-square-error (NMSE) and Fig. 4.24 shows the spectra of the signals from the last 20% of the data for each membrane model. From Figs. 4.23a and 4.24a, it shows that the decorrelated algorithm provides not only a faster convergence rate but also the control improvement for the low frequency spectral content. Noise at 200 Hz - 1 kHz has seen around 10 dB reduction after the enhancement. Models #2, #3 and #4 have also seen similar improvements, though mainly for the convergence rate. The NRL below 1 kHz, for example for model #4 in Figs. 4.23d and 4.24d, has about 5 - 10 dB improvement in general. Thus, for model #4, there is a 15 - 20dB noise reduction above 200 Hz. This result is comparable to the one with the traditional microphone, with the difference at only 100 - 200 Hz. One of the reasons is the coherence function discussed

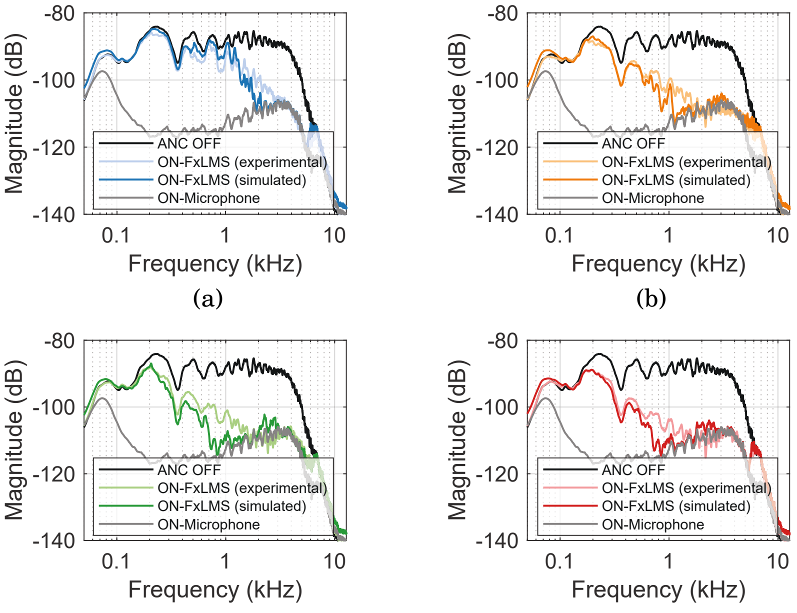

(a) (b) (c) (d)

Figure 4.22: The spectra of the error signal when ANC is off, when ANC is on with the simulated and the experimental FxLMS algorithm with the remote reference sensing for the (a) model #1, (b) model #2, (c) model #3 and (d) model #4, and when ANC is on with the experimental solution with a traditional reference microphone using the FxLMS algorithm as the benchmark.

above, and another one can still be due to causality. The reference signal from the remote reference sensing configuration is more complex than the one from the traditional microphone, thus making the control filter more complex and requiring more time advance between the reference sensor and the secondary source. Nonetheless, the satisfactory control performance at 200 Hz - 4 kHz can cover most types of disturbing noise. The main advantage of such a remote reference sensing configuration is that the reference sensors can be easily placed at a remote location and without the concerns of the wiring issue with the traditional microphones as illustrated in Fig. 4.17.

The retro-reflective membranes used in the remote *reference* sensing systems may not have a serious size restriction as the ones in the remote *error* sensing systems, which may fit into the user's ears. Therefore, a larger size of the membrane can potentially be used compared to model #4. Fig. 4.25 shows the properties and the control performance with a membrane with an inner diameter of 24.00 mm. The frequency response is shown in Fig. 4.25a, which is also averaged from the measurements of five specimens. The first resonance

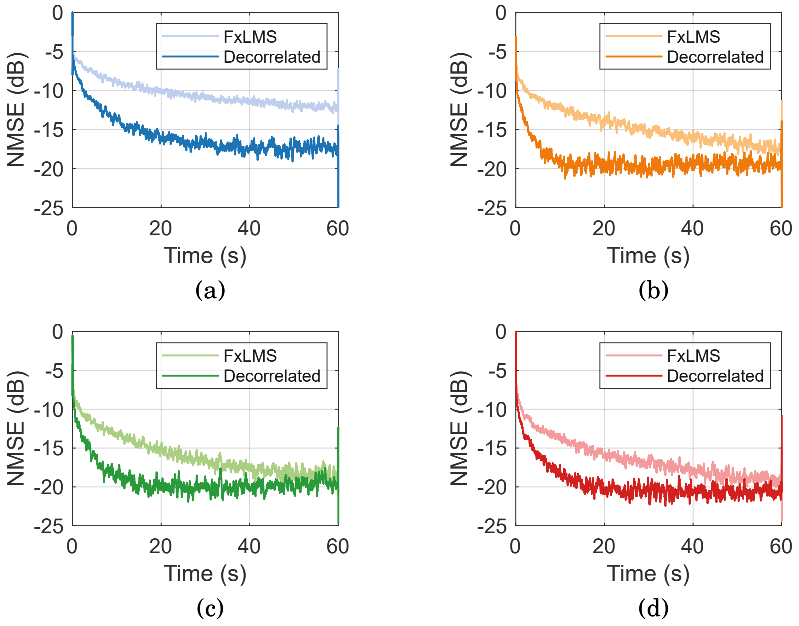

(a) (b) (c) (d)

Figure 4.23: The NMSE of the error signal from the FxLMS algorithm and the decorrelated FxLMS algorithm for the (a) model #1, (b) model #2, (c) model #3 and (d) model #4.

occurs at 1 kHz, and the signal magnitude below 1 kHz has seen a 10 dB increase compared to the one for model #4, though the coherence function shown in Fig. 4.25b is similar. With the FxLMS algorithm, signals at about 500 Hz - 4 kHz can have 20 dB reduction and signals at 200 - 500 Hz can have 5 - 10dB reduction, which is similar to the result from model #4. The use of the decorrelated FxLMS algorithm does not further improve the control performance for the spectral content significantly. The main benefit is the speedup of the convergence rate as shown in Fig. 4.25c. One of the benefits of using such a bigger membrane size is that it makes the system easier to track and scan a bigger target.

4.4.4 Discussions

Although the displacement of the membrane is proportional to the incident sound pressure, and hence flattens the spectral content of the reference signal, the LDV should be equipped with a displacement decoder. It not only increases the size of the LDV system, but also it is not economically efficient. Thus, the hardware approach is not desirable. The velocity measurement may be converted to the displacement signal by applying a filter in the signal process-

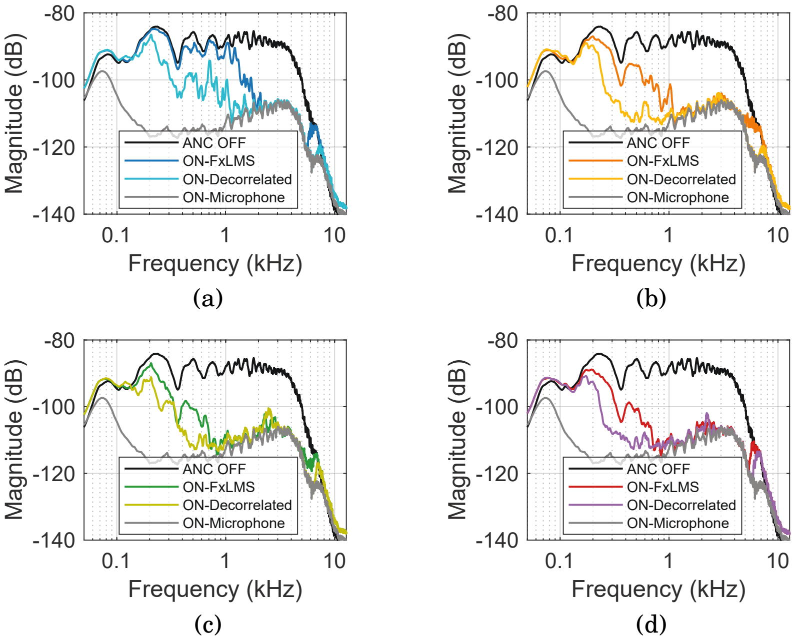

(a) (b) (c) (d)

Figure 4.24: The spectra of the error signal when ANC is off, when ANC is on with the simulated FxLMS and the decorrelated FxLMS algorithms with the remote reference sensing for the (a) model #1, (b) model #2, (c) model #3 and (d) model #4, and when ANC is on with the experimental solution with a traditional reference microphone using the FxLMS algorithm as the benchmark.

ing region in the system when calculating the control filter. This approach is similar to that of the decorrelation filter to pre-whiten the reference signal. Therefore, it is not further discussed. Note that the displacement may only improve the flatness of the spectrum, thus leading to faster convergence. The coherence function, however, may not be improved since the displacement signal is decoded from the original velocity measurement.

One note should be made regarding the distance of the membranes in the proposed remote sensing method. Although it can be potentially placed considerably far away from the main system, the distance should be bounded by the length of the control filter. The distance between the reference sensors and the secondary sources constitutes the delay in the impulse response of the control filter. For example, in previous examples, the filter lengths in the ANC controller were set up 1024 taps, with a sampling rate of 32 kHz. The delay in the control filter should be kept within 512 taps, thus leaving the remaining 512 taps for the main impulses. The maximum 512-tap delay translates to a maximum distance of $512/32000 * 340 = 5.44$ m. If required,

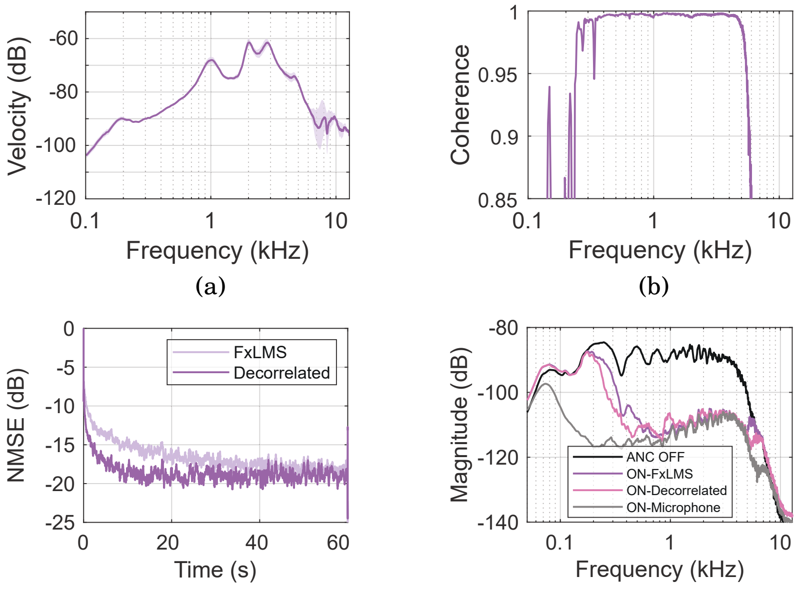

(a) (b) (c) (d)

Figure 4.25: (a) The frequency response of the retro-reflective membrane with an inner diameter of 24.00 mm. The shaded areas show the deviation of the five specimens. (b) The coherence function between the membrane velocity signal from the LDV and the error microphone. (c) The NMSE of the error signal from the FxLMS algorithm and the decorrelated FxLMS algorithm using the membrane. (d) The spectra of the error signal when ANC is off, when ANC is on with the simulated FxLMS and the decorrelated FxLMS algorithms with membrane, and when ANC is on with the experimental solution with a traditional reference microphone using the FxLMS algorithm as the benchmark.

the sampling rate of the system can be reduced to half so as to double the maximum allowed distance. However, the bandwidth of the controlled noise will also be correspondingly degraded.

4.5 Summary

This chapter focuses on the reference sensors and signals in large ANC systems (i.e., the secondary path is significant compared to, for example, ANC headphones). It started by examining some non-ideal reference signals affected by reflections and reverberation, which made it difficult to control the system. Long filters could be used and adaptive decorrelation filters could also be used to speed up the system convergence. Another solution was found to use the hybrid ANC system where the non-coherent signal component could be controlled in the feedback subsystem. Next, the locations of the reference sensors were studied. It was found that, for a given secondary path (i.e., a given secondary loudspeaker and a given error microphone), its property of being non-minimum-phase requires a significant amount of time advance for the controller to have significant control performance across the spectrum. If the reference microphone is relatively too close to the secondary source, a part of the control filter becomes anti-causal, which mainly affects the low frequencies. Unfortunately, issues related to system causality are extremely difficult in any control system. Unless redesigning the secondary path, the reference sensors should be placed at an appropriate distance away from the main system. This may seem impractical in many ANC systems, e.g., a moving ANC system or an ANC system with limited space. To alleviate this issue, a remote reference sensing method with retro-reflective membranes and LDVs was proposed. The proposed method started by suggesting a design concept that is in contrast to the traditional condenser microphone design. The resonance of the membrane should be designed to be as low as possible. It has been shown that, for example with membranes with an inner diameter of 12.00 mm, signals at 200 Hz - 4 kHz can be controlled by 15-20 dB, which is slightly compromised compared to the result from a traditional microphone with 20 dB reduction at 100 Hz - 4 kHz. However, the traditional microphone was placed about 2.7 m away from the error microphone and must be physically connected via cables for the minimal signal delay. Alternatively, the membrane can be placed at a remote convenient location and the sound pressure is measured remotely with an LDV.

CHAPTER 5

Line-based Sound Measurement with Refracto-vibrometry

5.1 Introduction

Many sound field control applications require the acoustic pressure field to be measured in advance. This is commonly achieved by an array of microphones distributed across the field or by altering the position of a smaller number of microphones sequentially. A higher frequency range of interest also requires a higher spatial resolution, which may become impractical for certain applications. Sometimes, the control performance is degraded due to difficulties in installing microphones at certain locations. Furthermore, the presence of physical transducers might perturb the sound field itself. For these reasons, non-intrusive, large-scale, high spatial resolution sound field measurement techniques are worthy of investigation.

Refracto-vibrometry, based on the acousto-optic effect, can be used to reconstruct a sound field without obstructing the field (see Chapter 1 for the review of the technique). Sound waves are compressional oscillatory disturbances that propagate in air as fluid medium. The pressure and the density of air are modulated with the resulting refractive index altering the amplitude and phase of light. These changes can be readily detected using LDV. When the reflecting surface is stationary, the highly sensitive measurement from the LDV *only* results from the variations in the optical path due to the fluctuating sound field, so refracto-vibrometry can be used as an alternative to reconstructing a sound field.

The work herein focuses on using refracto-vibrometry to reconstruct the sound field at the opening of an enclosure, which might represent an aperture such as an open window. In such locations, the sound field can be complicated and thus require a large number of microphones for either sound measurement or control. It is also necessary that obstructions are minimised for such an opening (Qiu, 2019; Wang et al., 2019b). This chapter explores using refracto-vibrometry and the quality of the reconstructed sound field will be examined in what follows and compared with that from a microphone array. Chapter 5.2 describes the fundamentals of refracto-vibrometry. Chapter 5.3 provides several sound field reconstruction methods. Chapter 5.4 offers the details of an experimental investigation and finally Chapter 5.6 summarises this chapter.

5.2 Refracto-vibrometry Fundamentals

5.2.1 Measurement Principle

The pressure fluctuation of a sound field changes the refractive index of the medium. In air, the refractive index, n, is proportional to the sound pressure, p, with the following relationship (Torras-Rosell et al., 2012),

$$n(t) = (n_0 - 1)\left(1 + \frac{p(t)}{p_0}\right)^{\frac{1}{\gamma}} + 1 \approx n_0 + \frac{n_0 - 1}{\gamma p_0} p(t), \tag{5.1}$$

where n_0 is the refractive index of air under standard atmospheric pressure, p_0 is the static atmospheric pressure, γ is the specific heat capacity ratio of air.

The phase, ϕ, of light travelling through the sound field has the following relationship with the refractive index, n

$$\phi(t) = k_0 \int_L n(t)\, dl, \tag{5.2}$$

where k_0 is the wavenumber of light *in vacuo* and L is the travelling path of the light. Combining Eq. (5.1) into (5.2), ϕ can be re-written as

$$\phi(t) = k_0 n_0 L + k_0 \frac{n_0 - 1}{\gamma p_0} \int_L p(l,t)\, dl = \phi_0 + \phi_p(t), \tag{5.3}$$

where ϕ_0 is the static phase and ϕ_p is the dynamic phase due to the sound wave. Any variation of the pressure along the path alters the measured scattering light. An LDV velocity measurement, v, is proportional to the time derivative of the phase of the light,

$$v(t) = \frac{1}{k_0 n_0} \frac{d\phi(t)}{dt}. \tag{5.4}$$

When an LDV is used for measurement from a vibrating object, the vibration of the surface is typically much more significant than any path length variations due to surrounding sound field pressure fluctuations, i.e., $\phi_0 \gg \phi_p$. However, when the object is stationary and not susceptible to vibration, the velocity measurement from the LDV is totally contributed to by the dynamic phase, that is, the pressure fluctuation along the travelling path of the light. Therefore, Eq. (5.4) becomes

$$v(t) = \frac{1}{k_0 n_0} \frac{d\phi_p(t)}{dt} = \frac{n_0 - 1}{\gamma p_0 n_0} \int_L \frac{dp(l,t)}{dt} dl. \tag{5.5}$$

which, in the frequency domain, is written as

$$V(\omega) = \mathrm{i}\omega \frac{n_0 - 1}{\gamma p_0 n_0} \int_L P(l,\omega) dl, \tag{5.6}$$

with ω being the angular frequency of interest.

5.2.2 Radon Transform

Equation (5.6) shows that the velocity measurements from the LDV due to the sound field are the line integrals of the optical paths rather than discrete point measurements. Such measurements are the projections “slicing” through the sound field and are described as the *Radon transform* (Kak & Slaney, 2001) as illustrated in Fig. 5.1. At a projection angle θ, the Radon transform R can be mathematically expressed through

$$R(x',\theta,\omega) = \int_{-L/2}^{L/2} P(x',y',\omega) dy', \tag{5.7}$$

where

$$\begin{bmatrix} x' \\ y' \end{bmatrix} = \begin{bmatrix} \cos\theta & \sin\theta \\ -\sin\theta & \cos\theta \end{bmatrix} \begin{bmatrix} x \\ y \end{bmatrix}, \tag{5.8}$$

are the new coordinates. Eq. (5.6) can be represented by the Radon transform as

$$V(x',\theta,\omega) = \mathrm{i}\omega \frac{n_0 - 1}{\gamma p_0 n_0} R(x',\theta,\omega), \tag{5.9}$$

where the velocity measurements from the LDV are the scaled Radon transform of the sound field.

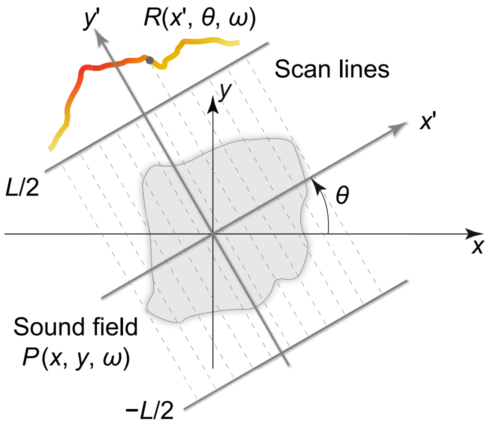

Figure 5.1: Demonstration of the Radon transform and parallel scan lines.

5.3 Sound Field Reconstruction Methods

Since the velocity measurements from the LDV are forward projections of the sound field, and are also equivalent to the Radon transform of the sound field, sound information at points within the sound field can be recovered by solving its inverse (i.e., inverse Radon transform). There are various analytical and numerical methods to achieve this.

5.3.1 Analytical Method - Filtered Back-Projection (FBP)

The FBP is the most popular and basic method of finding the inverse Radon transform. Since the measurements are the forward projections, the original sound field can be theoretically back-projected (Barrett, 1984; Kak & Slaney, 2001). The FBP method can be written as

$$P(x,y,\omega) = \frac{1}{\mathrm{i}\omega}\frac{\gamma p_0 n_0}{n_0 - 1}\int_0^{2\pi} R(x',\theta,\omega)H(\omega)\,d\theta, \tag{5.10}$$

where

$$H(\omega) = \begin{cases} |\omega| & \text{for } |\omega| \leqslant \omega_{\max}, \\ 0 & \text{else }, \end{cases} \tag{5.11}$$

is typically a ramp (highpass) filter to prevent oversampling at certain locations. This method essentially integrates (sums) all the projections with an adjusting filter. The FBP is an analytical method to find the inverse Radon transform of the sound field to recover the original sound field information.

5.3.2 Numerical Methods - TSVD & Tikhonov

Alternatively, the Radon transform can be represented numerical as (Bertero & Boccacci, 2020; Fernandez-Grande et al., 2013; Torras-Rosell et al., 2013)

$$\mathbf{v} = \mathbf{A}\mathbf{p}, \tag{5.12}$$

where $\mathbf{v} \in \mathbb{C}^{JN}$ is the vector of all the velocity measurements, $\mathbf{A} \in \mathbb{C}^{JN \times MM}$ is the matrix representing the (discrete) Radon transform, and $\mathbf{p} \in \mathbb{C}^{MM}$ is the vector of the sound pressure of all the points in the sound field. It is assumed that there are N light beams per projection angle and that there are J angles. There are $M \times M$ points to be determined in the sound field. Once the system is identified, that is, $\mathbf{A}$ is modelled, the sound pressure of all the points within the sound field can be found. Finding the inverse Radon transform is equivalent to solving the inverse problem. However, as will be demonstrated later, this inverse problem is ill-posed and certain regularisation should be made. There are two main regularisation methods that can be used - Truncated Singular Value Decomposition (TSVD) and the Tikhonov regularisation (Bertero & Boccacci, 2020; Hansen et al., 2021).

Truncated Singular Value Decomposition (TSVD)

When $\mathbf{A}$ is written in the form of SVD, i.e.,

$$\mathbf{A} = \mathbf{U}\Sigma\mathbf{V}^{\mathrm{H}}, \tag{5.13}$$

where $\mathbf{U} \in \mathbb{C}^{JN \times JN}$ and $\mathbf{V} \in \mathbb{C}^{MM \times MM}$ are orthogonal matrices. $\Sigma \in \mathbb{C}^{JN \times MM} = \operatorname{diag}(\sigma_1, \sigma_2, \ldots, \sigma_r)$ is a diagonal matrix with the singular values of $\mathbf{A}$. The solution can be found by (Hansen, 1990)

$$\mathbf{p} = \mathbf{A}^{\dagger}\mathbf{v} = \mathbf{V}\Sigma^{\dagger}\mathbf{U}^{\mathrm{H}}\mathbf{v}, \tag{5.14}$$

where

$$\Sigma^{\dagger} \in \mathbb{R}^{MM \times JN} = \begin{bmatrix} 1/\sigma_1 & 0 & \cdots & 0 & \cdots & 0 \\ 0 & 1/\sigma_2 & & & & \vdots \\ \vdots & & \ddots & & & \\ & & & 1/\sigma_{r_\alpha} & & \\ \vdots & & & & \ddots & \vdots \\ 0 & \cdots & & & \cdots & 0 \end{bmatrix}, \; (r_\alpha < r). \tag{5.15}$$

The † symbol denotes pseudoinverse. Certain small singular values are truncated to prevent unstable inverse results.

Tikhonov Regularisation

The Tikhonov regularised solution (Tikhonov & Arsenin, 1977) of Eq. (5.12) can be found through

$$\mathbf{p} = \operatorname{argmin}\left\{\|\mathbf{A}\mathbf{p}-\mathbf{v}\|_2^2 + \lambda^2\|\mathbf{p}\|_2^2\right\}, \tag{5.16}$$

where λ is the regularisation parameter. The solution to the Tikhonov regularised optimisation problem is

$$\mathbf{p} = (\mathbf{A}^{\mathrm{H}}\mathbf{A} + \lambda^2\mathbf{I})^{-1}\mathbf{A}^{\mathrm{H}}\mathbf{v}, \tag{5.17}$$

where superscript $^{\mathrm{H}}$ denotes Hermitian transpose, $\mathbf{I}$ is the identity matrix.

5.4 Experimental Investigation

5.4.1 System Setup

The sound field under investigation was at an opening of an enclosure as shown in Fig. 5.2a. The specific tonal frequency under investigation herein is 500 Hz. The opening was at the topside. The enclosure had dimensions of $(L_x \times L_y \times L_z) = (1 \times 0.85 \times 0.9)$ m and was made from acrylic material with 10 mm thickness. A sound source (a Genelec 8010A studio monitor) was placed at the coordinate $(-0.4, -0.325, 0.1)$ m. The sound field to be measured was located at the $z = 0.95$ m plane. Fig. 5.2b shows the traditional sound field measurement using a 14×16 microphone array (Brüel & Kjær Type 4957) with $L_{\mathrm{mic}} = 60$ mm spacing. Fig. 5.2c shows the setup of using the refracto-vibrometry with an LDV to reconstruct the sound field. The LDV (Polytec PDV-100) was mounted on a 1.5 m motorised ball-screw slider actuated by a stepper motor (NEMA23). The reflector was a steel beam located $L = 1.5$ m away across the field with retro-reflective tape adhered for the maximum laser beam reflection. Accelerometers (Brüel & Kjær Type 4533-B) were adhered to the reflector at six spots close to the laser reflection spots to monitor the vibration of the reflector. There were 131 scan lines per projection angle with an interval of 10 mm and 36 projection angles, i.e., $\theta \in [0:10:350]$. All signals

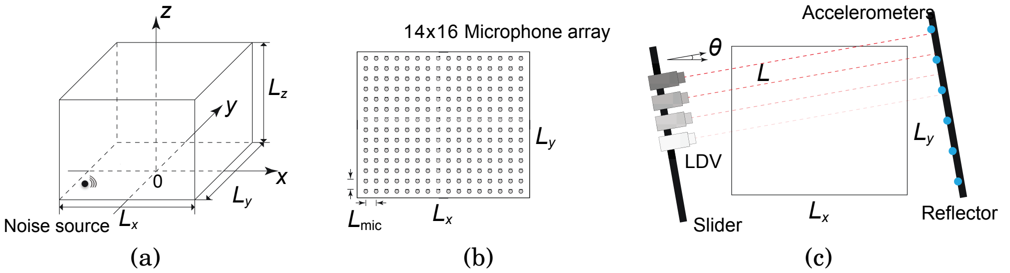

Figure 5.2: (a) The coordinate and s of the enclosure under investigation. The opening is at the topside. (b) Configuration of the 14×16 microphone array to measure the sound field at $z = 0.95$ m. (c) Sound field measurement/reconstruction by refracto-vibrometry using an LDV on a motorised slider. The optical path has a length of L, and the projection angle is θ.

were acquired and recorded through the Brüel & Kjær LAN-XI DAQ modules (Type 3053 and 3160). The atmospheric condition was measured through a thermo-hygro-barometer (RS-1160). The heat ratio of air was $\gamma = 1.4$, the static pressure was $p_0 = 101.32$ kPa, the room temperature was 25.0 °C and the relative humidity was measured to be 47.6%. The static refractive index of air n_0 was hence calculated (Malkin et al., 2014) to be 1.0002667951. Fig. 3.14 shows the experimental setup.

5.4.2 Data Collection and Noise Management

The procedure for velocity measurements is illustrated in Fig. 5.4. At projection angle θ, the motorised slider takes the LDV to scan the sound field. When the LDV is moved to the position, the motor pauses for 5 seconds to allow the measurement to be made. The 5-second periods are subsequently found by locating the peaks of the recorded signal, these being due to the movement of the slider and therefore the LDV. Then, the last 3 of every 5 seconds are taken for each location. Since the frequency of interest is known, a narrow bandpass filter for 500 Hz is applied. Due to the delay in the filter (non-minimum-phase), the last 2.9 second data is kept. Next, using the recorded loudspeaker signal as the phase reference, the trimmed velocity signals can be synchronised. After applying further filtering (such as using the MATLAB function filloutliers) to reject any remaining spurious noise and outliers in the signals, finally, the velocity in the frequency domain, $V(x', \theta, \omega)$, can be found.

So far, some fundamental noise filtering techniques for the raw data have

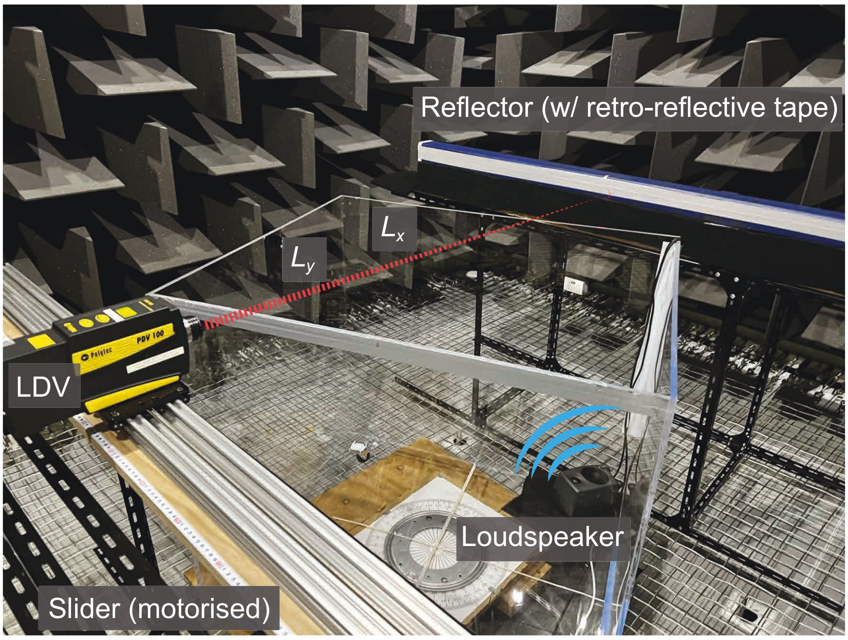

Figure 5.3: Experimental setup of refracto-vibrometry to measure a sound field of an enclosure opening.

been applied. Further actions can be taken to alleviate effects of measurement noise. Figs. 5.5a and 5.4b show the real and imaginary of velocity, respectively, for 131 spots per projection angle and for the total 36 projection angles (the scattered plot). To avoid any irregular velocity measurement at certain locations, curve fitting is applied to the measurements. The red lines in Figs. 5.5a and 5.4b are the results from the robust locally weighted scatter plot smoothing (RLOWESS) method with a window of 12 samples (MATLAB built-in function rlowess). Certain outliers, in particular as can be observed in, for example, $\theta = 90°, 100°, 280°$, are rejected during this processing.

After the basic and intermediate filtering and smoothing processes to manage the noisy data, interpolation can then be used to expand the amount of usable data. The number of scan lines per projection angle is already dense with 131 lines with 10 mm interval, which is sufficiently small compared to the acoustical wavelength at 500 Hz, i.e., 0.686 m. However, there are only 36 projection angles with a 10° interval, which can be further improved. Instead of physically taking measurements at finer angles, e.g., 72 projection angles with a 5° interval, more values can be interpolated from the existing ones. Fig. 5.5 shows the interpolated velocity measurements using the spline method. It is clear that a finer resolution, that is, more available data, is acquired and is therefore available for reconstructing the sound field.

5.4.3 Valid Frequency Range

By comparing the measurements from both the LDV and the accelerometers, which are shown in Fig. 5.6, it is validated that the velocity measurements from the LDV are caused by the acousto-optic effect. From the six locations on the reflector, it is clear that the acousto-optic effect is prominent generally above 500 Hz. Below 500 Hz, the reflector can be more easily acoustically excited and this setup is thus not suitable for refracto-vibrometry technique at lower frequencies.

5.4.4 Regularisation Parameters

Fig. 5.7 shows singular values of **A** corresponding to the 90 × 90 resolution and 72 uniformly distributed projection angles. The singular values span from about 4.7×10^{-4} at the maximum to 4.6×10^{-21} at the minimum. This significant span of singular values shows that the matrix **A** is very ill-conditioned. Regularisation must be made to ensure the validity of the inverse results.

The appropriate regularisation parameters, i.e., r_α in Eqs. (5.14) and (5.15) and λ in Eq. (5.17), can be found through the generalised cross validation (GCV) method (Hansen, 1998). λ for the Tikhonov regularisation will minimise the GCV function of

$$G(\lambda) = \frac{||\mathbf{A}\mathbf{p}_\lambda - \mathbf{v}||_2^2}{\left(\mathbf{I} - \mathrm{trace}\left(\mathbf{A}(\mathbf{A}^{\mathrm{H}}\mathbf{A} + \lambda^2\mathbf{I})^{-1}\mathbf{A}^{\mathrm{H}}\right)\right)^2}. \tag{5.18}$$

Similarly, r_α for the TSVD will also minimise the GCV function in the form of

$$G(r_\alpha) = \frac{||\mathbf{A}\mathbf{p}_{r_\alpha} - \mathbf{v}||_2^2}{(JN - r_\alpha)^2}. \tag{5.19}$$

As shown in Fig. 5.8, λ and r_α are found to be 1.195×10^{-4} and 87 (Hansen, 1994), respectively, for minimising the GCV functions. These values are then used to find the inverse results.

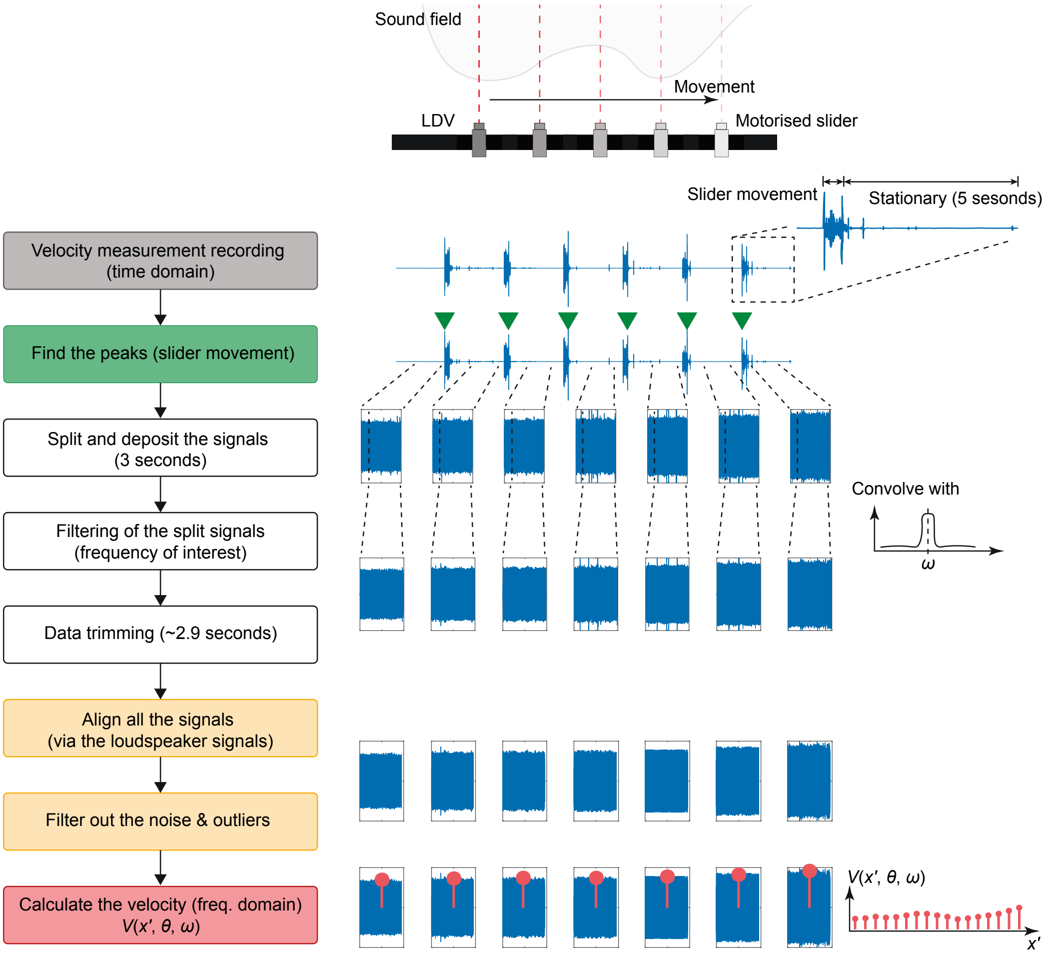

Figure 5.4: Data collection procedure for sound field reconstruction using refracto-vibrometry.

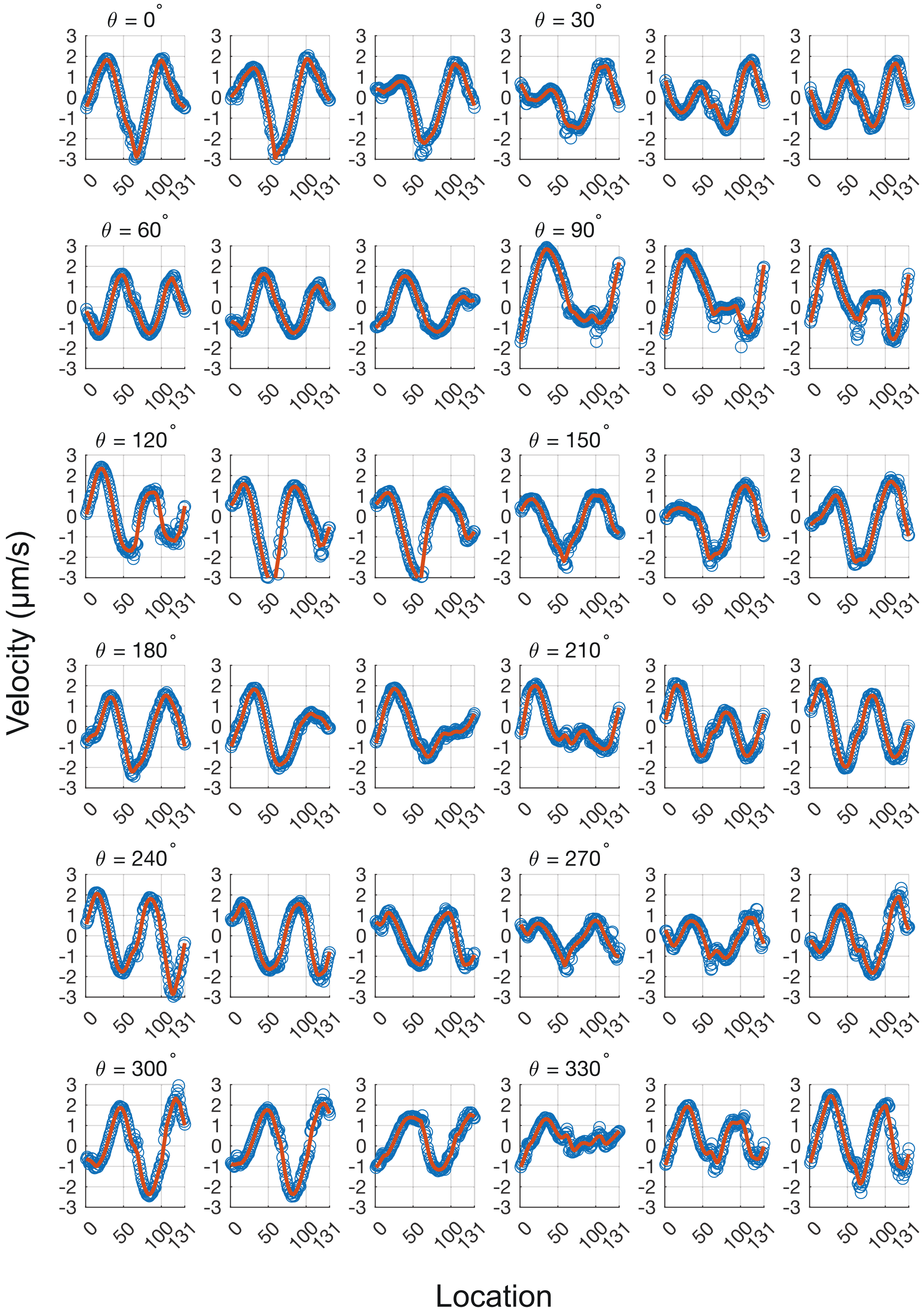
θ = 0°
θ = 30°
θ = 60°
θ = 90°
θ = 120°
θ = 150°
θ = 180°
θ = 210°
θ = 240°
θ = 270°
θ = 300°
θ = 330°
Velocity (µm/s)
Location
3
2
1
0
-1
-2
-3
0
50
100
131

(a)

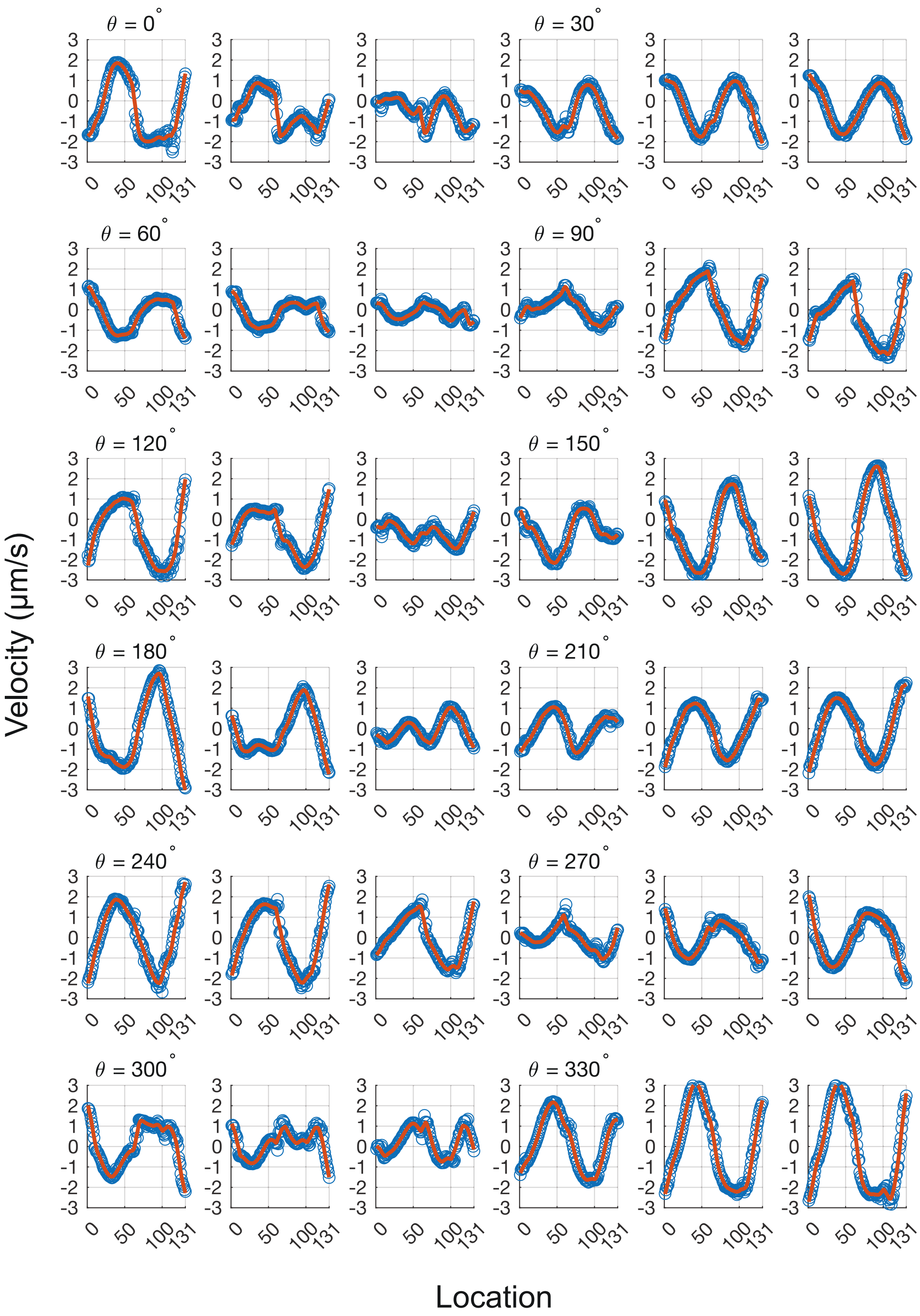

(b)

Figure 5.4: (a) *Real* part of velocity measurements, $\mathfrak{Re}\big(V(x',\theta,\omega)\big)$, and (b) *imaginary* part of velocity measurements, $\mathfrak{Im}\big(V(x',\theta,\omega)\big)$, at 131 spots for projection angles $\theta \in [0:10:350]$. The scattered dots are the velocity value at the discrete locations. The line represents the smoothed data filtering out the any irregular value.

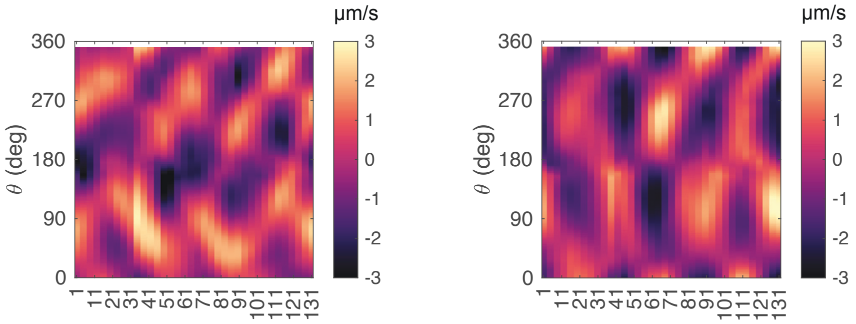

(a) 36 angles, real part (b) 36 angles, imaginary part

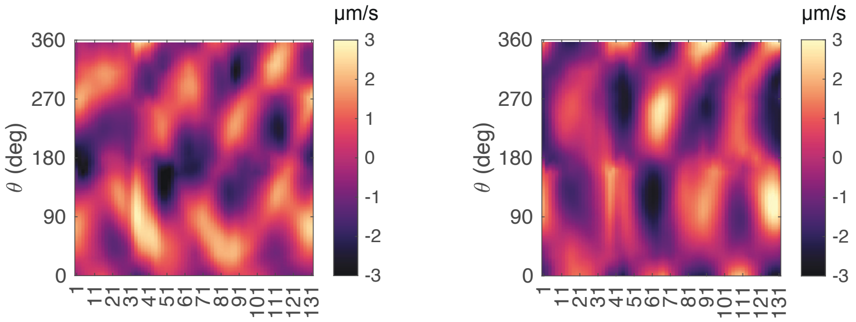

(c) 72 angles, real part (d) 72 angles, imaginary part

Figure 5.5: (a) Real part and (b) imaginary part of velocity measurements with 36 projection angles. (c) Real part and (d) imaginary part of velocity measurements with 72 interpolated projections angles.

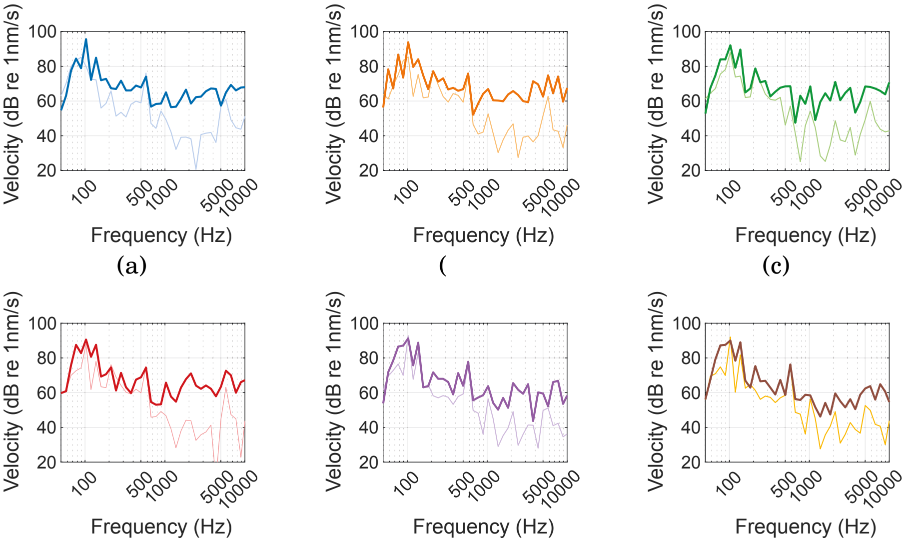

(a) ((c)

(d) (e) (f)

Figure 5.6: Velocity from the LDV (thick lines) across the sound field and from the accelerometers (thin lines) adhered to the rigid reflector at six locations.

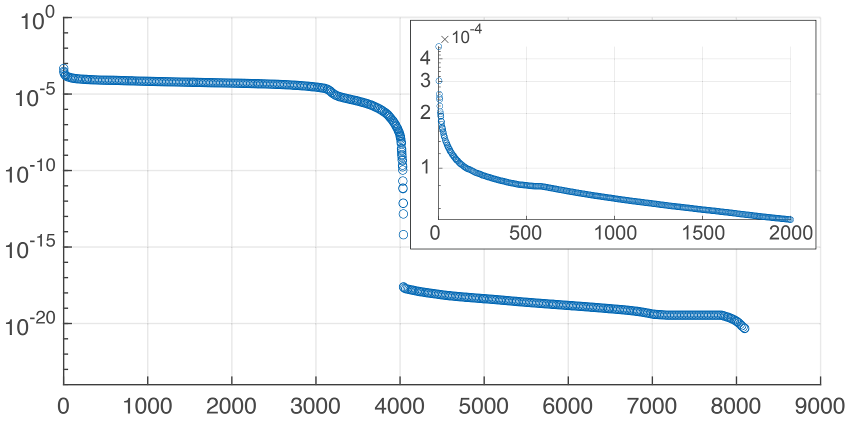

Figure 5.7: Singular values of **A** corresponding to the 90 × 90 resolution and 72 uniformly distributed projection angles.

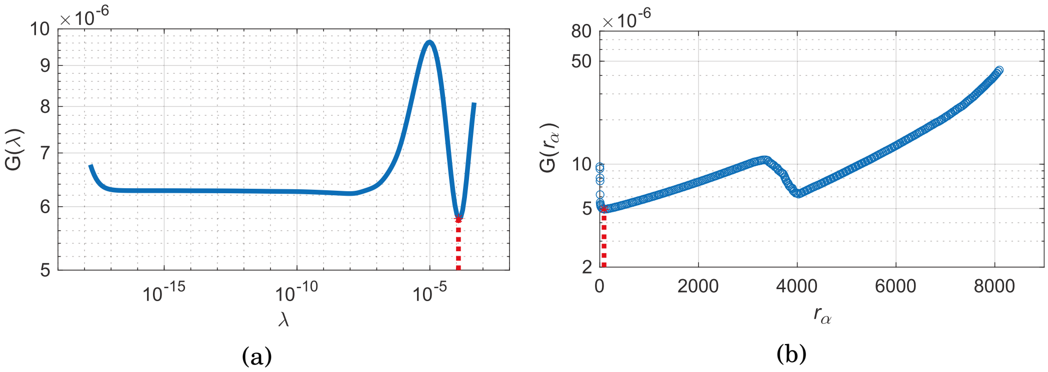

(a)

(b)

Figure 5.8: The GCV function (a) for the Tikhonov regularisation, where the minimum is found at $\lambda = 1.195 \times 10^{-4}$ and (b) for the TSVD, where the minimum is found at $r_\alpha = 87$.

5.4.5 Sound Field Reconstruction

The specific tonal frequency under investigation is 500 Hz. Fig. 5.9a shows the simulated results for some basic understanding of the sound field (Wang et al., 2015). Fig. 5.9b shows the sound pressure levels measured by the microphone array as the reference (a), whereas the reconstructed sound fields from the aforementioned three methods – (b) FBP, (c) TSVD and (d) Tikhonov – are compared.

The reconstructed sound field from the FBP method as shown in Fig. 5.9c is the least satisfactory among the three techniques. Although the general form is similar to the reference case, “lumpy” artefacts can occur with this method when the measurements are noisy and/or the amount of data is sub-optimal. In addition, the only adjustable parameter is the highpass filter, which makes it the least favourable for sound field reconstruction. The result from the TSVD is shown in Fig. 5.9d. Similar artefacts in Fig. 5.9c are still present, though they are improved compared with those from the FBP method. The best result among the three techniques is that from the Tikhonov regularisation method as shown in Fig. 5.9e. The overall reconstructed sound field is the smoothest and is the closest to the one measured by the 14 × 16 microphone array.

The sound fields reconstructed using refracto-vibrometry with the Tikhonov regularisation are quantitatively compared with the ones measured by the microphone array. The normalised difference is defined as

$$\varepsilon = \frac{||\mathbf{p}_{\mathrm{mic}} - \tilde{\mathbf{p}}_{\mathrm{Tikh}}||_2^2}{||\mathbf{p}_{\mathrm{mic}}||_2^2} \times 100\%, \tag{5.20}$$

where $\mathbf{p}_{\mathrm{mic}}$ is the pressure measured by the microphone array, $\tilde{\mathbf{p}}_{\mathrm{Tikh}}$ is the pressure measured with the Tikhonov regularisation method with $\lambda = 1.195 \times 10^{-4}$. It should be noted that $\mathbf{p}_{\mathrm{mic}} \in \mathbb{C}^{224}$ from the 14×16 array (with spacing of 60 mm), whereas the original resolution from refracto-vibrometry of $\mathbf{p}_{\mathrm{Tikh}}$ is 78×90 with spacing of 10 mm. $\tilde{\mathbf{p}}_{\mathrm{Tikh}}$ is the downscaled version to $\mathbb{C}^{224}$ for the calculation in Eq. (5.20). The downscaled sound field is demonstrated in Fig. 5.10. The normalised difference is calculated to be 10.3%, which is satisfyingly low for such a reconstruction.

5.5 Discussions

This chapter shows how to reconstruct sound fields using the refracto-vibrometry technique. The comparison made to the microphone array was to examine the quality of the reconstructed sound fields. However, it should be particularly noted that these two methods have different measurement principles. On the one hand, a microphone array can provide instantaneous and synchronous measurements of the sound field at discrete points, but the main disadvantage is the physical presence of the sensors in the sound field. On the other hand, refracto-vibrometry takes sequential measurements over multiple projections of the sound field. Although it does not impose any physical sensor limitations, the sound field is “reconstructed” from the projections rather than being directly “measured”. Therefore, the technique does not provide instantaneous measurements and the sound field should be stationary during the measurement, as arranged for the experimental campaigns herein. This open challenge limits the application of the technique, and remains to be solved in the future for refracto-vibrometry to be used in practice, where non-stationary sound fields are likely.

5.6 Summary

In this chapter, an analytical method (i.e., FBP) and two numerical methods (i.e., TSVD and Tikhonov), have been used to find the inverse Radon transform to reconstruct the sound field at the opening of an enclosure from an LDV-based refracto-vibrometry measurement campaign. Using the measurement from a 14×16 microphone array as the reference, the Tikhonov regularisation method yields the best result, whereas the FBP method gives the least satisfactory result. Next, LDV-based refracto-vibrometry will be used to control sound at an opening where obstructions are undesirable for aesthetic, ventilation and access reasons. The physical presence of a microphone array can be intrusive in such applications, whereas refracto-vibrometry might be preferable.

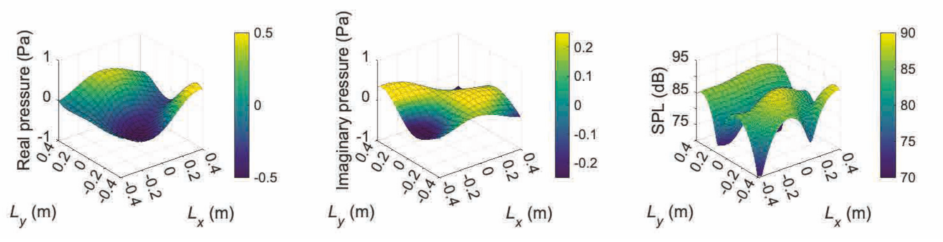

(a) Simulation

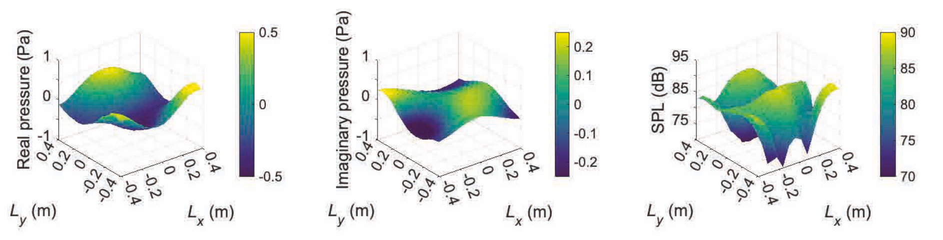

(b) Microphone array

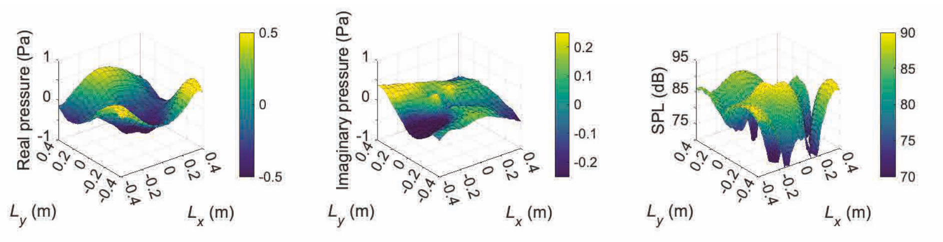

(c) FBP

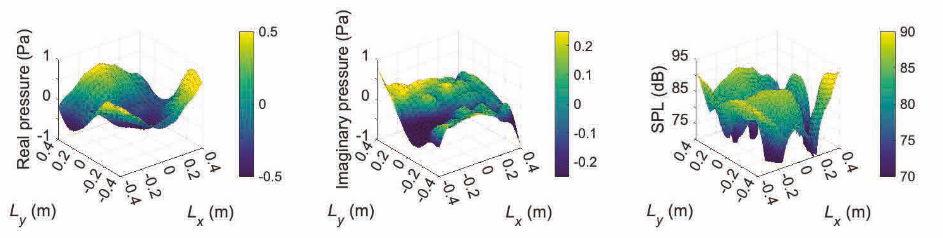

(d) TSVD

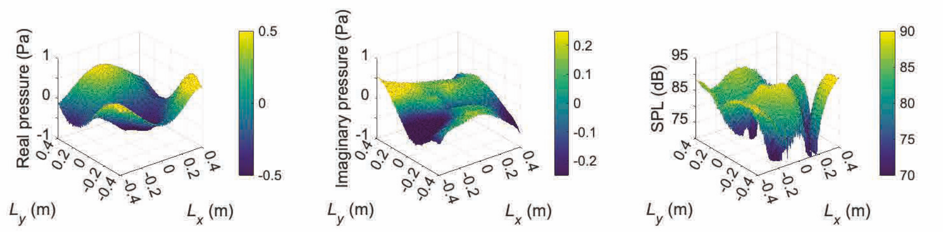

(e) Tikhonov

Figure 5.9: Real (left) and imaginary (middle) parts of the sound pressure and the SPLs (right) from (a) simulation results, (b) the 14×16 microphone array, and reconstructed from (c) the FBP, (d) the TSVD and (e) the Tikhonov regularisation methods.

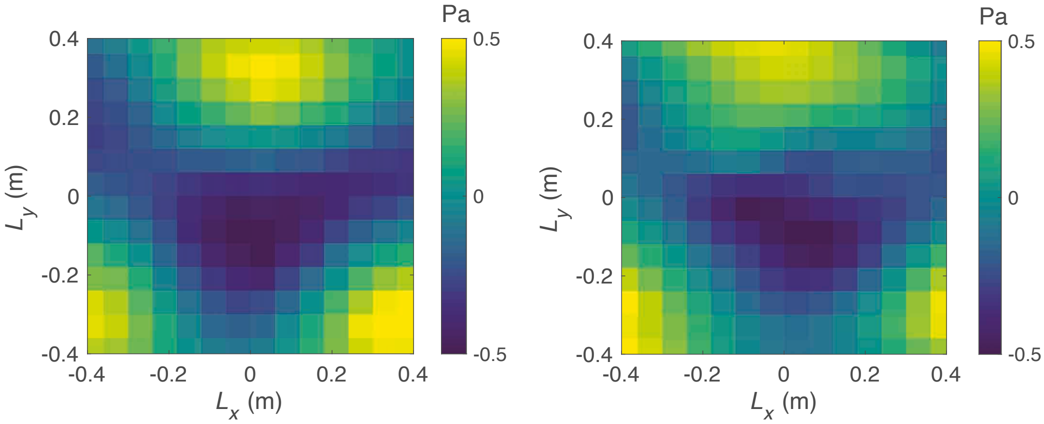

(a) Microphone array

(b) Tikhonov, downsampled

Figure 5.10: Sound pressure field measured by (a) a 14 × 16 microphone array, (b) refracto-vibrometry downscaled to the size of 14 × 16. The normalised difference is calculated to be 10.3%.

CHAPTER 6

ANC with Refracto-vibrometry

6.1 Introduction

Controlling noise propagating through a large opening is difficult. As reviewed in Chapter 1, a significant number of transducers (both secondary sources and error sensors) are required for effective performance. The higher the frequency of interest, the more channels are required. Past research focused rather on the configuration and the control performance of secondary sources. An evenly distributed layout leads to the best control performance, though at the expense of obstruction of the opening. A boundary layout, on the other hand, distributes the secondary sources and error microphones along the edges of the opening, which minimises the obstruction, yet limits the frequency range and requires a large number of transducers.

Here the particular focus is on the configuration and performance of the error signals, their ideal number and the associated ANC performance. When using conventional microphones as error sensors, the number of error microphones required is typically the same or, at most, double the number of the secondary sources (cf. Table 1.1). The number of error sensors is restricted in practice due to many factors, e.g., supported channels of the ANC controller, the computational overhead, the cost of the system, *etc*. However, as demonstrated in Chapter 5, refracto-vibrometry provides great sound field reconstruction quality with a high spatial resolution. This allows for a substan-

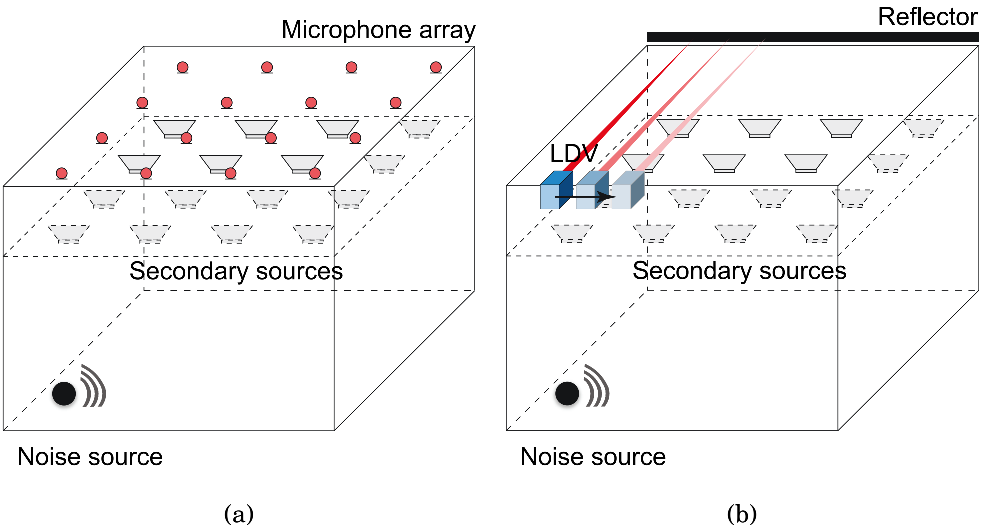

(a) (b)

Figure 6.1: Example schematic scenarios of controlling noise through an enclosure opening with an array of secondary sources while using, for the error signals, (a) a microphone array and (b) refracto-vibrometry.

tial number of error signals to be used in ANC with the potential to improve the control performance, while also not further obstructing the opening thanks to the inherent, non-invasive nature of the refracto-vibrometry technique. The schematics of both alternative systems are depicted in Fig. 6.1.

Chapter 6.2 provides the theoretical investigations on the number of error sensors on the control performance. Chapter 6.3 shows experimental results of ANC performances using either a microphone array or refracto-vibrometry. Chapter 6.4 provides some remarks on using refracto-vibrometry for ANC and Chapter 6.5 summarises the chapter.

6.2 Theoretical Investigations

Regardless of whether using a microphone array or the refracto-vibrometry technique for the error sensing, the ANC performance is bound by the physical limitations of the system. Therefore, before applying refracto-vibrometry to control noise through an opening, these limitations must be understood. In the absence of any restriction on the number of error sensors and their placement, i.e., the limit of what might be achievable with refracto-vibrometry, the question becomes:

Which and how many error sensors[*] and signals should be chosen for the best control performance?

6.2.1 System Configuration

The system to be investigated is as shown schematically in Fig. 6.2a, and is similar to that investigated in Chapter 5.4. The enclosure has dimensions of $(L_x \times L_y \times L_z) = (1 \times 0.85 \times 0.9)$ m, with the opening at the top. The primary source is placed at the location $(-0.35, -0.325, 0.1)$ m. Calculations of the sound fields of all the sources are made using the analytical model of monopoles in a cavity, which has been verified through numerical simulations (Wang et al., 2015). A total of 100 modes will be used in the subsequent section.

The evaluation point hemisphere is situated above the plane of error sensors at $z = 0.95$ m, and has a radius $r_{\text{eval}} = 5$ m. There are 201 far-field evaluation points distributed regularly on the hemisphere as shown in Fig. 6.2. Adding more points does not change the results by more than 1 dB.

For a fixed secondary source configuration, the number and positioning of the error sensors will be varied in the following analysis with the corresponding control performance observed. The benefits of an evenly distributed error sensor configuration will be validated as completed in earlier works by other researchers (Wang et al., 2019b). Some error sensor distribution options are shown in Fig. 6.3, ranging from 16 to 256 locations. For the brevity of the discussion, all the arrangements are organised in square formations, i.e., $4 \times 4, 6 \times 6, 8 \times 8$ and 16×16. The spacing between the sensors to the edge of the opening is half of the spacing between the sensors in each of the two directions in line with earlier studies (Lam et al., 2018a).

Since evenly distributed secondary sources can achieve the best noise control (Lam et al., 2018a; Wang et al., 2015, 2018), the development hereinafter also uses such a configuration. The secondary sources are thereby uniformly distributed in the xy-plane at $z = 0.72$ m. The distribution of the secondary sources is the same as that of the error sensors in each case.

---

[*] The theoretical investigations do not consider any technique or instrument for obtaining the error signals. Thus, the general term “sensor” is used here. The term “microphones” will be used when it explicitly refers to the use of conventional microphones.

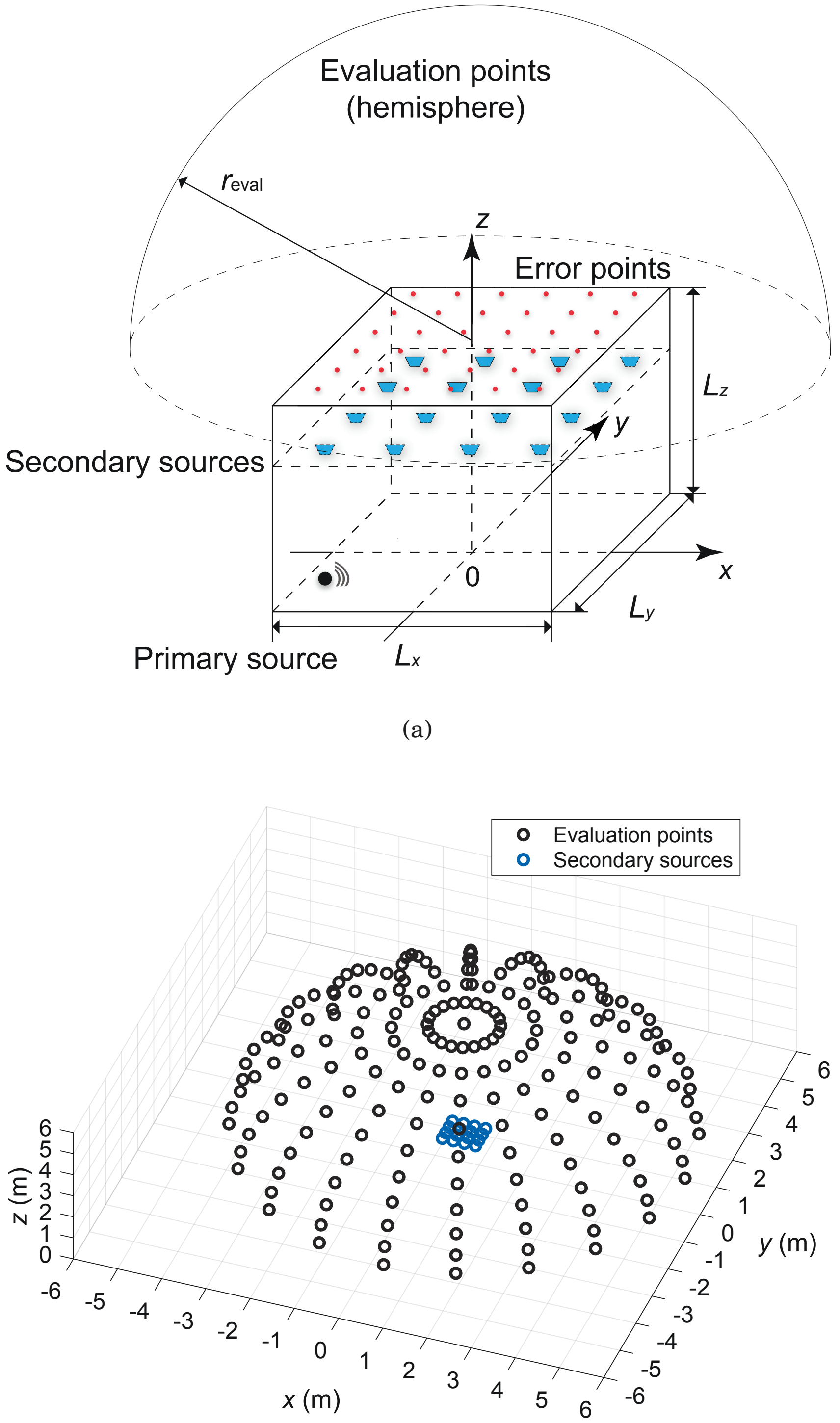

(a)

(b)

Figure 6.2: (a) The schematic diagram of the system controlling noise radiated from a cavity with 16 secondary sources evenly distributed across the opening. (b) Positions of the 201 regularly spaced evaluation points on a hemisphere of radius 5 m and above the plane of $z = 0.95$ m.

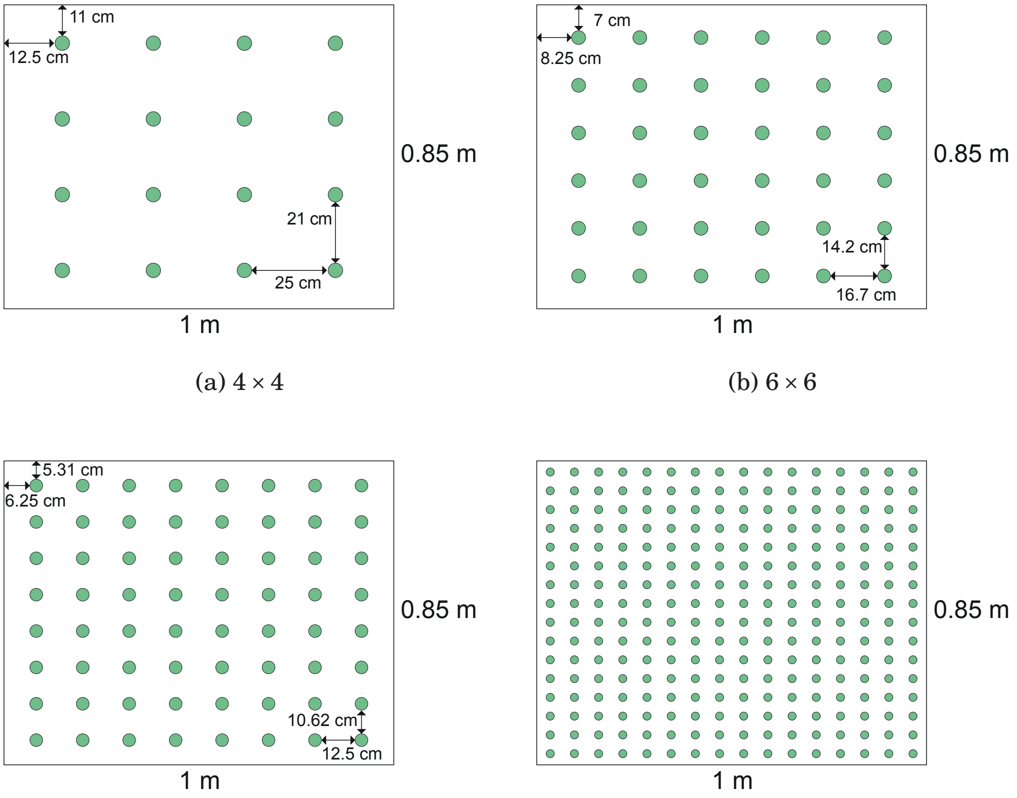

(a) 4 × 4

(b) 6 × 6

(c) 8 × 8

(d) 16 × 16

Figure 6.3: The distributions of (a) 4 × 4, (b) 6 × 6, (c) 8 × 8, and 16 × 16 error sensors in the $z = 0.95$ m xy-plane. The same distributions also apply to the secondary source locations.

6.2.2 Control Formulation and Evaluation

The primary noise source is assumed to be a monopole inside the cavity. All five walls of the cavity are considered rigid, so all sound outside the cavity is solely transmitted through the opening. The far-field hemispherical evaluation points that encompass the opening are used to estimate the radiated sound power before and after ANC is applied.

The sum of the squared sound pressures at all the error sensors is aimed to be controlled by the ANC system. Before control, the sound pressure $\mathbf{p}_\mathrm{p} \in \mathbb{C}^{N_\mathrm{e}}$ at N_e error sensors (the disturbance) due to the single primary source can be written as

$$\mathbf{p}_\mathrm{p} = \mathbf{Z}_\mathrm{pe} q_\mathrm{p}, \tag{6.1}$$

where $\mathbf{Z}_\mathrm{pe} \in \mathbb{C}^{N_\mathrm{e}}$ are the acoustic transfer functions from the primary source to the error sensor points. q_p represents the primary source strength.

After control, the error signals $\mathbf{p}_\mathrm{e} \in \mathbb{C}^{N_\mathrm{e}}$ containing sound from both primary and secondary sources, can be denoted as

$$\mathbf{p}_\mathrm{e} = \mathbf{p}_\mathrm{p} + \mathbf{p}_\mathrm{s} = \mathbf{Z}_\mathrm{pe} q_\mathrm{p} + \mathbf{Z}_\mathrm{se} \mathbf{q}_\mathrm{s}, \tag{6.2}$$

where $\mathbf{Z}_\mathrm{se} \in \mathbb{C}^{N_\mathrm{e} \times N_\mathrm{s}}$ are the acoustic transfer functions from N_s secondary sources to the error points. $\mathbf{q}_\mathrm{s} \in \mathbb{C}^{N_\mathrm{s}}$ represent the strengths of the secondary source.

The optimal secondary source strengths can be calculated by minimising the sum of the total squared sound pressures at error point locations with a control effort constraint, i.e.,

$$J = \mathbf{p}_\mathrm{e}^\mathrm{H} \mathbf{p}_\mathrm{e} + \beta \mathbf{q}_\mathrm{s}^\mathrm{H} \mathbf{q}_\mathrm{s}, \tag{6.3}$$

where superscript $^\mathrm{H}$ denotes the Hermitian transpose with β being the regularisation parameter. The optimised secondary source strengths can be found to be

$$\mathbf{q}_\mathrm{s} = -\left(\mathbf{Z}_\mathrm{se}^\mathrm{H} \mathbf{Z}_\mathrm{se} + \beta \mathbf{I}\right)^{-1} \mathbf{Z}_\mathrm{se}^\mathrm{H} \mathbf{Z}_\mathrm{pe} q_\mathrm{p}. \tag{6.4}$$

Then, the noise reduction level at N_m evaluation/monitoring points can be determined

$$\mathrm{NR\ (dB)} = 10 \log_{10} \frac{\mathbf{p}_\mathrm{pm}^\mathrm{H} \mathbf{p}_\mathrm{pm}}{\mathbf{p}_\mathrm{m}^\mathrm{H} \mathbf{p}_\mathrm{m}}, \tag{6.5}$$

where $\mathbf{p}_\mathrm{pm} = \mathbf{Z}_\mathrm{pm} q_\mathrm{p}$ is the pressure at the evaluation points without ANC. $\mathbf{p}_\mathrm{m} = \mathbf{p}_\mathrm{pm} + \mathbf{Z}_\mathrm{sm} \mathbf{q}_\mathrm{s}$ is the pressure at the evaluation points after applying the calculated optimal secondary source strengths.

6.2.3 Number of Error Signals on the Performance

The following cases are simulated using the derived analytical model:

- A fully determined system, i.e., $N_\mathrm{e} : N_\mathrm{s} = 1 : 1$
- A slightly over-determined system, e.g., $N_\mathrm{e} : N_\mathrm{s} \approx 1.5 : 1$
- A more over-determined system, e.g., $N_\mathrm{e} : N_\mathrm{s} \approx 2 : 1$
- An extremely over-determined system[*], i.e., $N_\mathrm{e} \gg N_\mathrm{s}$

The results for three different secondary sources arrangements are shown in Fig. 6.4. Controlling the noise directly at the evaluation points gives the best possible performance for given secondary sources. As observed in the results, while frequencies below 500 Hz can be effectively controlled in all three cases, adding more secondary sources increases the controllable frequency range. With 16 secondary sources, noise can be controlled up to about 800 Hz. For noise control up to about 1.5 kHz, 36 secondary sources are required. With 64 secondary sources, noise below 1.4 kHz can be controlled by more than 20 dB. Higher frequencies, such as those at 1.5 kHz – 2 kHz and 3 kHz – 4 kHz, can also be controlled by about 10 dB.

When using near-field error sensors for noise control, the number of error sensors is important, particularly at higher frequencies. So far, most of the previous works have either a fully determined system, or a slightly over-determined system. Although the lower frequency noise can be controlled, the results presented in Fig. 6.4 suggest that such systems can potentially *increase* the noise at far-field evaluation points at higher frequencies, although the secondary source strengths have been constrained within a reasonable amplitude range in Eq. 6.4. To not cause significant noise level elevations after control, the number of error sensors should ideally be at least double the number of secondary sources. For example[†], at least 36 evenly distributed error signals should be used with 16 secondary sources, at least 64 errors for 36 secondary sources, and at least 121 errors for 64 secondary sources.

This, however, can be very difficult to realise practically when using traditional microphones as error sensors. One of the major limitations of controlling

---

[*] The extremely over-determined system can still be ill-posed since the signals can be redundant, which is particularly the case for lower frequencies.

[†] Only nominally square openings with the same number of sensors in each of the two directions are considered

noise through openings is to use as few control sources and sensors as possible. Using a great number of error microphones not only obstructs the opening, particularly with an evenly distributed configuration but also increases the computational cost in a real-time controller implementation.

Some extra steps can be taken when using a limited number of error microphones. Firstly, a low-pass filter implemented in the controller hardware can suppress secondary signals in the higher frequency range. However, such filters can increase the latency of the secondary path, which is detrimental to the overall performance of ANC systems. Alternatively, the low-pass filter can be applied at the algorithm level when calculating the secondary source signals. A spectral-shaping filter can be added in the time domain, or a frequency-dependent regularisation factor can be used. However, by doing that the controlled frequency range is seriously limited. The ANC system has to give up any attempt to control even if the secondary sources have the ability to do so.

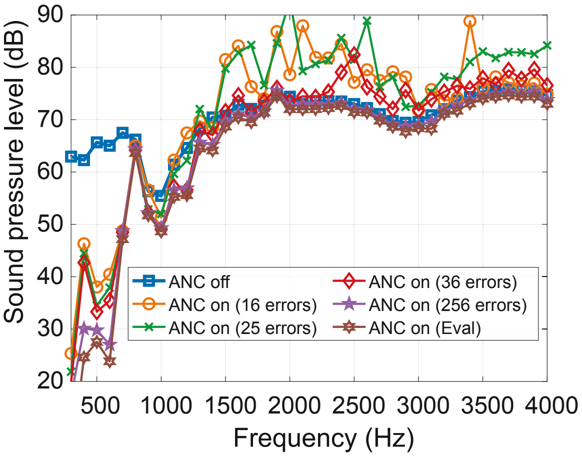

(a) 16 secondary sources

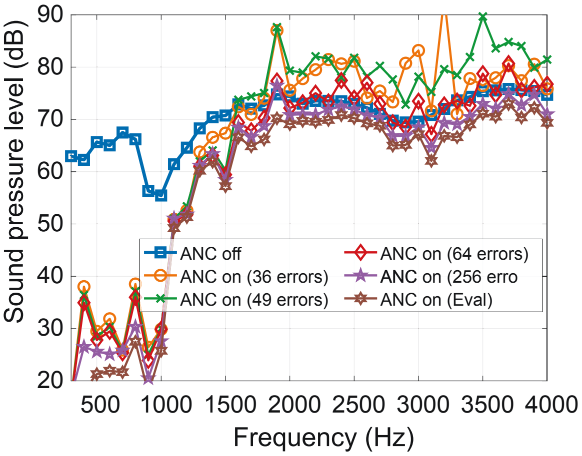

(b) 36 secondary sources

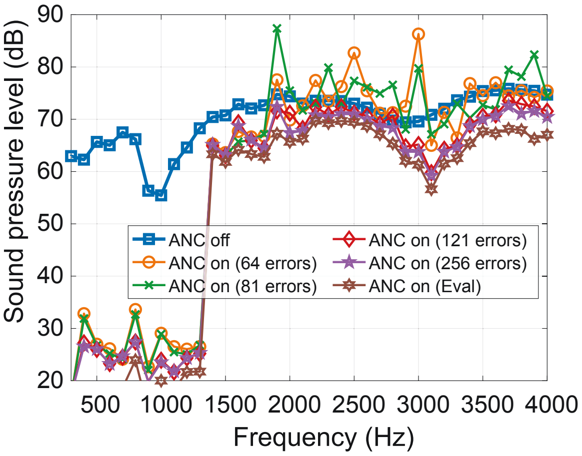

(c) 64 secondary sources

Figure 6.4: Analytical results of the overall sound pressure level determined at the 201 far-field evaluation points for different numbers of error sensors when using (a) 4 × 4, (b) 6 × 6 and (c) 8 × 8 secondary sources.

6.3 Experimental Results

6.3.1 System Setup

The experimental setup follows the investigation in the previous chapter. The sound field under investigation was at the opening of the previous enclosure with dimensions of $(L_x \times L_y \times L_z) = (1 \times 0.85 \times 0.9)$ m as shown in Fig. 6.5. The primary source (a Genelec 8010A studio monitor) was placed at the location $(-0.35, -0.325, 0.1)$ m. There were 15 secondary sources (3×5) in the xy-plane at $z = 0.72$ m. The 16 loudspeakers were connected to a 16-Channel Digital to Analog Converter (RME M-16). The configuration can be seen both schematically and as implemented experimentally in Fig. 6.5. The sound field to be measured and controlled was located at $z = 0.95$ m. A traditional sound field measurement using a 14×16 microphone (Brüel & Kjær Type 4957) array with $L_{\text{mic}} = 60$ mm spacing was taken as a reference[*]. Nine evaluation points were located on a regular grid 1 m above the enclosure opening.

Fig. 6.5 also shows the setup of using refracto-vibrometry to reconstruct the sound field. The LDV (Polytec PDV-100) was mounted on a 1.5 m motorised ball-screw slider actuated by a stepper motor (NEMA23). The reflector was a steel square hollow section beam located at a stand-off distance of $L = 1.4$ m directly behind the field with retro-reflective tape adhered to the surface for optimal optical signal level and signal-to-noise ratio. As in Chapter 5, the entire enclosure was mounted on a turntable with the LDV/slider/reflector setup remaining fixed. For each of the 36 projection angles, evenly spaced over an entire revolution, i.e., $\theta \in [0:10:350]$, there were 69 scan lines evenly spaced at an interval of 20 mm. All signals were acquired and recorded through a Brüel & Kjær DAQ modules (Type 3053 and 3160) with a sampling rate of 131.072 kHz. Environmental conditions in the anechoic chamber were 23.7 °C room temperature and relative humidity of 47.4%.

6.3.2 ANC Performance with a Microphone Array

Using the 224 microphone array, an area of 0.78 m × 0.9 m over the sound field could be measured for both the primary source and the secondary sources. Using the "Steady-State Response (SSR) Analyzer" in the Brüel & Kjær Pulse

---

[*] This array was realised using a 7×8 microphone array with 120 mm spacing sequentially positioned in four locations at 60 mm spacing

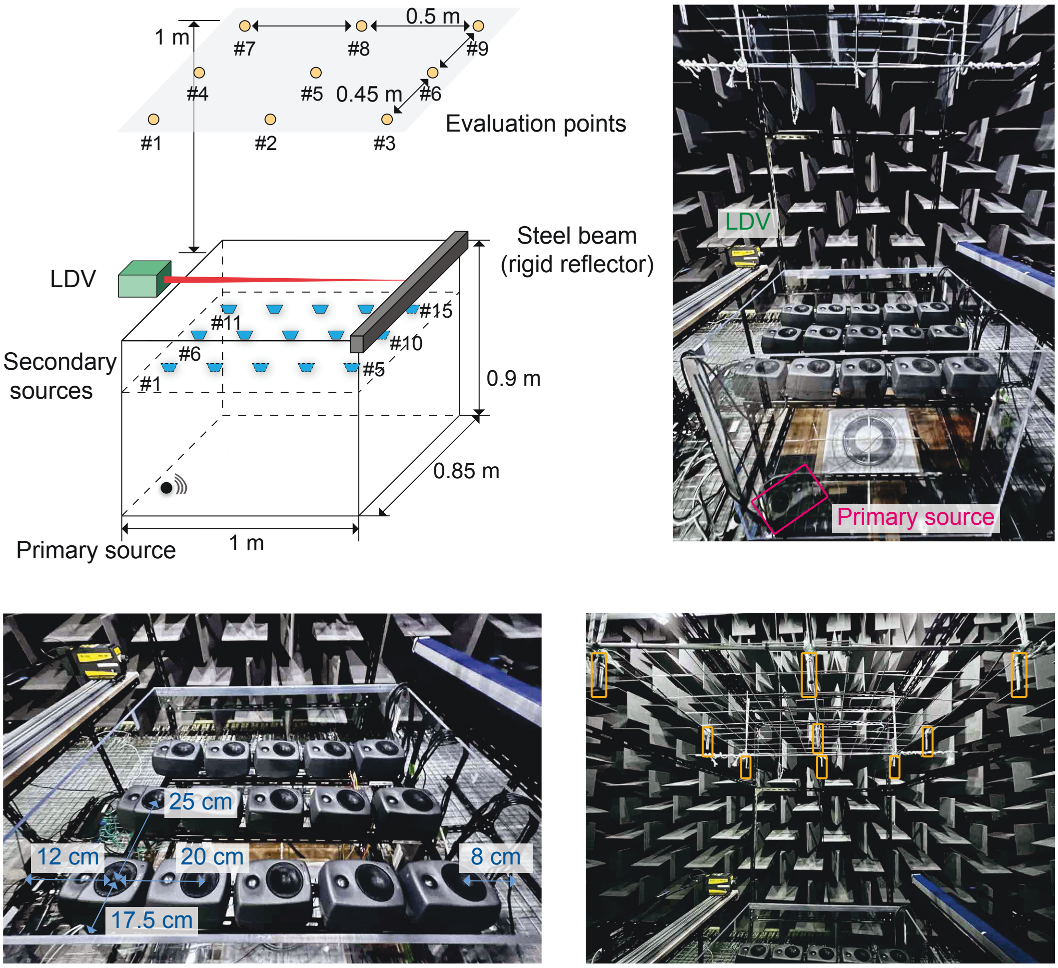

Figure 6.5: The experimental setup of using the refracto-vibrometry to measure the sound field as the error signals controlling the primary noise from the enclosure with 15 secondary sources.

LabShop software, the phase information of the sound field could also be acquired. After measuring all at 224 points for each source, some signals were chosen as the error signals for the control. The nine evaluation points were also recorded simultaneously for monitoring the system performance.

Fig. 6.6 shows the overall SPL of the nine evaluation points when using 3×5, 3×7, 6×5, 7×8 and all 14×16 error signals with the 3×5 secondary sources for frequencies from 300 Hz to 4 kHz. Results follow the theoretical findings shown in Fig. 6.4a. For low frequencies below 600 Hz, the system does not require so many error signals for an effective control performance of more than 10 dB reduction. However, if the system is fully determined ($N_\mathrm{e} : N_\mathrm{s} = 15 : 15$) or slightly over-determined ($N_\mathrm{e} : N_\mathrm{s} = 21 : 15$), the sound pressure levels at some frequencies above 1 kHz can become elevated by more than 10 dB, even though the secondary source strengths have been regularised. The trend of the results also follows those from discussions of the previous section. As the number of error signals increases, e.g., with 30 and 56 error signals, while there are still some increased pressure levels after control, these increases are not as significant, generally 5 dB maximum. If the number of error signals is sufficient, e.g., 224 errors ($N_\mathrm{e} \gg N_\mathrm{s}$), there is essentially no noise increase at higher frequencies, this being the upper control limit given only the 15 secondary sources.

From this result with the microphone array, although the number of secondary sources is limited, the previous theoretical investigations can still be verified. For low frequency noise, the system does not require as many error signals. However, if no extra steps are taken to improve the performance at higher frequencies, such as low-pass filtering as discussed previously, using a number of error signals lower than twice the number of secondary sources can inadvertently result in sound pressure level *elevation* instead[*]. Conversely, when there are many more secondary sources, e.g., 64 loudspeakers or more the noise could have also been controlled at 3 kHz – 4 kHz by about 10 dB, as shown in Fig. 6.4c. To achieve this outcome, the required number of error microphones may need to be significantly over a hundred, a set-up that is largely infeasible in practice. More likely, the system will cut out the high

---

[*] Although it is not the focus here, the spacing between the error sensors in relationship with the upper frequency limit can be found, which is similar to the studies for the secondary sources in (Lam et al., 2018a,b). This can be useful when optimising the number of required error microphones. However, as shown in Chapter 6.3.3, the relationship is not as important when using refracto-vibrometry since there are many error signals readily available for ANC.

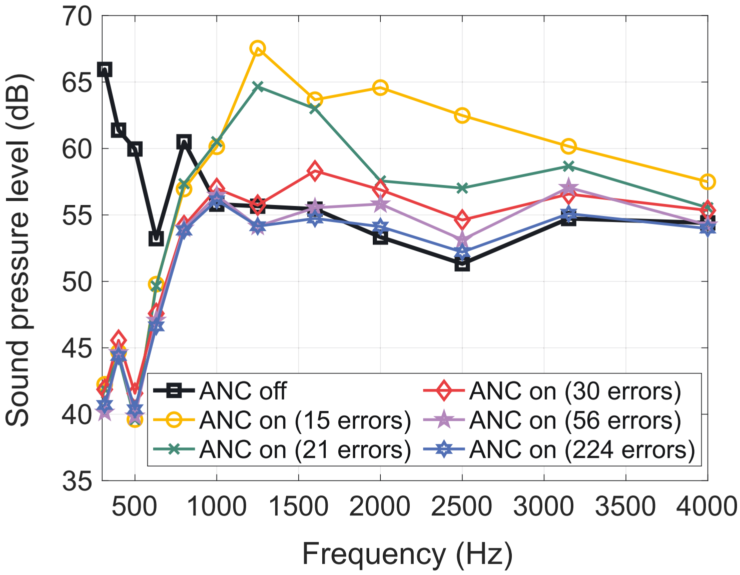

Figure 6.6: Experimental result of the overall sound pressure level of the evaluation points when using different numbers of error microphones using 3 × 5 secondary sources.

frequencies, preventing the secondary sources from being able to control these higher frequencies at all. Using refracto-vibrometry for the error sensing, however, potentially eliminates these practical limitations and therefore presents an alternative to this as will be investigated in the next subsection.

6.3.3 ANC Performance with Refracto-vibrometry

This section will demonstrate the benefits of using the refracto-vibrometry technique for error sensing by actively controlling noise in an enclosure through a large opening. As demonstrated in Fig. 6.5, there were 36 evenly spaced projection angles in a full circle, i.e., $\theta \in [0:10:350]$ with 69 scan lines evenly spaced at 20 mm increments per projection angle. Following the same data collection and noise management approach of the previous chapter, the measurements were then upsampled using the “makima” interpolation method in MATLAB with an interval of 10 mm (a total length of 1.38 m) and 72 projection angles instead. The frequency of interest was set to 2 kHz with each secondary source being activated in turn and a full refracto-vibrometry measurement campaign taken. The focus here is to see how the high frequency noise behaves using refracto-vibrometry after the control.

Using Tikhonov regularisation, the sound field can be reconstructed from the refracto-vibrometry data, as described in detail in Chapter 5. The results of the measurements and post-processing for some of the various secondary sources are illustrated in Figs. 6.7 (*Real* parts) and 6.8 (*Imaginary* parts). The subplots in the leftmost column show the sound pressure using the 14×16 microphone array (with the microphone spacing of 60 mm) to measure over the 0.78 m × 0.9 m enclosure opening area. These measurements were further scaled up (27×31, with spacing of 30 mm) using the "cubic" interpolation for better visualisation as shown in the middle column subplots. The rightmost column subplots show the corresponding results derived from refracto-vibrometry. The original refracto-vibrometry results immediately offered a spatial resolution of 96×96 with the spacing of 10 mm, but these were truncated to 78×90 with the spacing of 10 mm for ease of comparison later. The regularisation factors were 1×10^{-7} using the L-curve (Hansen, 1998). Comparing these results with the ones from the upscaled microphone array, it is very apparent that the refracto-vibrometry technique gives very close measurements to those obtained from the microphone array. However, unlike using an 837 or even *just* a 224 microphone array, the sound field can be readily measured with an extremely high spatial resolution without obstructing the opening at all.

After using refracto-vibrometry for measuring the primary source and the 15 secondary sources individually[*], the sound pressures were used to calculate the secondary source strengths to enable the control. For a fair comparison, the 7020 points of measurement (78×90) were scaled down to the same size of 14×16 as the microphone array. Fig. 6.9 shows the normalised difference between the refracto-vibrometry and microphone array measurements, determined using Eq. (5.20) from the previous chapter. Due to the symmetry of the positioning of the secondary sources, #1 – #5 and #11 – #15 are similar and thus the latter are not shown. With all the normalised differences under 20%, the reconstruction from the refracto-vibrometry technique is shown to be rather successful.

---

[*] Due to the symmetric nature of the array of secondary sources and for the sake of saving time, the measurements for secondary sources #1 – #5 were also used for #11 to #15 with no apparent loss of performance.

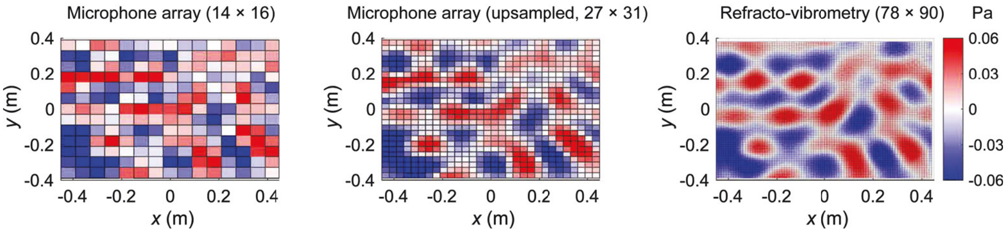

(a) Primary source

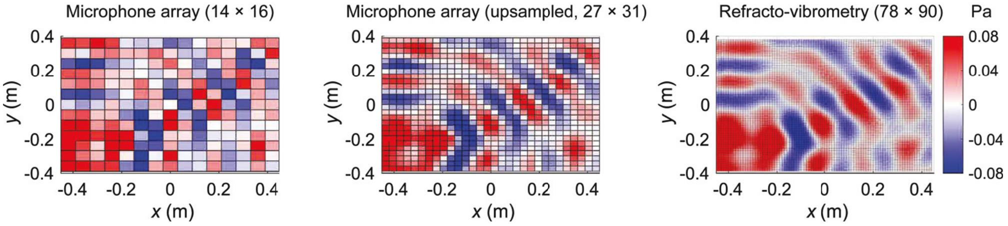

(b) Secondary #1

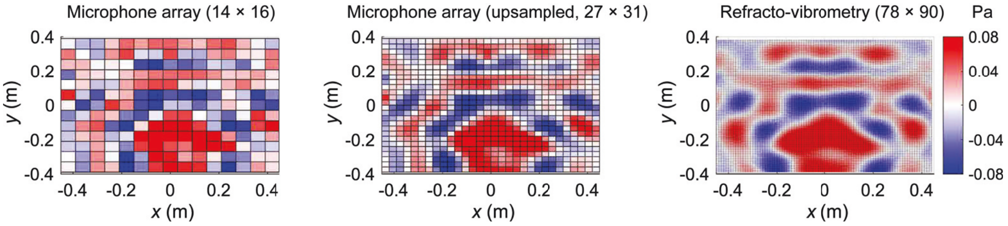

(c) Secondary #3

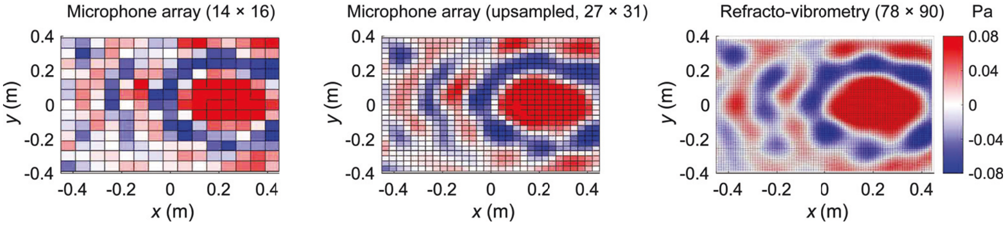

(d) Secondary #9

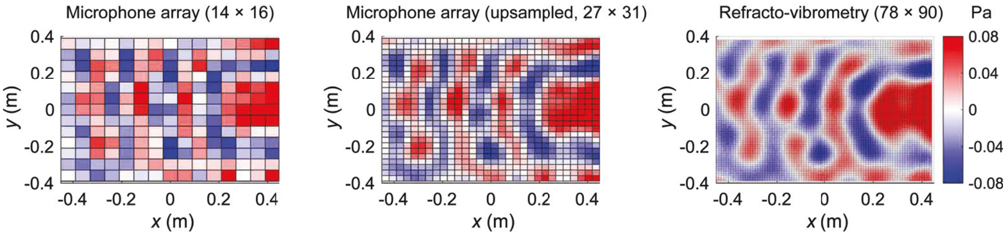

(e) Secondary #10

Figure 6.7: *Real* part of the sound pressure at 2 kHz from the 14 × 16 microphone array (left), the upscaled microphone array measurement (27 × 31) (middle), and the reconstructed using the Tikhonov regularised refracto-vibrometry technique (right) (78 × 90) for (a) the primary source, (b) the secondary source #1, (c) the secondary source #3, (d) the secondary source #9, and (e) the secondary source #10.

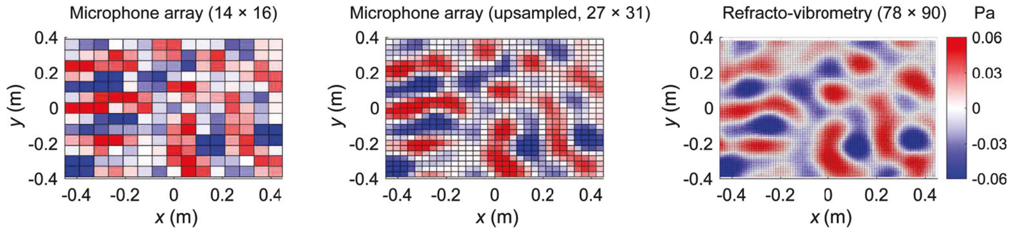

(a) Primary source

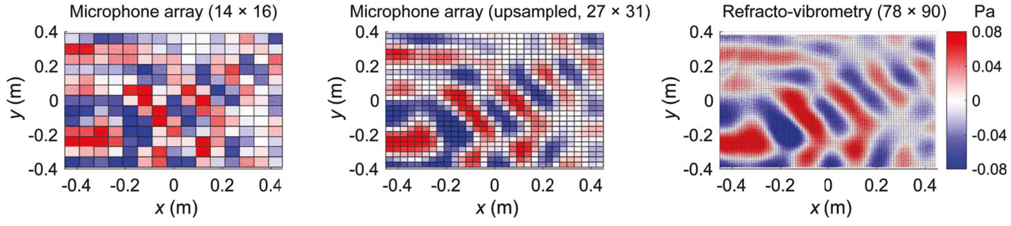

(b) Secondary #1

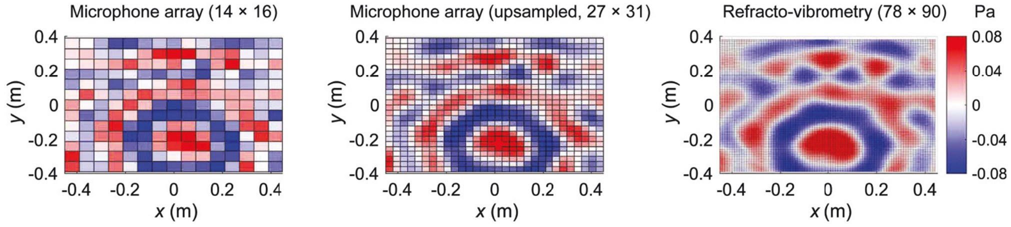

(c) Secondary #3

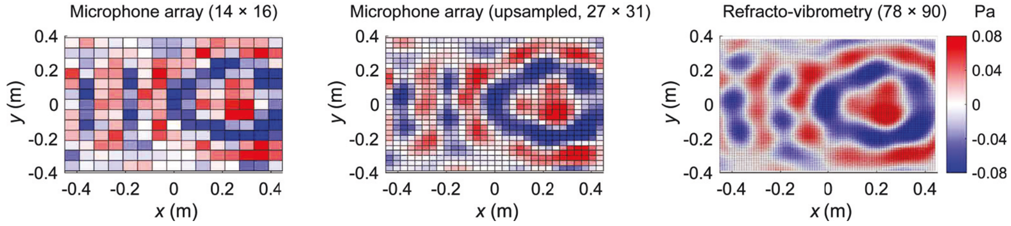

(d) Secondary #9

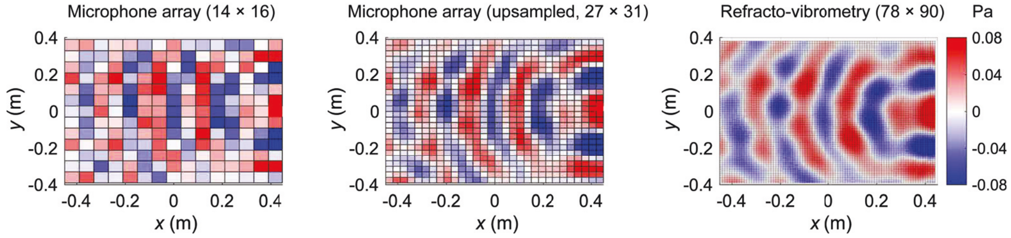

(e) Secondary #10

Figure 6.8: *Imaginary* part of the sound pressure at 2 kHz from the 14 × 16 microphone array (left), the upscaled microphone array measurement (27 × 31) (middle), and the reconstructed using the Tikhonov regularised refracto-vibrometry technique (right) (78 × 90) for (a) the primary source, (b) the secondary source #1, (c) the secondary source #3, (d) the secondary source #9, and (e) the secondary source #10.

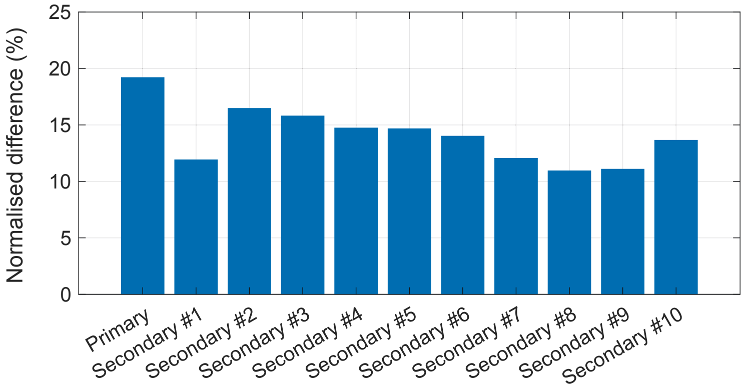

Figure 6.9: Normalised difference between the 224 microphone array and the downscaled refracto-vibrometry reconstruction results for the primary source and the secondary sources #1 – #10.

Table 6.1 shows the overall noise reduction levels at the nine evaluation points when using a different number of error signals for each of the microphone array and refracto-vibrometry techniques. Both techniques performed similarly when controlling the 2 kHz noise source. It is expected, based on previous analysis, that, when using 15 secondary sources, the fully determined case of using 15 error signals from either method will cause significant noise level elevation at higher frequencies. As the number of error signals increases, this elevation is less significant. When the system is extremely overdetermined, even without extra regularisation, the noise will not be increased, this being the performance limit for the control system given only the 15 secondary sources. Table 6.1 clearly shows all of these expected performance outcomes.

The main benefit of using the refracto-vibrometry technique for controlling the noise through an opening is that a sound field can be measured without any disturbance to it. No physical sensors are required, which is favourable for opening applications, such as windows or doorways. In addition, the measured sound field can potentially have a remarkably high spatial resolution which can then be directly exploited in ANC. Using only a fraction of the whole measurement, e.g., 224 out of 9216 possible error sensors, the ANC system realises the optimal performance that the secondary sources can achieve. This can be even more advantageous when the number of secondary sources is sufficiently large, e.g., 64 or more. In this case, thousands of error signals, e.g., all 9216 points are readily available to reach the optimal ANC solution.

Table 6.1: The overall noise reduction levels at 2 kHz at the nine evaluation points with different numbers of error signals from two measurement techniques, the microphone array and refracto-vibrometry. (Negative values mean noise level elevation.)

No. of errors	**Noise reduction level**	
	Microphone array	**Refracto-vibrometry**
15	−11.2 dB	−10.1 dB
21	−4.2 dB	−5.8 dB
30	−3.6 dB	−3.4 dB
56	−2.5 dB	−2.2 dB
224	−0.8 dB	0.2 dB
9216	–	0.1 dB

6.4 Discussions

Similar to as discussed in Chapter 5.5, using refracto-vibrometry in sound/noise control applications is not yet immediately realisable. Using a microphone array can provide real-time sound control, but the physical presence of the sensors limits its use, especially for opening applications. While refracto-vibrometry does not obstruct the opening at all, the measurements need to be made sequentially and the sound field reconstructed; thus, real-time measurements for control are not (yet) possible.

The total computational duration of the previous reconstructions can be considerable since they can only be calculated once all the projections have been made. For effective sound control applications, the duration should clearly be as short as possible. Improvements can be made through both the physical and algorithmic aspects of the system. For the former, the projections of the laser beam can be made automatic. Scanning LDVs are widely available and can scan the sound field using the fan-beam measurement configuration (Rothberg et al., 2017). For the latter, algebraic iterative reconstruction methods, such as Kaczmarz's method, Cimmino's method, and simultaneous iterative reconstruction technique (SIRT) (Hansen et al., 2021), can be used to speed up the reconstruction process, not to mention that the required computation is less expensive.

It should be noted that the proposal of refracto-vibrometry for sound control at openings was not meant to replace the microphone array. Rather, this technique can be used as an alternative or complementary error sensing method. For example, controlling low frequency noise (e.g., below 1 kHz) can still use conventional microphones as error sensors since the system does not require many error microphones. Refracto-vibrometry can be used to jointly control high frequency noise (e.g., above 1 kHz), which requires a considerable number of error sensors.

6.5 Summary

This chapter investigated the error signals in controlling noise through an enclosure opening. Theoretical investigations were made regarding the impact of the number of error signals on the ANC performance. It was discovered that the number of error signals used is crucial to high frequency noise control in particular. The system does not require a large number of error signals at low frequencies. However, for a fully determined or slightly over-determined system, the high frequency noise could be inadvertently *increased* after control. To prevent significant noise level elevation, the number of the error sensors should be at least double the number of secondary sources, i.e., $N_\mathrm{e} : N_\mathrm{s} \geq 2:1$. This can be impractical if physical microphones are used since too many microphones can obstruct the opening, not to mention that the setup is complicated and the computation expensive. Therefore, the secondary source signals must be low-pass filtered to remove the risk of elevating the sound pressure at higher frequencies while removing any attempt to control in this range, even if the secondary sources have the potential to control at those higher frequencies.

The chapter also examined the refracto-vibrometry technique in measuring the sound field of the opening as near-field error signals in the context of using these for ANC. Using this technique at a large enclosure opening, the sound fields due to a primary source and each of the 15 secondary sources can be accurately reconstructed with a very high spatial resolution compared to the corresponding results from a large channel count microphone array. Although only evaluated for a single 2 kHz tonal component, the results from the refracto-vibrometry technique were the same as those for the microphone array. However, unlike the microphone array, which can significantly obstruct the opening, the refracto-vibrometry technique leaves the opening completely unobstructed, while still providing a large number of error signals for the ANC system. If the number of secondary sources is sufficiently large and able to control the high frequency noise, the ANC system will give the best performance that the secondary sources allow since the refracto-vibrometry technique provides the required considerable number of error signals.

CHAPTER

7

Conclusions and Future Works

This chapter states the general conclusions drawn from this thesis. The detailed contributions can be found at the end of each chapter and are not repeated here. Following this, possible future research directions are suggested.

7.1 Conclusions

This thesis was motivated by the multitude of issues stemming from the physical presence of conventional microphones in contemporary ANC applications, particularly ANC headrests and ANC windows. For ANC headrests, the error microphones cannot be installed close to the user's ears. The reference microphones also cannot be too close to the main system (the headrest). For ANC windows, the distributed layout of the error microphones can better sense the sound field at the opening for control. However, the opening should ideally continue to be free from any such obstructions to allow for effective ventilation, sufficient lighting or for merely aesthetic reasons. Due to these problems, a non-intrusive error sensing method was identified as a need for further development. Laser Doppler vibrometry can offer non-contact and non-invasive vibro-acoustic measurements, with the potential to resolve the identified open challenges in both ANC headrests and windows.

The overall structure and main contributions are demonstrated in Fig. 7.1.

The first part of the thesis (Chapters 2, 3 and 4) was concerned with using LDVs for ANC headrests. Firstly, a remote acoustic sensing apparatus has been developed that consists of a retro-reflective membrane and an LDV at a remote location. The small lightweight membrane without any cables could be placed at the location of interest, whereby the LDV could then measure the acoustically-induced membrane surface vibration at that remote location. Next, the apparatus was applied to an ANC headrest for error sensing. The membrane was placed in the cavum concha of the synthetic ears of a head and torso simulator. The results showed that more than 10 dB sound attenuation could be obtained over an ultra-broadband frequency range up to 6 kHz for multiple sound sources and various types of common environmental noise. Finally, the locations of the reference sensors have also been studied. It has been found that a typical non-minimum-phase secondary path requires a significant amount of time advance, that is, preserving enough latency for the controller to have an effective performance, especially for low frequencies. The LDV-based remote acoustic sensing arrangement has also been investigated for reference signals. For a traditional, physically connected reference microphone placed far away from the main system, the remote reference sensing method achieves comparable performance but without the requirement for any physical connection.

The second part of the thesis (Chapter 5 and 6) was concerned with using LDVs for ANC windows or a large opening in general. Instead of measuring a large sound field at discrete points, a line-based sound field measurement technique, i.e., refracto-vibrometry, has been investigated. This approach could serve as an alternative method to measure sound pressure at all the points of interest without disturbing the sound field as is the case for microphones. Experimental results showed that the Tikhonov regularisation method yielded the best result when compared to the alternative filtered back-projection and truncated singular value decomposition options relative to a microphone array. Then, this technique was applied to measuring sound fields at the enclosure opening from a primary source and 15 secondary sources for the purpose of ANC. Through a series of theoretical investigations, which are later verified through experiments, it was discovered that, for an evenly distributed layout, the ratio of the number of error signals to secondary sources should be at least $2:1$ so as not to cause elevated noise levels at the high frequencies, e.g., above 2 kHz. Although this could be impractical using conventional microphones, since the number can be so great as to obstruct the opening, this is not the case when using the refracto-vibrometry technique. The experimental results have demonstrated that refracto-vibrometry can be used to determine the sound pressure at all the points of interest without disturbing the sound field and with high spatial resolution. If the number of secondary sources was sufficient and could potentially control the high frequency noise, the ANC performance would not be limited by the number of error signals and could reach the optimal solution that the secondary sources allow. If the secondary sources could only control the low frequency noise, using refracto-vibrometry would at least not cause noise level increase at the high frequencies as can occur for a microphone-based approach.

Overall, the laser Doppler vibrometry based remote sensing method has been proven to be very effective in solving the issues of the physical presence of conventional microphones in a number of ANC applications.

7.2 Future Works

Outlined below are a number of potential future research directions arising from work presented in this thesis.

- **Remote error sensing with remote sensing**
  Although Fig. 3.7 in Chapter 3 showed that placing the retro-reflective membrane in the cavum concha of an ear can achieve the best ANC performance, with the worst observed at the small lobe (lobule) of the ear, a more practically realistic approach is still to put the membrane on the lobule for both comfort and aesthetic reasons. To maintain the best control performance, some of the remote sensing methods as reviewed in Chapter 1.3.2 can be combined with the proposed remote error sensing arrangement with an LDV. For example, by using the remote microphone method, that is, pre-determing the transfer function between the signals at the lobule and at the cavum concha, even though the physical membrane is adhered to the lobule, the ANC performance can still, theoretically, be as if based on a *virtual* membrane placed at the cavum concha for the best performance.

- **Non-stationary paths with the LDV based remote sensing**

LDV-based remote acoustic sensing has been applied to both the error and the reference signals for ANC headrests. The primary and secondary paths measured by the LDVs can be more perturbed compared to the ones from the conventional microphones. To make the system more robust, some measures can be taken on the algorithm level to prevent performance degradation due to sudden changes in the error and reference measurements (Elliott et al., 2020).

- **Refracto-vibrometry with adaptive reconstruction**
  Similar to using the FxLMS algorithm to make the ANC system adaptive, the refracto-vibrometry technique for measuring a large sound field can also be adaptive. The noise through an opening can be non-stationary and the use of an adaptive algorithm can be more practical. Kaczmarz's method, Cimmino's method and simultaneous iterative reconstruction technique (SIRT) (Hansen et al., 2021) can be explored and associated with an adaptive ANC algorithm in the future.

- **Refracto-vibrometry with presumed acoustical models**
  Chapter 1.4.2 described some previous works that incorporated acoustical models during the reconstruction to make the results more accurate. Yatabe et al. (2017) added the Kirchhoff-Helmholtz integral equation and the Herglotz wave function for interpolation when the measurements were limited or noisy. Acoustic holography has also been explored. Plane-wave expansion model was also used. The reconstructed sound field can be extrapolated and thus only a partial area needs to be measured (Fernandez-Grande et al., 2013; Verburg & Fernandez-Grande, 2021). These methods and possibly others can be explored in the future for better and quicker reconstruction for sound/noise control applications.

- **Controlling both sound pressure and intensity with refracto-vibrometry**
  It has been demonstrated that the refracto-vibrometry technique can provide a very high spatial resolution sound pressure measurement for the error signals for controlling noise at an opening. With enough information, the sound intensity can also be estimated to determine the acoustic energy flow. Then, instead of controlling only the sound pressure,

the ANC system can potentially control both the sound pressure and the intensity, which can achieve an even better ANC performance.

- **Using refracto-vibrometry to measure broadband sound**
  The thesis experimentally investigated using the refracto-vibrometry technique at certain tonal frequencies. Combining measurements of different tonal frequencies may not necessarily be directly translated to measuring and controlling a broadband sound. Adjustments or corrections might be required for an accurate result when applying such a system to measure different kinds of broadband environmental sound for application in ANC windows.

- **Refracto-vibrometry affected by flow**
  Air fluctuation due to other than acoustic waves, such as wind, can indeed affect the optical measurements. One can study the optical signals when the system is sensing the acoustic waves and/or wind. It is expected that the measurements from the two situations can have distinctive characteristics. Once these situations are understood, the system can recognise when the wind is present. Then the system can either reduce the signal interference from the wind or discard the measurement. This remains to be an open challenge to be explored in the future.

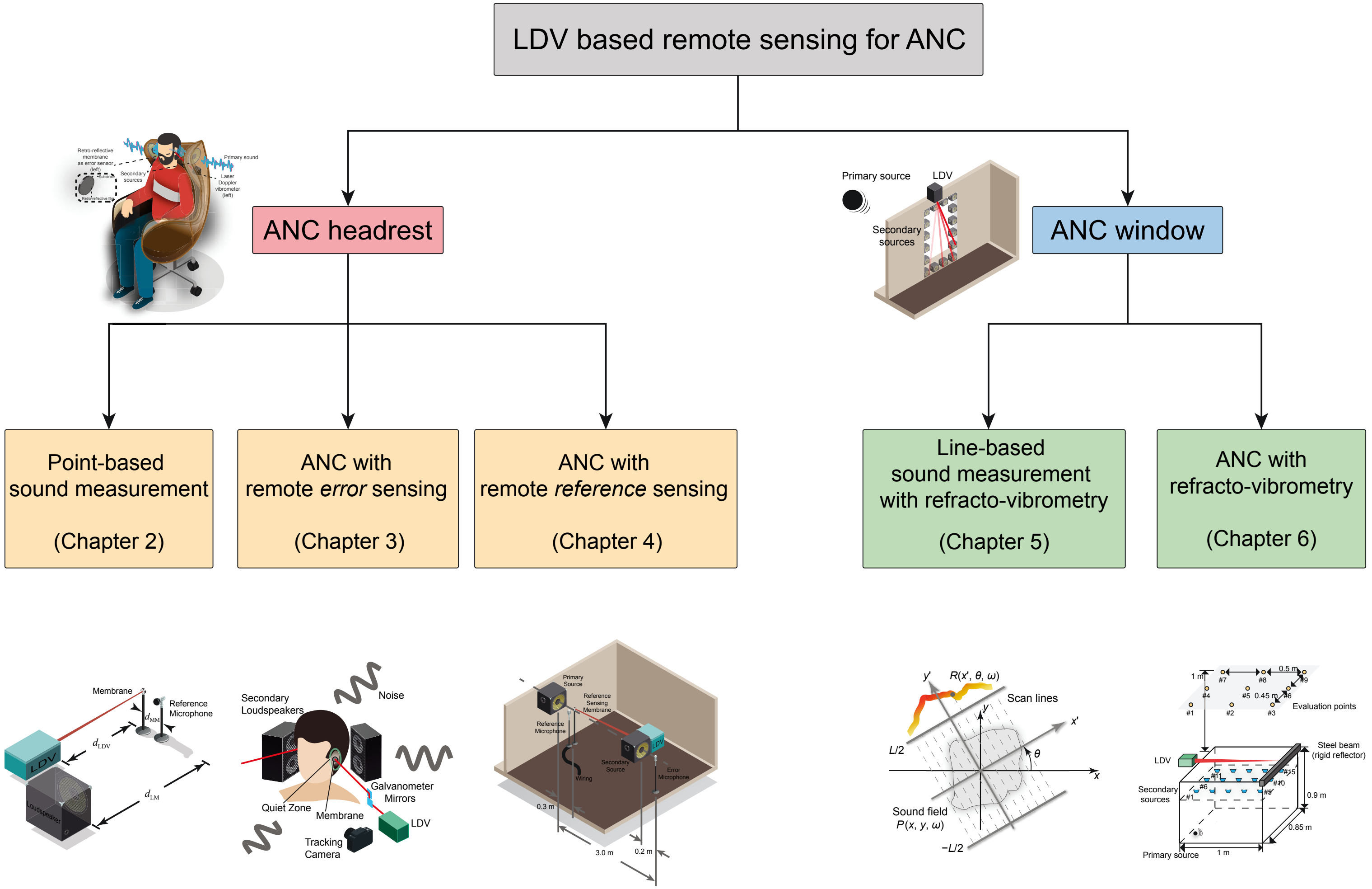

Figure 7.1: Conclusion of major contribution areas.

Bibliography

Airplane Sound Effects (2019). Airplane sound effects. [Online; accessed 2019-09-01].

Akhtar, M. T. & Mitsuhashi, W. (2011). Improving performance of hybrid active noise control systems for uncorrelated narrowband disturbances. *IEEE Transactions on Audio, Speech and Language Processing*, 19(7), 2058–2066.

Ang, L. Y. L., Koh, Y. K., & Lee, H. P. (2017). The performance of active noise-canceling headphones in different noise environments. *Applied Acoustics*, 122, 16–22.

Bai, M. & Lee, D. (1997). Implementation of an active headset by using the h,àû robust control theory. *The Journal of the Acoustical Society of America*, 102(4), 2184–2190.

Bai, M. R., Pan, W., & Chen, H. (2018). Active feedforward noise control and signal tracking of headsets: Electroacoustic analysis and system implementation. *The Journal of the Acoustical Society of America*, 143(3), 1613–1622.

Barrett, H. H. (1984). Iii the radon transform and its applications. *Progress in optics*, 21, 217–286.

BBC Sound Effects (2019). Bbc sound effects - research & education space. [Online; accessed 2019-09-01].

Berengier, M. & Roure, A. (1980). Broad-band active sound absorption in a duct carrying uniformly flowing fluid. *Journal of Sound and Vibration*, 68(3), 437–449.

Bertero, M. & Boccacci, P. (2020). *Introduction to inverse problems in imaging*. CRC press.

Bies, D. A., Hansen, C. H., & Howard, C. Q. (2017). *Engineering noise control*. CRC press.

Bilaniuk, N. (1997). Optical microphone transduction techniques. *Applied acoustics*, 50(1), 35–63.

Bissinger, G. & Oliver, D. (2007). 3-d laser vibrometry on legendary old italian violins. *Sound and Vibration*, 41(7), 10–15.

Brammer, A. J., Pan, G. J., & Crabtree, R. B. (1997). Adaptive feedforward active noise reduction headset for low-frequency noise. In *INTER-NOISE and NOISE-CON Congress and Conference Proceedings*, volume 1997 (pp. 399–406).: Institute of Noise Control Engineering.

Brggemann, H., Hanselka, J., & Sachau, D. (2019). Experimental study on the effects of increasing number of system components and sampling rate of an active noise blocker for a tilted window. In *INTER-NOISE and NOISE-CON Congress and Conference Proceedings*, volume 259 (pp. 3829–3838).: Institute of Noise Control Engineering.

Brillouin, L. (1922). Diffusion de la lumière et des rayons x par un corps transparent homogène. In *Annales de physique*, volume 9 (pp. 88–122).

Brüel & Kjær (2019). Microphone handbook.

Buck, J., Jukkert, S., & Sachau, D. (2018). Performance evaluation of an active headrest considering non-stationary broadband disturbances and head movement. *The Journal of the Acoustical Society of America*, 143(5), 2571–2579.

Bullmore, A., Nelson, P., Curtis, A., & Elliott, S. (1987). The active minimization of harmonic enclosed sound fields, part ii: A computer simulation. *Journal of Sound and Vibration*, 117(1), 15–33.

Burgess, G., Shortis, M., & Scott, P. (2011a). Photographic assessment of retroreflective film properties. *ISPRS journal of photogrammetry and remote sensing*, 66(5), 743–750.

Burgess, G., Shortis, M. R., & Scott, P. (2011b). Photographic assessment of retroreflective film properties. *ISPRS Journal of Photogrammetry and Remote Sensing*, 66(5), 743–750.

Burgess, J. C. (1981). Active adaptive sound control in a duct: A computer simulation. *The Journal of the Acoustical Society of America*, 70(3), 715–726.

Carme, C. (1987). *Absorption acoustique active dans les cavités*. PhD thesis, Aix-Marseille 2.

Carme, C. (1988). A new filtering method by feedback for anc at the ear. *Proc. Inter-Noise 88*, (pp. 1083–1086).

Carme, C., Schevin, O., Romerowski, C., & Clavard, J. (2016). Active opening windows. *Proceedings of the ICSV*.

Cartes, D. A., Ray, L. R., & Collier, R. D. (2002). Experimental evaluation of leaky least-mean-square algorithms for active noise reduction in communication headsets. *The Journal of the Acoustical Society of America*, 111(4), 1758–1771.

Cazzolato, B. S. (1999). Sensing systems for active control of sound transmission into cavities. *Mechanical Engineering*.

Chang, C.-Y., Siswanto, A., Ho, C.-Y., Yeh, T.-K., Chen, Y.-R., & Kuo, S. M. (2016). Listening in a noisy environment: Integration of active noise control in audio products. *IEEE Consumer Electronics Magazine*, 5(4), 34–43.

Chaplin, B. (1980). The cancellation of repetitive noise and vibration. In *INTER-NOISE and NOISE-CON Congress and Conference Proceedings*, volume 1980 (pp. 699–702).: Institute of Noise Control Engineering.

Chaplin, G. (1983). Waveform synthesis-the essex solution to repetitive noise and vibration. *Proc, of Internoise'83*.

Chaplin, G. B., Smith, R. A., & Bramer, T. P. (1987). Method and apparatus for reducing repetitive noise entering the ear. US Patent 4,654,871.

Cheer, J. & Elliott, S. J. (2015). Multichannel control systems for the attenuation of interior road noise in vehicles. *Mechanical Systems and Signal Processing*, 60, 753–769.

Cheer, J., Patel, V., & Fontana, S. (2019). The application of a multi-reference control strategy to noise cancelling headphones. *The Journal of the Acoustical Society of America*, 145(5), 3095–3103.

Chen, W., Rao, W., Min, H., & Qiu, X. (2011). An active noise barrier with unidirectional secondary sources. *Applied Acoustics*, 72(12), 969–974.

Chitanont, N., Yaginuma, K., Yatabe, K., & Oikawa, Y. (2015). Visualization of sound field by means of schlieren method with spatio-temporal filtering. In *2015 IEEE International Conference on Acoustics, Speech and Signal Processing (ICASSP)* (pp. 509–513).: IEEE.

Chitanont, N., Yatabe, K., Ishikawa, K., & Oikawa, Y. (2017). Spatio-temporal filter bank for visualizing audible sound field by schlieren method. *Applied Acoustics*, 115, 109–120.

Crocker, M. J. (2007). *Handbook of noise and vibration control*. John Wiley.

Curtis, A., Nelson, P., & Elliott, S. (1985). Active control of one-dimensional enclosed sound fields. In *INTER-NOISE and NOISE-CON Congress and Conference Proceedings*, volume 1985 (pp. 579–582).: Institute of Noise Control Engineering.

David, A. & Elliott, S. (1994). Numerical studies of actively generated quiet zones. *Applied Acoustics*, 41, 63–79.

Debye, P. & Sears, F. (1932). On the scattering of light by supersonic waves. *Proceedings of the National Academy of Sciences of the United States of America*, 18(6), 409.

Eargle, J. (2012). *The Microphone Book: From mono to stereo to surround-a guide to microphone design and application*. CRC Press.

Edamoto, S., Shi, C., & Kajikawa, Y. (2016). Virtual sensing technique for feedforward active noise control. In *Proceedings of Meetings on Acoustics 172ASA*, volume 29 (pp. 030001).: Acoustical Society of America.

Eder, J., Hanselka, J., & Sachau, D. (2017). Experimental comparison on the effect of the number of system components of an active noise blocker. In *INTER-NOISE and NOISE-CON Congress and Conference Proceedings*, volume 255 (pp. 3525–3534).: Institute of Noise Control Engineering.

Eghtesadi, K. (1983). The tight-coupled monopole active attenuator in a duct. *Noise Contr. Eng. J.*, 20, 16–20.

Elliott, S., Joseph, P., Bullmore, A., & Nelson, P. (1988a). Active cancellation at a point in a pure tone diffuse sound field. *Journal of Sound and Vibration*, 120(1), 183–189.

Elliott, S., Stothers, I., Nelson, P., McDonald, A., Quinn, D., & Saunders, T. (1988b). The active control of engine noise inside cars. In *INTER-NOISE and NOISE-CON congress and conference proceedings*, volume 1988 (pp. 987–990).: Institute of Noise Control Engineering.

Elliott, S. J. (2000). *Signal processing for active control*. Academic Press.

Elliott, S. J. & David, A. (1992). A virtual microphone arrangement for local active sound control. INTERNATIONAL CONFERENCE ON MOTION AND VIBRATION CONTROL (pp. 1027–1031). Tokyo: The Society.

Elliott, S. J. & Jones, M. (2006). An active headrest for personal audio. *The Journal of the Acoustical Society of America*, 119(5), 2702–2709.

Elliott, S. J., Joseph, P., Bullmore, A., & Nelson, P. A. (1988c). Active cancellation at a point in a pure tone diffuse sound field. *Journal of sound and vibration*, 120(1), 183–189.

Elliott, S. J., Jung, W., & Cheer, J. (2018). Head tracking extends local active control of broadband sound to higher frequencies. *Scientific reports*, 8(1), 1–7.

Elliott, S. J., Zhang, J., Kwan Lai, C., & Cheer, J. (2020). Superposition of the uncertainties in acoustic responses and the robust design of active control systems. *The Journal of the Acoustical Society of America*, 148(3), 1415–1424.

Emms, G. & Fox, C. (2001). Control of sound transmission through an aperture using active sound absorption techniques: a theoretical investigation. *Applied Acoustics*, 62(6), 735–747.

Eriksson, L., Allie, M., & Greiner, R. (1987). The selection and application of an iir adaptive filter for use in active sound attenuation. *IEEE Transactions on acoustics, speech, and signal processing*, 35(4), 433–437.

Fernandez-Grande, E., Torras-Rosell, A., & Jacobsen, F. (2013). Holographic reconstruction of sound fields based on the acousto-optic effect. In *INTER-NOISE and NOISE-CON Congress and Conference Proceedings*, volume 247 (pp. 3181–3190).: Institute of Noise Control Engineering.

Fernandez-Grande, E., VERBURG, S., & HAHMANN, M. (2019). Acousto-optic capture of the sound field in a room based on sparse measurement data.

Field, C. & Fricke, F. (1998). Theory and applications of quarter-wave resonators: A prelude to their use for attenuating noise entering buildings through ventilation openings. *Applied Acoustics*, 53(1-3), 117–132.

Fletcher, H. & Munson, W. A. (1933). Loudness, its definition, measurement and calculation. *Bell System Technical Journal*, 12(4), 377–430.

Ford, R. & Kerry, G. (1973). The sound insulation of partially open double glazing. *Applied Acoustics*, 6(1), 57–72.

Forno, C. (1988). Deformation measurement using high resolution moiré photography. *Optics and lasers in engineering*, 8(3-4), 189–212.

Gan, W. S. & Kuo, S. M. (2002). An integrated audio and active noise control headset. *IEEE Transactions on Consumer Electronics*, 48(2), 242–247.

Gan, W. S., Mitra, S., & Kuo, S. M. (2005). Adaptive feedback active noise control headset: Implementation, evaluation and its extensions. *IEEE Transactions on Consumer Electronics*, 51(3), 975–982.

Gan, W.-S., Yang, J., & Kamakura, T. (2012). A review of parametric acoustic array in air. *Applied Acoustics*, 73(12), 1211–1219. Parametric Acoustic Array: Theory, Advancement and Applications.

Garcia-Bonito, J. & Elliott, S. (1995). Local active control of diffracted diffuse sound fields. *The Journal of the Acoustical Society of America*, 98(2), 1017–1024.

Garcia-Bonito, J., Elliott, S. J., & Boucher, C. C. (1997). Generation of zones of quiet using a virtual microphone arrangement. *The Journal of the Acoustical Society of America*, 101(6), 3498–3516.

Garthe, D. (1991). A fiber-optic microphone. *Sensors and Actuators A: Physical*, 26(1-3), 341–345.

Goodwin, G. (1984). Adaptive filtering prediction and control. *Englewood Cliffs*.

Gordon, E. I. (1966). A review of acoustooptical deflection and modulation devices. *Applied optics*, 5(10), 1629–1639.

Grande, E. F., Riezu, S. A. V., & Hahmann, M. (2019). Acousto-optic capture of the sound field in a room based on sparse measurement data. In *International Symposium on Room Acoustics 2019* (pp. 451–457).: Nederlands Akoestisch Genootschap.

Guicking, D. & Karcher, K. (1984). Active impedance control for one-dimensional sound. *Journal of vibration, acoustics, stress, and reliability in design*, 106(3), 393–396.

Guo, J. & Pan, J. (1998). Effects of reflective ground on the actively created quiet zones. *The Journal of the Acoustical Society of America*, 103(2), 944–952.

Guo, J., Pan, J., & Bao, C. (1997). Actively created quiet zones by multiple control sources in free space. *The Journal of the Acoustical Society of America*, 101(3), 1492–1501.

Halkon, B. J. & Rothberg, S. J. (2021). Establishing correction solutions for scanning laser doppler vibrometer measurements affected by sensor head vibration. *Mechanical Systems and Signal Processing*, 150, 107255.

Hanselka, J. & Sachau, D. (2016). Experimental study on the influence of the sensor and actuator arrangement on the performance of an active noise blocker for a tilted window. In *INTER-NOISE and NOISE-CON Congress and Conference Proceedings*, volume 253 (pp. 5298–5309).: Institute of Noise Control Engineering.

Hansen, C., Snyder, S., Qiu, X., Brooks, L., & Moreau, D. (2012). *Active control of noise and vibration*. CRC press.

Hansen, P. C. (1990). Truncated singular value decomposition solutions to discrete ill-posed problems with ill-determined numerical rank. *SIAM Journal on Scientific and Statistical Computing*, 11(3), 503–518.

Hansen, P. C. (1994). Regularization tools: a matlab package for analysis and solution of discrete ill-posed problems. *Numerical algorithms*, 6(1), 1–35.

Hansen, P. C. (1998). *Rank-deficient and discrete ill-posed problems: numerical aspects of linear inversion*. SIAM.

Hansen, P. C., Jørgensen, J., & Lionheart, W. R. (2021). *Computed Tomography: Algorithms, Insight, and Just Enough Theory*. SIAM.

Hawley, M. E. (1956). Acoustic interference for noise control. *Noise Control*, 2(2), 61–94.

Hesselmann, N. (1978). Investigation of noise reduction on a 100 kva transformer tank by means of active methods. *Applied acoustics*, 11(1), 27–34.

Heuchel, F. M., Caviedes-Nozal, D., Brunskog, J., Agerkvist, F. T., & Fernandez-Grande, E. (2020). Large-scale outdoor sound field control. *The Journal of the Acoustical Society of America*, 148(4), 2392–2402.

Hu, A., Cuomo, F. W., & Zuckerwar, A. J. (1992). Theoretical and experimental study of a fiber optic microphone. *The Journal of the Acoustical Society of America*, 91(5), 3049–3056.

Hu, Q. & Tang, S. K. (2019). Active cancellation of sound generated by finite length coherent line sources using piston-like secondary source arrays. *The Journal of the Acoustical Society of America*, 145(6), 3647–3655.

Huang, H., Qiu, X., & Kang, J. (2011). Active noise attenuation in ventilation windows. *The Journal of the Acoustical Society of America*, 130(1), 176–188.

Ikeda, Y., Okamoto, N., Konishi, T., Oikawa, Y., Tokita, Y., & Yamasaki, Y. (2016). Observation of traveling wave with laser tomography. *Acoustical Science and Technology*, 37(5), 231–238.

Ise, S. (2005). The boundary surface control principle and its applications. *IEICE transactions on fundamentals of electronics, communications and computer sciences*, 88(7), 1656–1664.

Ishikawa, K., Yatabe, K., Chitanont, N., Ikeda, Y., Oikawa, Y., Onuma, T., Niwa, H., & Yoshii, M. (2016). High-speed imaging of sound using parallel phase-shifting interferometry. *Optics express*, 24(12), 12922–12932.

Ishikawa, K., Yatabe, K., Ikeda, Y., Oikawa, Y., Onuma, T., Niwa, H., & Yoshii, M. (2017). Interferometric imaging of acoustical phenomena using high-speed polarization camera and 4-step parallel phase-shifting technique. In *Selected Papers from the 31st International Congress on High-Speed Imaging and Photonics*, volume 10328 (pp. 93–99).: SPIE.

Jackett, R., Piper, B., & Hughes, R. J. (2017). Characterization of acoustic diffusion using refracto-vibrometry. *Journal of Sound and Vibration*, 392, 70–76.

Jakob, A. & Möser, M. (2003a). Active control of double-glazed windows. part ii: Feedback control. *Applied Acoustics*, 64(2), 183–196.

Jakob, A. & Möser, M. (2003b). Active control of double-glazed windowspart i: Feedforward control. *Applied Acoustics*, 64(2), 163–182.

Jones, O. & Smith, R. (1983). The selective anti-noise ear defender. In *INTER-NOISE and NOISE-CON Congress and Conference Proceedings*, volume 1983 (pp. 375–378).: Institute of Noise Control Engineering.

Joseph, P., Elliott, S., & Nelson, P. (1994). Near field zones of quiet. *Journal of Sound and Vibration*, 172(5), 605–627.

Jung, W., Elliott, S. J., & Cheer, J. (2017). Combining the remote microphone technique with head-tracking for local active sound control. *The Journal of the Acoustical Society of America*, 142(1), 298–307.

Jung, W., Elliott, S. J., & Cheer, J. (2018). Estimation of the pressure at a listener's ears in an active headrest system using the remote microphone technique. *The Journal of the Acoustical Society of America*, 143(5), 2858–2869.

Jung, W., Elliott, S. J., & Cheer, J. (2019). Local active control of road noise inside a vehicle. *Mechanical Systems and Signal Processing*, 121, 144–157.

Kajikawa, Y. & Shi, C. (2019). Comparison of virtual sensing techniques for broadband feedforward active noise control. In *2019 International Conference on Control, Automation and Information Sciences (ICCAIS)* (pp. 1–5).: IEEE.

Kak, A. C. & Slaney, M. (2001). *Principles of computerized tomographic imaging*. SIAM.

Kang, J.-H. (2017). Viscously damped free and forced vibrations of circular and annular membranes by a closed form exact method. *Thin-Walled Structures*, 116, 194–200.

Kinsler, L. E., Frey, A. R., Coppens, A. B., & Sanders, J. V. (1999). *Fundamentals of acoustics*. John wiley & sons.

Ko, S. C., Kim, Y. C., Lee, S. S., Choi, S. H., & Kim, S. R. (2003). Micromachined piezoelectric membrane acoustic device. *Sensors and Actuators A: Physical*, 103(1-2), 130–134.

Kuo, S., Mitra, S., & Gan, W.-S. (2006). Active noise control system for headphone applications. *IEEE Transactions on Control Systems Technology*, 14(2), 331–335.

Kuo, S. M. & Morgan, D. R. (1996). *Active noise control systems : algorithms and DSP implementations*. Wiley.

Kwon, B. & Park, Y. (2013). Interior noise control with an active window system. *Applied Acoustics*, 74(5), 647–652.

Lam, B., Elliott, S., Cheer, J., & Gan, W.-S. (2018a). Physical limits on the performance of active noise control through open windows. *Applied Acoustics*, 137, 9–17.

Lam, B., Gan, W.-S., Shi, D., Nishimura, M., & Elliott, S. (2021). Ten questions concerning active noise control in the built environment. *Building and Environment*, 200, 107928.

Lam, B., Shi, C., Shi, D., & Gan, W.-S. (2018b). Active control of sound through full-sized open windows. *Building and Environment*, 141, 16–27.

Lam, B., Shi, D., Gan, W.-S., Elliott, S. J., & Nishimura, M. (2020). Active control of broadband sound through the open aperture of a full-sized domestic window. *Scientific reports*, 10(1), 1–7.

Lavergne, T., Durand, S., Bruneau, M., Joly, N., & Rodrigues, D. (2010). Dynamic behavior of the circular membrane of an electrostatic microphone: Effect of holes in the backing electrode. *The Journal of the Acoustical Society of America*, 128(6), 3459–3477.

Leissa, A. (1989). Closed form exact solutions for the steady state vibrations of continuous systems subjected to distributed exciting forces. *Journal of Sound and Vibration*, 134(3), 435–453.

Li, Y., Segers, P., Dirckx, J., & Baets, R. (2013). On-chip laser doppler vibrometer for arterial pulse wave velocity measurement. *Biomedical Optics Express*, 4(7), 1229.

Liebich, S., Richter, J.-G., Fabry, J., Durand, C., Fels, J., & Jax, P. (2018). Direction-of-Arrival Dependency of Active Noise Cancellation Headphones. volume ASME 2018 Noise Control and Acoustics Division Session presented at INTERNOISE 2018 of *Noise Control and Acoustics Division Conference*. V001T08A003.

Lokberg, O. J., Rustad, R., & Espeland, M. (1994). Reconstruction of sound fields using tv holography. In *First International Conference on Vibration Measurements by Laser Techniques: Advances and Applications*, volume 2358 (pp. 305–312).: International Society for Optics and Photonics.

Lucas, R. & Biquard, P. (1932). Optical properties of solids and liquids under ultrasonic vibrations. *J. Phys. Rad.*, 3, 464.

Lueg, P. (1936). Process of silencing sound oscillations. US Patent 2,043,416.

Malkin, R., Todd, T., & Robert, D. (2014). A simple method for quantitative imaging of 2d acoustic fields using refracto-vibrometry. *Journal of Sound and Vibration*, 333(19), 4473–4482.

Meeker, W. F. (1957). Component characteristics for an active ear defender. *The Journal of the Acoustical Society of America*, 29(11), 1252–1252.

Moreau, D., Cazzolato, B., Zander, A., & Petersen, C. (2008). A review of virtual sensing algorithms for active noise control. *Algorithms*, 1(2), 69–99.

Morse, P. M. & Ingard, K. U. (1986). *Theoretical acoustics*. Princeton university press.

Muller, G., Black, R., & Davis, T. (1938). The diffraction produced by cylindrical and cubical obstacles and by circular and square plates. *The Journal of the Acoustical Society of America*, 10(1), 6–13.

Murao, T. & Nishimura, M. (2012). Basic study on active acoustic shielding. *Journal of Environment and Engineering*, 7(1), 76–91.

Nelson, P., Curtis, A., Elliott, S., & Bullmore, A. (1987a). The active minimization of harmonic enclosed sound fields, part i: Theory. *Journal of Sound and Vibration*, 117(1), 1–13.

Nelson, P., Curtis, A., Elliott, S., & Bullmore, A. (1987b). The minimum power output of free field point sources and the active control of sound. *Journal of sound and vibration*, 116(3), 397–414.

Nelson, P. A. & Elliott, S. (1991). *Active control of sound*. Academic Press.

Ohnishi, K., Saito, T., Teranishi, S., Namikawa, Y., Mori, T., Kimura, K., & Uesaka, K. (2004). Development of the product-type active soft edge noise barrier. In *Proceedings of the 18th international congress on acoustics, Kyoto, Japan* (pp. 4–9).

Oikawa, Y., Goto, M., Ikeda, Y., Takizawa, T., & Yamasaki, Y. (2005). Sound field measurements based on reconstruction from laser projections. In *Proceedings.(ICASSP'05). IEEE International Conference on Acoustics, Speech, and Signal Processing, 2005.*, volume 4 (pp. iv–661).: IEEE.

Olson, H. F. (1956). Electronic control of noise, vibration, and reverberation. *The Journal of the Acoustical Society of America*, 28(5), 966–972.

Olson, H. F. & May, E. G. (1953). Electronic sound absorber. *The Journal of the Acoustical Society of America*, 25(6), 1130–1136.

Oswald, L. J. (1984). Reproduction of diesel engine noise inside passenger compartments using active adaptive noise control. *Proceedings of Inter-Noise'84*, (pp. 483–488).

Pàmies, T., Romeu, J., Genescà, M., & Arcos, R. (2014). Active control of aircraft fly-over sound transmission through an open window. *Applied acoustics*, 84, 116–121.

Pan, G., Brammer, A., & Crabtree, R. (1997). Adaptive active noise reduction headset for helicopter aircrew. *Audio Effectiveness in Aviation*, (596), 9.

Pawelczyk, M. (2004). Adaptive noise control algorithms for active headrest system. *Control Engineering Practice*, 12(9), 1101–1112.

Pawelczyk, M. (2008). Analog active control of acoustic noise at a virtual location. *IEEE Transactions on Control Systems Technology*, 17(2), 465–472.

Piraux, J. & Mazzanti, S. (1985). Broadband active noise attenuation in three-dimensional space. In *INTER-NOISE and NOISE-CON Congress and Conference Proceedings*, volume 1985 (pp. 485–488).: Institute of Noise Control Engineering.

Piraux, J. & Nayroles, B. (1980). A theoretical model for active noise attenuation in three-dimensional space. In *INTER-NOISE and NOISE-CON Congress and Conference Proceedings*, volume 1980 (pp. 703–706).: Institute of Noise Control Engineering.

Polytec GmbH (2019). *MSA-050 Micro System Analyzer Datasheet*. Technical report.

Qiu, X. (2019). *An Introduction to Virtual Sound Barriers*. CRC Press.

Quate, C. F., Wilkinson, C., & Winslow, D. (1965). Interaction of light and microwave sound. *Proceedings of the IEEE*, 53(10), 1604–1623.

Rafaely, B. & Elliott, S. (1999). H_2/H_∞ active control of sound in a headrest: design and implementation. *IEEE Transactions on Control Systems Technology*, 7(1), 79–84.

Rafaely, B., Elliott, S. J., & Garcia-Bonito, J. (1999). Broadband performance of an active headrest. *The Journal of the Acoustical Society of America*, 106(2), 787–793.

Rafaely, B. & Jones, M. (2002). Combined feedback-feedforward active noise-reducing headset-the effect of the acoustics on broadband performance. *The Journal of the Acoustical Society of America*, 112(3), 981–989.

Rosell, A. T., Grande, E. F., Jacobsen, F., & Figueroa, S. B. (2012). Investigating the use of the acousto-optic effect for acoustic holography. In *41st International Congress and Exposition on Noise Control Engineering*.

Ross, C. (1978). Experiments on the active control of transformer noise. *Journal of Sound and Vibration*, 61(4), 473–480.

Rothberg, S., Allen, M., Castellini, P., Di Maio, D., Dirckx, J., Ewins, D., Halkon, B. J., Muyshondt, P., Paone, N., Ryan, T., et al. (2017). An international review of laser doppler vibrometry: Making light work of vibration measurement. *Optics and Lasers in Engineering*, 99, 11–22.

Roure, A. (1985). Self-adaptive broadband active sound control system. *Journal of Sound and Vibration*, 101(3), 429–441.

Roure, A. & Albarrazin, A. (1999). The remote microphone technique for active noise control. volume 1999 (pp. 1233–1244).

Rudzyn, B. & Fisher, M. (2012). Performance of personal active noise reduction devices. *Applied Acoustics*, 73(11), 1159–1167.

Shi, D., Lam, B., & Gan, W.-s. (2019). Analysis of multichannel virtual sensing active noise control to overcome spatial correlation and causality constraints. In *ICASSP 2019-2019 IEEE International Conference on Acoustics, Speech and Signal Processing (ICASSP)* (pp. 8499–8503).: IEEE.

Simshauser, E. D. & Hawley, M. E. (1955). The noise-cancelling headset-an active ear defender. *The Journal of the Acoustical Society of America*, 27(1), 207–207.

Siswanto, A., Chang, C.-Y., & Kuo, S. M. (2015). Active noise control for headrests. In *2015 Asia-Pacific Signal and Information Processing Association Annual Summit and Conference (APSIPA)* (pp. 688–692).: IEEE.

Snyder, S. D. & Hansen, C. H. (1989). Active noise control in ducts: Some physical insights. *The Journal of the Acoustical Society of America*, 86(1), 184–194.

Stansfeld, S., Berglund, B., Clark, C., Lopez-Barrio, I., Fischer, P., öhrström, E., Haines, M., Head, J., Hygge, S., van Kamp, I., & Berry, B. (2005). Aircraft and road traffic noise and children's cognition and health: a cross-national study. *The Lancet*, 365(9475), 1942–1949.

Stansfeld, S. A. & Matheson, M. P. (2003). Noise pollution: Non-auditory effects on health. *British Medical Bulletin*, 68, 243–257.

Suh, J.-G., Cho, W.-H., Kim, H.-Y., Cui, Z., & Suzuki, Y. (2019). Sensitivity measurement of a laboratory standard microphone by measuring the diaphragm vibration. *Applied Acoustics*, 143, 38–47.

Sujbert, L. & Szarvas, A. (2018). Noise-canceling office chair with multiple reference microphones. *Applied Sciences*, 8(9), 1702.

Sutton, T. J. (1994). Active control of road noise inside vehicles. *Noise Contr. Eng. J.*, 42(4), 137–147.

Swinbanks, M. (1984). The active control of noise and vibration and some applications in industry. *Proceedings of the Institution of Mechanical Engineers, Part A: Power and Process Engineering*, 198(4), 281–288.

Tabatabai, H., Oliver, D. E., Rohrbaugh, J. W., & Papadopoulos, C. (2013). Novel applications of laser doppler vibration measurements to medical imaging. *Sensing and Imaging: An International Journal*, 14(1), 13–28.

Tanaka, K., Shi, C., & Kajikawa, Y. (2017). Binaural active noise control using parametric array loudspeakers. *Applied Acoustics*, 116, 170–176.

Tanaka, N. & Tanaka, M. (2010). Active noise control using a steerable parametric array loudspeaker. *The Journal of the Acoustical Society of America*, 127(6), 3526–3537.

Tang, S. K., Tong, Y., & Tsui, K. (2016). Sound transmission acrosss a plenum window with an active noise cancellation system. *Noise Control Engineering Journal*, 64(4), 423–431.

Tao, J., Wang, S., Qiu, X., & Pan, J. (2016). Performance of an independent planar virtual sound barrier at the opening of a rectangular enclosure. *Applied Acoustics*, 105, 215–223.

Tichy, J. & Warnaka, G. E. (1983). Effect of evanescent waves on the active attenuation of sound in ducts. In *Proc. of Inter-Noise* (pp. 435–438).

Tikhonov, A. N. & Arsenin, V. Y. (1977). Solutions of ill-posed problems. *New York*, 1, 30.

Tong, Y., Tang, S. K., Kang, J., Fung, A., & Yeung, M. (2015). Full scale field study of sound transmission across plenum windows. *Applied Acoustics*, 89, 244–253.

Torras-Rosell, A., Barrera-Figueroa, S., & Jacobsen, F. (2012). Sound field reconstruction using acousto-optic tomography. *The Journal of the Acoustical Society of America*, 131(5), 3786–3793.

Torras-Rosell, A., Lylloff, O., Barrera-Figueroa, S., & Jacobsen, F. (2013). Reconstruction methods for sound visualization based on acousto-optic tomography. In *Proc Internoise*.

Transportation Ambience (2019). Transportation ambience. [Online; accessed 2019-09-01].

Trinder, M. & Jones, O. (1987). Active noise control at the ear. In *Proceedings of Noise-Con '87* (pp. 393–398).: Institute of Noise Control Engineering.

Twiney, R. C. & Salloway, A. J. (1990). Noise reduction system. US Patent 4,953,217.

Veit, I. (1988). A lightweight headset with an active noise compensation. In *INTER-NOISE and NOISE-CON Congress and Conference Proceedings*, volume 1988 (pp. 1087–1090).: Institute of Noise Control Engineering.

Verburg, S. A. & Fernandez-Grande, E. (2019). *Acousto-optic sensing-spatial reconstruction of the sound field enclosed in a room*. Universitätsbibliothek der RWTH Aachen.

Verburg, S. A. & Fernandez-Grande, E. (2021). Acousto-optical volumetric sensing of acoustic fields. *Physical Review Applied*, 16(4), 044033.

Verburg, S. A., Fernandez-Grande, E., & Barrera-Figueroa, S. (2019). Acousto-optic sensing of the sound field in a lightly damped room. In *INTER-NOISE and NOISE-CON Congress and Conference Proceedings*, volume 259 (pp. 7240–7248).: Institute of Noise Control Engineering.

Wang, K., Tao, J., & Qiu, X. (2019a). Boundary control of sound transmission into a cavity through its opening. *Journal of Sound and Vibration*, 442, 350–365.

Wang, S., Tao, J., & Qiu, X. (2015). Performance of a planar virtual sound barrier at the baffled opening of a rectangular cavity. *The Journal of the Acoustical Society of America*, 138(5), 2836–2847.

Wang, S., Tao, J., & Qiu, X. (2017a). Controlling sound radiation through an opening with secondary loudspeakers along its boundaries. *Scientific reports*, 7(1), 1–6.

Wang, S., Tao, J., Qiu, X., & Pan, J. (2018). Mechanisms of active control of sound radiation from an opening with boundary installed secondary sources. *The Journal of the Acoustical Society of America*, 143(6), 3345–3351.

Wang, S., Tao, J., Qiu, X., & Pan, J. (2019b). A boundary error sensing arrangement for virtual sound barriers to reduce noise radiation through openings. *The Journal of the Acoustical Society of America*, 145(6), 3695–3702.

Wang, S., Yu, J., Qiu, X., Pawelczyk, M., Shaid, A., & Wang, L. (2017b). Active sound radiation control with secondary sources at the edge of the opening. *Applied Acoustics*, 117, 173–179.

Warnaka, G. E., Poole, L. A., & Tichy, J. (1984). Active acoustic attenuator. US Patent 4,473,906.

Warnaka, G. E., Tichy, J., & Poole, L. A. (1981). Improvements in adaptive active attenuators. In *INTER-NOISE and NOISE-CON Congress and Conference Proceedings*, volume 1981 (pp. 307–310).: Institute of Noise Control Engineering.

Wheeler, P. D. (1986). *Voice communications in the cockpit noise environment: The role of active noise reduction*. PhD thesis.

Widrow, B. & Stearns, S. (1985). Adaptive signal processing. *Englewood Cliffs*.

Wissmeyer, G., Pleitez, M. A., Rosenthal, A., & Ntziachristos, V. (2018). Looking at sound: optoacoustics with all-optical ultrasound detection. *Light: Science & Applications*, 7(1), 1–16.

Wu, L., Qiu, X., Burnett, I. S., & Guo, Y. (2015). Decoupling feedforward and feedback structures in hybrid active noise control systems for uncorrelated narrowband disturbances. *Journal of Sound and Vibration*, 350, 1–10.

Xiao, T. & Qiu, X. (2019). A comparison of using sound pressure and particle velocity as error signals for local active noise control. In *Proceedings of the 26th International Congress on Sound and Vibration, ICSV 2019*.

Xiao, T., Qiu, X., & Halkon, B. (2020). Ultra-broadband local active noise control with remote acoustic sensing. *Scientific reports*, 10(1), 1–12.

Xiao, T., Qiu, X., & Halkon, B. (2021a). Using a laser doppler vibrometer to estimate sound pressure in air. In S. Oberst, B. Halkon, J. Ji, & T. Brown (Eds.), *Vibration Engineering for a Sustainable Future* (pp. 371–377). Cham: Springer International Publishing.

Xiao, T., Zhao, S., Qiu, X., & Halkon, B. (2021b). Using a retro-reflective membrane and laser doppler vibrometer for real-time remote acoustic sensing and control. *Sensors*, 21(11).

Yatabe, K., Ishikawa, K., & Oikawa, Y. (2017). Acousto-optic back-projection: Physical-model-based sound field reconstruction from optical projections. *Journal of Sound and Vibration*, 394, 171–184.

Yatabe, K. & Oikawa, Y. (2014). Pde-based interpolation method for optically visualized sound field. In *2014 IEEE International Conference on Acoustics, Speech and Signal Processing (ICASSP)* (pp. 4738–4742).: IEEE.

Yatabe, K. & Oikawa, Y. (2015). Optically visualized sound field reconstruction based on sparse selection of point sound sources. In *2015 IEEE International Conference on Acoustics, Speech and Signal Processing (ICASSP)* (pp. 504–508).: IEEE.

Yoneyama, M., Fujimoto, J.-i., Kawamo, Y., & Sasabe, S. (1983). The audio spotlight: An application of nonlinear interaction of sound waves to a new type of loudspeaker design. *The Journal of the Acoustical Society of America*, 73(5), 1532–1536.

Zevitas, C. D., Spengler, J. D., Jones, B., McNeely, E., Coull, B., Cao, X., Loo, S. M., Hard, A. K., & Allen, J. G. (2018). Assessment of noise in the airplane cabin environment. *Journal of Exposure Science and Environmental Epidemiology*, 28(6), 568–578.

Zhang, L. & Qiu, X. (2014). Causality study on a feedforward active noise control headset with different noise coming directions in free field. *Applied Acoustics*, 80, 36–44.

Zhang, L., Wu, L., & Qiu, X. (2013). An intuitive approach for feedback active noise controller design. *Applied Acoustics*, 74(1), 160–168.

Zhong, J., Xiao, T., Halkon, B., Kirby, R., & Qiu, X. (2020). An experimental study on the active noise control using a parametric array loudspeaker. In *INTER-NOISE and NOISE-CON Congress and Conference Proceedings*, volume 261 (pp. 662–668).: Institute of Noise Control Engineering.

Zhou, X. & Merzenich, M. M. (2012). Environmental noise exposure degrades normal listening processes. *Nature Communications*, 3(1), 843.

Zipser, L. & Franke, H. H. (2008). Refracto-vibrometry-a novel method for visualizing sound waves in transparent media. *Journal of the Acoustical Society of America*, 123(5), 3314.

Zoran, A., Welch, S., & Hunt, W. D. (2012). A platform for manipulation and examination of the acoustic guitar: The chameleon guitar. *Applied Acoustics*, 73(4), 338–347.

Zuckerwar, A. J. (1978). Theoretical response of condenser microphones. *The Journal of the Acoustical Society of America*, 64(5), 1278–1285.